Technische Universität München
TUM School of Engineering and Design

Determination of Equivalence Ratio Fluctuations in a Lean Premixed Dual Fuel Gas Turbine Combustor

Manuel Johann Vogel

Vollständiger Abdruck der von der TUM School of Engineering and Design der Technischen Universität München zur Erlangung eines

DOKTORS DER INGENIEURWISSENSCHAFTEN (DR.-ING.)

genehmigten Dissertation.

Vorsitz:
apl. Prof. Dr.-Ing. Christian W. M. Breitsamter
Prüfer*innen der Dissertation:
Prof. Dr.-Ing. Thomas Sattelmayer
Prof. Dr.-Ing. habil. Tobias Sander

Die Dissertation wurde am 27.03.2023 bei der Technischen Universität München eingereicht und durch die TUM School of Engineering and Design am 06.06.2023 angenommen.

Vorwort

Die vorliegende Arbeit entstand im Rahmen meiner Tätigkeit als wissenschaftlicher Mitarbeiter am Lehrstuhl für Thermodynamik der Technischen Universität München. Das Projekt wurde von GE Power und dem Bundesministerium für Wirtschaft und Klimaschutz (BMWK) gefördert (Förderkennzeichen 0324295C). Die Forschung wurde im Rahmen des Verbundprojektes ECOFlex-turbo im Rahmen der AG Turbo durchgeführt. Für die Unterstützung wird an dieser Stelle herzlich gedankt.

Mein besonderer Dank gilt meinem Doktorvater, Prof. Dr.-Ing. Thomas Sattelmayer, für die fachliche Betreuung der Arbeit und das in mich gesetzte Vertrauen. Durch seine Begeisterung für die Verbrennungsforschung sowie seine Expertise auf diesem Gebiet hat er mir immer wieder neue Denkanstöße gegeben. Seine wertvollen Impulse haben maßgeblich zum Erfolg dieser Arbeit beigetragen.

Herrn Prof. Dr.-Ing. habil. Tobias Sander danke ich für die Übernahme des Koreferates sowie die äußerst zügige Begutachtung meiner Arbeit. Weiterhin danke ich Herrn apl. Prof. Dr.-Ing. Christian Breitsamter für die freundliche Übernahme des Prüfungsvorsitzes.

Ein besonderer Dank geht auch an meine Kolleginnen und Kollegen für die freundschaftliche Atmosphäre und die kollegiale Zusammenarbeit. Ich bin sehr dankbar für all die Freundschaften, die sich aus der gemeinsamen Arbeit am Lehrstuhl entwickelt haben. Meinem Kollegen Jan Kaufmann gilt mein ausdrücklicher Dank. Gemeinsam haben wir alle Herausforderungen im Laufe des Forschungsprojektes erfolgreich gemeistert. Ich danke ihm für die inspirierenden Diskussionen im Büro und die kollegiale Zusammenarbeit im Labor. Ebenso danke ich Oberingenieur Dr.-Ing. Christoph Hirsch für die vielen fachlichen Anregungen und ausführlichen Diskussionen zu den unterschiedlichsten wissenschaftlichen Fragestellungen. Insbesondere danke ich Frau Helga

Bassett und Frau Sigrid Schulz-Reichwald für ihre geduldige Hilfe bei sämtlichen organisatorischen und finanziellen Angelegenheiten sowie den Werkstätten für ihre Unterstützung beim Umbau des Prüfstandes.

Außerdem danke ich allen Studierenden und wissenschaftlichen Hilfskräften, die an diesem Forschungsprojekt beteiligt waren. Vielen Dank für euren unermüdlichen Einsatz und eure zuverlässige Mitarbeit. Besonders hervorheben möchte ich hierbei Michael Bachfischer, Jannes Papenbrock und Vinzenz Völkl, die durch exzellente Leistungen einen wesentlichen Beitrag zum Gelingen dieser Arbeit geleistet haben.

Meiner Familie und vor allem meinen Eltern danke ich für ihre bedingungslose Unterstützung und den Rückhalt während meiner gesamten Ausbildung. Ohne ihre Unterstützung wäre diese Arbeit nicht möglich gewesen. Außerdem danke ich meinen Großeltern, die mich während meiner gesamten Ausbildung unterstützt haben und mich stets motiviert haben, diesen Weg einzuschlagen.

Ich widme diese Arbeit meiner Frau Livia, da es keine Worte gibt, die meine Dankbarkeit für ihre Unterstützung ausdrücken. Auch in den schwierigsten Zeiten hat Sie an mich geglaubt und mich motiviert durchzuhalten, wofür ich ihr von Herzen danke.

München, im Juli 2023 Manuel Vogel

Kurzfassung

Äquivalenzverhältnisschwankungen stellen einen zentralen Mechanismus dar, der zum Auftreten thermoakustischer Instabilitäten in mager vorgemischten Gasturbinenbrennkammern beiträgt. Die Quantifizierung des Einflusses von Äquivalenzverhältnisschwankungen auf die Stabilität eines Verbrennungssystems erfordert ein grundlegendes Verständnis der zugrundeliegenden Prozesse. Dazu zählen die Erzeugung von Äquivalenzverhältnisschwankungen am Ort der Kraftstoffzufuhr sowie die Ausbreitung dieser Schwankungen bis zur Flamme.

Die vorliegende Arbeit befasst sich mit der experimentellen Bestimmung von Äquivalenzverhältnisschwankungen mit Hilfe der Chemilumineszenz der Flamme in einer Gasturbinenbrennkammer mit magerer Vormischverbrennung. Die Verbrennung findet unter atmosphärischen Bedingungen statt, wobei sowohl Erdgas als auch Kerosin als Kraftstoff verwendet werden. Spektral aufgelöste Untersuchungen zeigen, dass das CH^*/CO_2^*-Verhältnis sowohl bei der Verbrennung von Erdgas als auch von Kerosin einen eindeutigen Zusammenhang zum globalen Äquivalenzverhältnis aufweist. CH^*- und CO_2^*-Chemilumineszenzsignale werden phasenaufgelöst aufgezeichnet, um die Schwankungen des Äquivalenzverhältnisses während akustischer Anregung für beide Kraftstoffe zu quantifizieren. Es wird beobachtet, dass die Äquivalenzverhältnisschwankungen besonders ausgeprägt sind, solange die konvektive Wellenlänge der Äquivalenzverhältniswelle größer ist als der Abstand zwischen Brennstoffzufuhr und Flamme. Mit zunehmender Frequenz nehmen die Schwankungen deutlich ab und sind schließlich fast vernachlässigbar klein. Es wird gezeigt, dass die Entstehung und Ausbreitung von Schwankungen des Äquivalenzverhältnisses durch die komplexe Gemischaufbereitung von flüssigen Kraftstoffen im Vergleich zu gasförmigen Kraftstoffen erheblich beeinflusst wird. Zur Validierung der vorgestellten Messtechnik wird die extern vorgemischte Erdgasverbrennung untersucht. Es wird ein eindimensionales Transportmodell entwickelt, um die Entstehung und Ausbreitung von Äquivalenzverhält-

nisschwankungen zu modellieren. Das Modell zeigt eine gute Übereinstimmung mit den experimentellen Daten.

Abstract

Equivalence ratio fluctuations constitute one major mechanism driving thermoacoustic instabilities in lean premixed gas turbine combustors. Quantifying the influence of equivalence ratio fluctuations on combustion system stability requires a fundamental understanding of the underlying processes. This includes the generation of equivalence ratio fluctuations at the fuel injection location, as well as the propagation of these fluctuations to the flame.

This thesis deals with the experimental determination of equivalence ratio fluctuations from flame chemiluminescence in a lean premixed gas turbine combustor fueled with natural gas and kerosene under atmospheric conditions. Spectrally resolved investigations reveal that the CH^*/CO_2^* ratio is clearly related to the global equivalence ratio for both natural gas and kerosene combustion. Phase-resolved CH^* and CO_2^* chemiluminescence signals are acquired, quantifying the oscillations of the equivalence ratio during acoustic excitation for both fuels. Equivalence ratio fluctuations are observed to be particularly pronounced as long as the convective wavelength of the equivalence ratio wave is greater than the distance between fuel supply and flame. As the frequency increases, the fluctuations decrease significantly and finally become almost negligible. It is shown that the generation and propagation of equivalence ratio fluctuations is considerably influenced by the more complex mixture preparation of liquid fuels compared to gaseous fuels. Validation of the presented measurement technique is carried out by examining externally premixed natural gas combustion. A one-dimensional transport model is developed to describe the generation and propagation of equivalence ratio oscillations. Good agreement is found between the model and the experimental data.

Contents

List of Figures

List of Tables

Nomenclature

Latin letters

A	Surface area [m^2]
c	Speed of sound [m/s]
c_w	Drag coefficient [-]
d	Diameter [m]
f	Frequency [1/s]
f	Riemann invariant [m/s]
g	Riemann invariant [m/s]
h	Specific enthalpy [J/kg]
$\mathbf{H}$	Coefficient matrix [-]
i	Imaginary unit [-]
$\mathbf{I}$	Identity matrix [-]
I	Chemiluminescence Intensity [W/m^2]
k	Wave number [1/m]
l	Length [m]
L_f	Flame length [m]
m	Mass [kg]
$\dot{m}$	Mass flow [kg/s]
M	Molar mass [kg/kmol]
N_s	Number of shear layers [-]
p	Pressure [N/m^2]
P_{th}	Thermal power [W]
$\dot{Q}$	Heat release rate [W]
R	Specific gas constant [J/kgK]

$R^{+/-}$	Reflection coefficient [-]
S	Swirl number [-]
s	Flame speed [m/s]
SM	Scattering matrix [-]
t	Time [s]
T	Temperature [K]
$T^{+/-}$	Transmission coefficient [-]
TF	Transfer function [-]
TM	Transfer matrix [-]
u	Flow velocity [m/s]
V	Volume [m^3]
x, y, z	Cartesian coordinates [m]
Z	Impedance [-]

Greek letters

α	Temperature coefficient laminar flame speed [-]
Γ	Diffusivity [m^2/s]
ζ	Pressure loss coefficient [-]
λ	Wavelength [m]
μ	Dynamic viscosity [kg/ms]
ν	Kinematic viscosity [m^2/s]
ρ	Density [kg/m^3]
σ	Time delay width [1/s]
τ	Time delay [s]
φ	Phase angle [rad]
ϕ	Equivalence ratio [-]
$\mathbf{\Omega}$	Transformation matrix [-]
ω	Angular frequency [rad/s]

Operators

$\hat{(\,)}$	Amplitude
$(\,)'$	Deterministic (coherent) component
$\lvert\,\rvert$	Magnitude
$\angle(\,)$	Phase
$\langle\,\rangle$	Phase-averaged value
$(\,)^{\dagger}$	Pseudo-inverse
$\tilde{(\,)}$	Random (stochastic) component
$\bar{(\,)}$	Time-averaged value
$(\,)^{\top}$	Transpose

Subscripts

acc	Acceleration
ad	Adiabat
b	Burner outlet
cc	Combustion chamber
cg	Center of gravity
ds	Downstream
eff	Effective
f	Flame
geo	Geometric
h	Hydraulic
inj	Injector
l	Laminar
mix	Mixing
pre	Preheater
st	Stoichiometric
sup	Fuel supply line
T	Transport
t	Turbulent

us	Upstream

Dimensionless numbers

Ma	Mach
Da	Damköhler
Ka	Karlovitz
Pe	Peclet
Re	Reynolds
Sr	Strouhal

Abbreviations

A^2EV	Advanced^2 En-Vironmental burner
CWL	Center wavelength
FFT	Fast fourier transform
FWHM	Full width at half maximum
ICCD	Intensified charge coupled device
II	Image intensifier
LOS	Line-of-sight
MMM	Mulit-microphone method
NGp	Perfectly premixed natural gas operation
NGt	Technically premixed natural gas operation
RMS	Root mean square
SMD	Sauter Mean Diameter
TMM	Two-microphone method
URANS	Unsteady Reynolds-Averaged Navier-Stokes
UV	Ultraviolet

1 Introduction

This chapter outlines the importance of heavy duty gas turbines for power generation in order to cover the increasing demand for electrical energy. First, the advantages of lean premixed combustion are highlighted, as well as the challenges that this combustion technology poses for gas turbine engines. Subsequently, the formation of thermoacoustic instabilities is elucidated. Here, the mechanisms contributing to the development of combustion instabilities are discussed in more detail. Lastly, an outline of this thesis is provided.

1.1 Technological Background

Ensuring a constantly available supply of electricity and heat is one of the main challenges of the energy suppliers. In today's highly fluctuating energy mix with an increasing proportion of renewable energies, gas turbines play a decisive role in ensuring a constant power supply. The fast start-up and flexible operation of gas turbines, especially in terms of part-load efficiency, are key factors here. Modern power plants must comply with the required improvements in reducing pollutant emissions and increasing overall efficiency. In industrialized countries, nitrogen oxides (NO_x) represent one of the main air pollutants [1] [35]. Nitrogen oxides contribute to the formation of photochemical smog and ozone in the troposphere [4]. Also, nitrogen oxides contribute to the stratospheric ozone depletion. This leads to the formation of the ozone hole over Antarctica and causes increased ultraviolet radiation to reach the earth's surface [53].

[1] The term NO_x includes NO and NO_2.

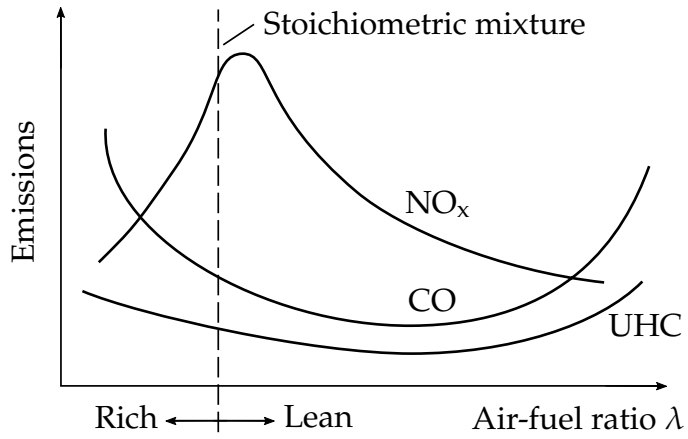

Figure 1.1: The dependence of pollutant emissions on the fuel-air ratio λ=1/ϕ. Adapted from Saravanamuttoo [114].

In combustion systems, thermal NO is formed at high temperatures by decomposition of nitrogen, one of the components present in the air. Thermal NO is formed by the following elementary reactions [129]

$$O + N_2 \longrightarrow NO + N \tag{1.1}$$

$$N + O_2 \longrightarrow NO + O \tag{1.2}$$

$$N + OH \longrightarrow NO + H \tag{1.3}$$

This formation mechanism is also referred to as the Zeldovich mechanism as he first postulated it. NO is predominantly formed in the flame, with oxidation to NO_2 in a subsequent step [21]. Due to the strong triple bond in N_2, Reaction 1.1 has a high activation energy and shows a strong temperature dependency. Thus, thermal NO becomes important only at temperatures of about 1800 K and above [126]. Consequently, flame temperature is the most important factor influencing the formation of NO. In addition to the Zeldovich mechanism, there are other mechanisms leading to the formation of nitrogen oxides, which are not addressed in detail in the present thesis [129]. High NO_x emissions have long been an issue for gas turbines due to the high combustion temperatures associated with non-premixed combustion. Figure 1.1 depicts the pollutant emissions as a function of the fuel-air ratio. In non-premixed combustion systems, the flame stabilizes locally in the regions of stoichiometric mixture, resulting

in high NO_x emissions. NO_x emissions decrease significantly for lean operating conditions. Lean premixed combustion turns out to be a effective strategy for reducing NO_x emissions [16]. However, as shown in Figure 1.1, emissions associated with carbon monoxide (CO) and unburned hydrocarbons (UHC) tend to increase for lean operating conditions.

Modern gas turbine engines used for power generation primarily feature lean premixed combustion to meet applicable regulatory requirements. Here, the mixing process is decoupled from combustion by installing a mixing section upstream of the combustion chamber, being part of the injector. As a result, a homogeneous mixture of air and fuel reaches the combustion chamber and is burned at a uniformly low flame temperature. Changing from diffusion combustion to lean premixed combustion significantly reduces NO_x emissions from hundreds of ppm down to single digit ppm numbers. In addition, modern gas turbines are expected to play a major role in reducing the carbon footprint of power generation [42].

To ensure the economic efficiency of gas turbines even in the event of high prices and short-term shortages of the main gaseous fuel, the implementation of a combustion system with high fuel flexibility in current gas turbine engines is becoming a key objective [22, 82, 132]. Such scenarios are realistic and topical, as demonstrated not least by the politically driven reduction in the supply of natural gas from Eastern Europe and Russia in 2014 as a result of the Crimea crisis [64]. Of central importance in this context is compliance with the legally prescribed NO_x emission limits, as their compliance requires a homogeneous mixing of vaporized fuel and oxidation air. Compared to gaseous fuels, this leads to an increased effort in mixture preparation of liquid fuels and thus considerably increases the complexity of the combustion system. The mixture preparation of liquid fuels consists of the sub-processes atomization, spray propagation and simultaneous evaporation and mixing.

1.2 Thermoacoustic Instabilities

Unfortunately, lean premixed combustion is susceptible to the formation of thermoacoustic instabilities caused by a coupling between acoustic waves in the combustion chamber and fluctuations in the heat release rate [59, 70, 80]. The resulting oscillations can lead to high pressure and temperature amplitudes in the combustion chamber and thereby cause higher emissions and mechanical failure of the system [16]. In response to an acoustic perturbation, the flame reacts with a fluctuation of the heat release rate and therefore acts as a source of sound. The acoustic waves propagate upstream and downstream of the flame to the combustion chamber walls, where they are partially reflected. The reflected waves travel back to the flame again causing an acoustic disturbance in the reaction zone. The instabilities grow if more energy is supplied to the acoustic system by the combustion process than acoustic energy is dissipated within the combustion chamber. In case the dissipating mechanisms prevail, the self-excited oscillation will decrease and the system will become stable. The limit cycle with a constant amplitude is reached when the excitatory and dissipative mechanisms are in equilibrium. In general, combustion instabilities manifest as natural modes at corresponding eigenfrequencies of the combustion system. According to the direction of the oscillations with respect to the combustion chamber geometry, various modes appear, which can be categorized as follows [15, 81]:

- **Longitudinal modes:** The oscillation direction is parallel to the main flow direction in the combustion chamber. The flame can be considered as acoustically compact, implying the acoustic quantities to be constant over the flame area. One-dimensional wave propagation can be presumed with eigenfrequencies in the range between 50 and 1000 Hz [30, 61].
- **Azimuthal modes:** The direction of oscillation is in circumferential direction. Azimuthal modes can be found in annular combustors with eigenfrequencies in the same order of magnitude as for longitu-

dinal modes. Considering adjacent burners of an annular combustor, the azimuthal mode firstly modulates the axial mass flow in the respective burners, but also generates a transverse excitation. Usually it is valid to consider the burner and the flame as acoustically compact [12].

- **Transverse modes:** The oscillation direction is perpendicular to the main flow direction in the combustion chamber. Transverse modes typically occur at eigenfrequencies above 1000 Hz. Acoustics and flame cannot be considered separately as the acoustic field significantly changes over the flame volume. Thus, the flame cannot be assumed to be acoustically compact and the interaction of the flame and acoustics must be analyzed spatially resolved. This results in a multi-dimensional pressure field [95].

This categorization refers to narrow combustion chambers, where the length of the combustion chamber is significantly larger than its height. Mixed modes can also occur, resulting from any combination of the presented modes [50].

1.2.1 The Rayleigh Criterion

The interaction of acoustic pressure fluctuations p' in the combustion chamber with heat release fluctuations $\dot{Q}'$ of the flame can either have a exciting or a damping effect on the thermoacoustic instabilities, depending on the phase difference between these two quantities. This correlation is represented by the Rayleigh criterion [107]. Rayleigh reported the oscillation to grow when the fluctuating heat release is in phase with the pressure fluctuations. Meaning, if heat is added at peak pressure, or removed at minimum pressure, respectively, an instability can grow. Conversely, the oscillation is attenuated when p' and $\dot{Q}'$ are out of phase. Mathematically, this relation can be represented by the Rayleigh integral

as follows [106]:

$$\int_0^T p'(t) \cdot \dot{Q}'(t) dt > 0 \tag{1.4}$$

Here T denotes the oscillation period. Thus, thermoacoustic instabilities in the combustor can only be amplified if the Rayleigh integral is positive. The Rayleigh integral turns positive if the phase difference between p′ and $\dot{Q}'$ becomes smaller than $\pi/2$. For a phase difference exceeding $\pi/2$ the Rayleigh integral becomes negative. However, a positive Rayleigh integral is only a necessary but not a sufficient condition for the formation of thermoacoustic instabilities. This requires an increase in acoustic energy of the system, meaning the energy added to the acoustic field by the flame must exceed the damping and losses in the combustor.

1.2.2 Instability Mechanisms

Over the last decades, a fundamental understanding of the dominant processes for the stability behaviour of gas turbine has been developed. From the studies of flame dynamics in lean premixed combustors, the following mechanisms causing thermoacoustic instabilities were identified, as indicated in Figure 1.2:

- **Turbulent noise:** Turbulent noise results from unsteady combustion due to turbulent flow and flame interaction. This leads to turbulent fluctuations in heat release and results in a broadband spectrum of combustion noise. Selective amplification of the combustion noise corresponding to the eigenfrequencies of the combustor can occur, potentially affecting the flame dynamics. Turbulent noise is largely independent of the thermoacoustic feedback loop, but can serve as a trigger for combustion instabilities [20, 24, 124].
- **Natural and forced coherent flow structures:** Coherent flow structures refer to phenomena such as vortex shedding or any type of periodic flow instability. In the case of forced coherent flow structures, acoustically initiated velocity fluctuations (u′) at the burner outlet

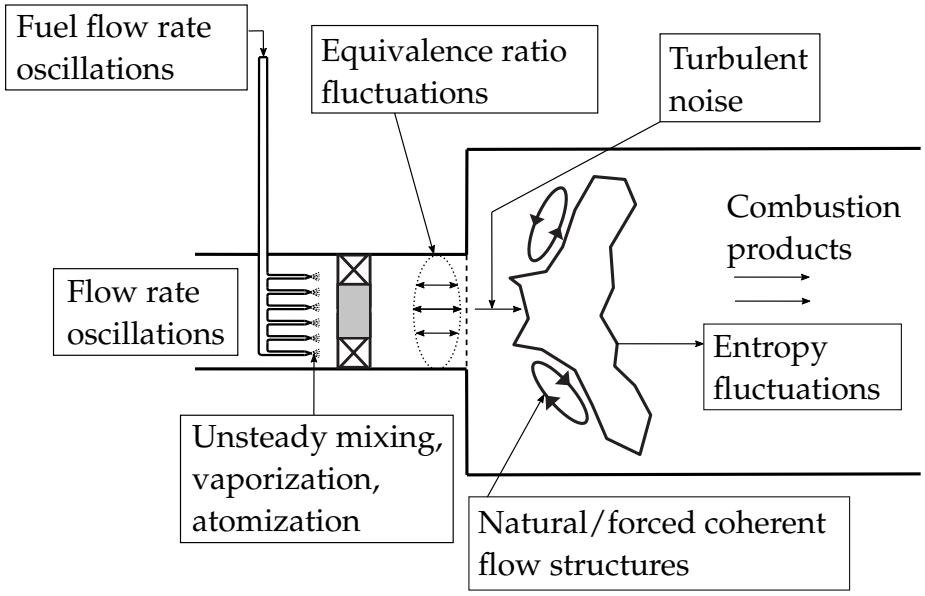

Figure 1.2: Sketch of a lean premixed combustor including the mechanisms driving thermoacoustic instabilities. Adapted from Lieuwen [81].

lead to a large-scale coherent vortex formation of a combustible mixture. If hot product gas penetrates the vortices, they burn abruptly and act as a source of acoustic energy. In addition, the convectively transported vortices cause a fluctuation of the flame surface, which also leads to a modulation of the heat release. Both feedback mechanisms show a corresponding time delay due to the convective transport of the vortices [100, 104, 117]. In the case of swirling flames, swirl fluctuations can additionally contribute to the generation of instabilities [49, 67]. In modelling it is appropriate to use the velocity fluctuation at the burner outlet as a coupling variable. On the basis of experimentally determined amplitude and phase responses between the heat release fluctuations and fluctuations of the coupling variables, semi-analytical models of the flame dynamics could be derived based on typical time delay terms [38]. In contrast, natural coherent structures are independent of the combustor acoustics and thus independent of the thermoacoustic feedback loop.

- **Equivalence ratio fluctuations:** In technically premixed combustion systems, equivalence ratio fluctuations (ϕ') can additionally lead to a fluctuation of the heat release. Acoustic pressure and velocity fluctuations at the fuel injector can cause both air mass flow and fuel mass flow oscillations, resulting in fluctuations of the mixture composition. If an acoustically stiff fuel supply is assumed, equivalence ratio fluctuations result due to the acoustic velocity fluctuations and the resulting air mass flow fluctuations at the location of the fuel supply. This equivalence ratio perturbations are then convectively transported to the flame, leading to fluctuations in the heat release rate both directly in terms of a modulating energy content of the reactive flow and indirectly in terms of a modulation of the flame temperature and the burning rate [17, 60, 79, 110]. This feedback mechanism also results in a characteristic delay time due to convective transport. In the case of liquid fuel injection, the acoustic perturbations may also affect the additional processes of atomization and evaporation [18, 34]. Since this study focuses on the investigation of equivalence ratio fluctuations, a detailed description of this mechanism is given in Section 3.3.

- **Entropy fluctuations:** Entropy fluctuations refers to periodic temperature oscillations resulting, for example, from equivalence ratio fluctuations in the flame. Consequently, local density fluctuations occur due to temperature fluctuations, which are likely to interact with the acoustic field. The entropy waves, transported via strong area contractions such as combustor outlet, impair the reflection of acoustic waves and consequently affect the stability of the combustion system [33, 84, 105].

Turbulent combustion noise and natural coherent flow structures are thus effects largely independent of the thermoacoustic feedback loop. In contrast, forced coherent flow structures, equivalence ratio fluctuations and entropy fluctuations are mechanisms driven by the thermoacoustic feedback loop sustaining combustion instabilities.

1.3 Research Objective and Thesis Outline

This work aims to provide a fundamental understanding of the generation and propagation of equivalence ratio fluctuations in lean premixed gas turbine combustors. In recent years, several studies concerning this topic have already been published for lean premixed gas combustion [13, 14, 55, 73]. However, the generation and propagation of equivalence ratio fluctuations for lean premixed spray combustion has hardly been investigated. Due to the additional sub-processes of atomization and evaporation, a complex interaction of the acoustic velocity fluctuations with the mixture preparation in the mixing tube arises influencing the generation of equivalence ratio fluctuations.

This study investigates equivalence ratio fluctuations in a lean premixed gas turbine combustor fueled with natural gas and kerosene under atmospheric conditions. Within the scope of this work, a downscaled version of the A^2EV burner is extended by a central twin-fluid nozzle to enable the injection of liquid fuel. Thus, equivalence ratio fluctuations can be investigated in both natural gas and liquid fuel operation using the same burner. For this purpose, a measurement technique was first developed to determine the equivalence ratio fluctuations from flame chemiluminescence under atmospheric conditions for both natural gas and kerosene combustion. Applying this measurement technique, experimental investigations can be conducted aiming at the following objectives:

- Validation of the measurement technique.
- Investigation of the influence of different operating conditions on the propagation of equivalence ratio fluctuations for gaseous and liquid fuel injection.
- Quantification of the effects of atomization and evaporation on the propagation of equivalence ratio fluctuations for liquid fuel operation.

- Identification of parameters influencing the propagation of equivalence ratio fluctuations.
- Provide experimental data to develop low-order models to describe the generation and propagation of equivalence ratio fluctuations.

The strategy is to compare the experimentally determined equivalence ratio fluctuations in the flame for both gaseous fuel and liquid fuel injection. This is to identify the fundamental contributions of atomization and evaporation of liquid fuel injection on the generation and propagation of equivalence ratio fluctuations. Last, all these findings are exploited to develop low-order models for predicting the generation and propagation of equivalence ratio fluctuations in lean premixed combustors.

The thesis is structured as follows. In the following two chapters the theoretical background is presented. In Chapter 2, the fundamentals of chemiluminescence are outlined. The spectral characteristics of diatomic molecules are presented. Furthermore, OH* and CH* and CO_2* chemiluminescence is discussed in more detail, especially the reactions that lead to the formation and deactivation of these radicals. A literature review on chemiluminescence as a measurement technique for the equivalence ratio is also presented. Chapter 3 provides the relevant acoustic theory. First, the linear wave equation is derived. By solving the wave equation, a representation of wave propagation in simple ducts is obtained. Different boundary conditions are discussed and the eigenfrequencies of a duct are presented. Low-order network models are also introduced to describe the propagation of waves in acoustic systems. Finally, equivalence ratio fluctuations are discussed in more detail. This includes a mathematical description of the generation and propagation of equivalence ratio fluctuations and a literature review of previous studies including low-order modeling approaches. In Chapter 4 the experimental setup is described. This includes an overview of the atmospheric single burner test rig and a detailed description of the burner utilized for the investigations. Emphasis is placed on the modifications of the burner for the investigation of spray combustion. Chapter 5 introduces the acoustic and optical mea-

surement techniques. First, the multimicrophone method is outlined for reconstructing acoustic pressure and velocity fluctuations in the combustion system. The spectrally resolved measurement technique is presented subsequently, followed by the bandpass filtered measurement technique. In particular, it will be discussed how to determine equivalence ratio fluctuations in the flame using this optical measurement technique. Chapter 6 presents the results of the stationary flame investigations. Here, the relationship between the ratio of different chemiluminescence species and the equivalence ratio for both natural gas and kerosene combustion is highlighted. Chapter 7 shows the results for the investigations of equivalence ratio fluctuations during acoustic excitation. First, the velocity fluctuations at the burner outlet are discussed. Subsequently, the equivalence ratio fluctuations for natural gas and kerosene combustion are analyzed in detail. In the subsequent Chapter 8, a low-order modeling approach is presented to predict the generation and propagation of equivalence ratio fluctuations for both gaseous and liquid fuel injection. Lastly, a summary of this thesis is provided in Chapter 9.

2 Chemiluminescence

The term chemiluminescence describes the emission of light by a molecule when returning from an energetically excited state to the ground state. The prefix "chemi" indicates that the molecule in the excited state is formed by a chemical reaction [41]. Chemiluminescence can be observed in any combustion process. The main contributors to the overall chemiluminescence in hydrocarbon flames are the electronically excited species OH*, CH*, C_2* and CO_2* [40, 69]. The asterisk indicates electronically excited molecules. As these species are mainly formed in the reaction zone, the observation of the flame chemiluminescence is often used as a combustion diagnostic tool. For example, for reaction zone marking, as indicator for the heat release rate or the measurement of the equivalence ratio [26, 72].

Fig. 2.1 shows the individual steps involved in a chemiluminescence reaction. The upper line describes the excited state of a molecule XY* and the lower line its ground state XY. The individual steps can be described in more detail as follows [93]:

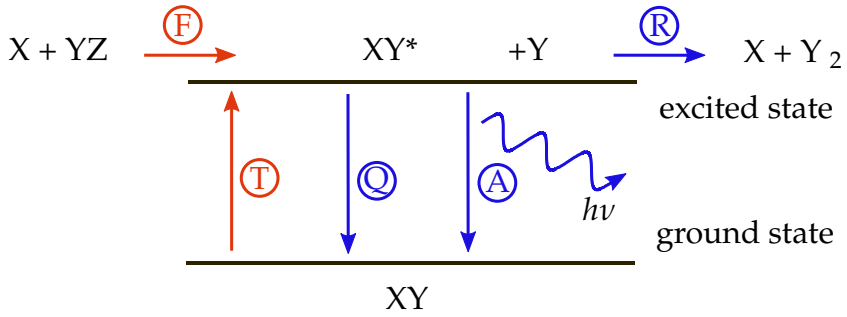

Figure 2.1: Various steps involved in a chemiluminescence reaction. Adapted from Nori [93].

- Formation of the excited state by a chemical reaction (F)
- Formation of the excited state by thermal excitation (T)
- Collisional quenching reaction in which the excited molecule XY* returns to the ground state XY without emitting photons (Q)
- Collision with another molecule leading to a chemical reaction (R)
- Spontaneous returning to the ground state by emitting a photon (A)

The formation and deactivation of electronically excited radicals are in equilibrium under stationary flame conditions. It can thus be assumed that the concentration of radicals is in a quasi-steady state. For an excited radical XY* this can be expressed by the following equation [93]:

$$\frac{d[\mathrm{XY}^*]}{dt} = F + T - Q - R - A \approx 0 \tag{2.1}$$

F and T describe the formation rates of the electronically excited species by chemical reaction or thermal excitation. Q, R and A represent the deactivation rates of the excited species by collisional or reactive quenching and by spontaneous emission of a photon. The emission rate of the photons can thus be described by the following equation [93]:

$$\frac{d[h\nu]}{dt} = A[XY^*] \tag{2.2}$$

Here, h is the Planck constant and ν is the frequency of chemiluminescence emission. A is the Einstein coefficient of spontaneous emission and is often called the spontaneous transition probability. [XY*] is the concentration of the excited state. In combustion research, the OH* radical is usually used for optical investigations of flames.

2.1 Spectral Characteristics of Diatomic Molecules

The spectral characteristics of molecules are considerably more complicated compared to the discrete emission spectra of single atoms [31]. In

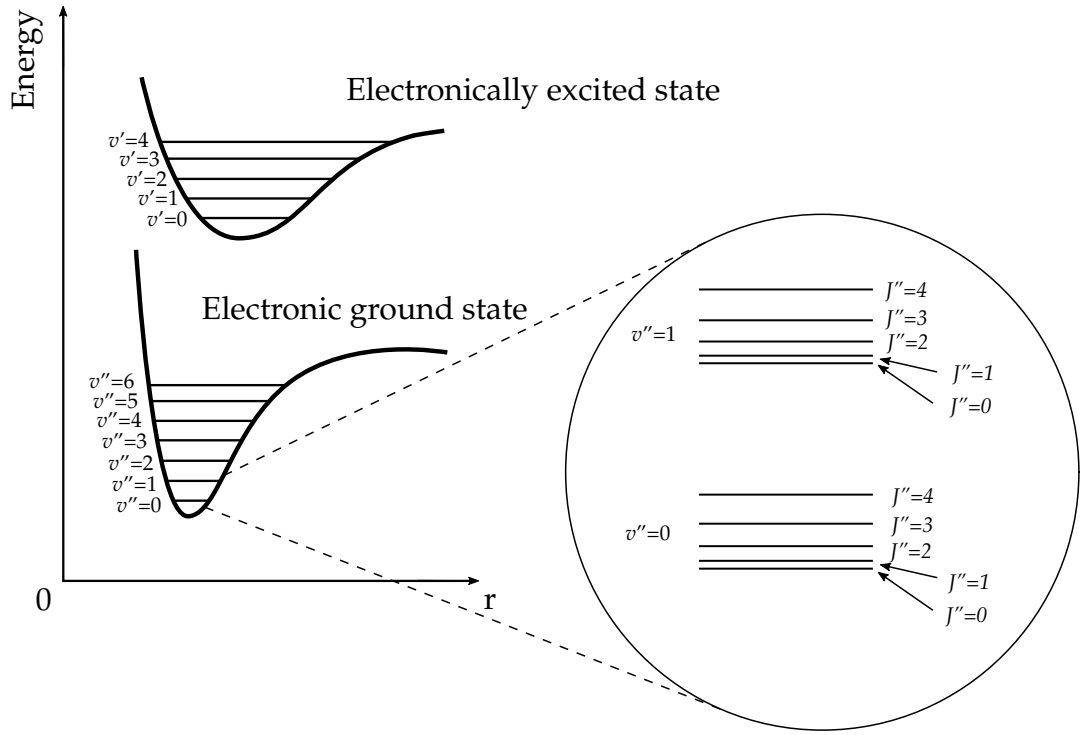

Figure 2.2: Sketch of a diatomic molecule's energy level. The electronic state can be divided into several vibrational states (v). Each vibrational state can be split in several rotational states (J). Adapted from Tipler [125].

hydrocarbon flames, essentially diatomic (OH* and CH*) or triatomic (CO_2*) molecules are mainly contributing to the overall chemiluminescence. This section outlines the spectral characteristics of diatomic molecules in more detail.

According to quantum mechanics, excited molecules can only have discrete energy states. These can be divided into 3 states: the electronic excitation, the vibration of the atoms and the rotation of the molecule around its center of mass. Figure 2.2 schematically shows the electronic excited state and the ground state of a diatomic molecule as well as the vibration and rotational energy states. The inner energy of the molecule is plotted as a function of the average nuclei distance. The vibration and rotation states are labeled with the corresponding quantum numbers (v or J). The energies associated with an electronic transition are in the order of 1 eV.

In contrast, the energy for a vibrational or rotational transition is much smaller. All vibrational and rotational transitions of a molecule can occur when returning from the electronically excited state to the ground state [125].

2.2 Modeling of Reaction Kinetics

The reaction kinetics of the formation and deactivation of chemiluminescence species have been examined in numerous studies [25,56,66,94,112]. In this section, the modeling of the reaction kinetics of OH*, CH*, and CO_2* is further discussed.

2.2.1 OH* Chemiluminescence

The reaction mechanisms for the formation of OH* radicals and the returning of these radicals to their ground state have already been investigated in many theoretical and experimental studies. Three fundamental reactions leading to the formation of OH* radicals have been published by Kathrotia [57]:

$$CH + O_2 \longrightarrow OH^* + CO \tag{2.3}$$

$$CHO + O \longrightarrow OH^* + CO \tag{2.4}$$

$$H + O + M \longrightarrow OH^* + M \tag{2.5}$$

M represents a collision partner, such as H_2O, H_2 or CO_2. Reaction 2.3 is the most common form of OH* formation when burning hydrocarbons [93]. As shown in Fig. 2.1, the OH* radical can return to its ground state in two different ways. The dominant mechanism for returning to the ground state is the collisional quenching (cf. Reaction 2.6). Only a small number of the excited radicals return to the ground state by emitting a photon (cf. Reaction 2.7) [56]:

$$OH^* + M \longrightarrow OH + M \tag{2.6}$$

$$OH^* \longrightarrow OH + \frac{hc}{\lambda} \tag{2.7}$$

The wavelength of the emitted photon depends on the energy level at which the excited molecule returns to the ground state or an excited state in between. Furthermore, OH* radicals can also be deactivated by a reactive collision with another molecule, for example [56]:

$$OH^* + H_2 \longrightarrow H + H_2O \tag{2.8}$$

The emission spectrum of the OH* radical is in the region of 310 nm and thus in the UV range.

2.2.2 CH* Chemiluminescence

Similar to OH* chemiluminescence, there are a number of reactions that lead to the formation of CH* radicals. Research has primarily focused on the following 3 reactions [93]:

$$C_2 + OH \longrightarrow CH^* + CO \tag{2.9}$$

$$C_2H + O \longrightarrow CH^* + CO \tag{2.10}$$

$$C_2H + O_2 \longrightarrow CH^* + CO_2 \tag{2.11}$$

Hall et al. proposed Reaction 2.9 and 2.10 as the dominant CH* formation pathways [45]. They conducted shock tube studies with methane-hydrogen mixtures at high temperatures (1200 K - 2300 K) under atmospheric conditions. They also reported Reaction 2.11 to contribute negligibly to the formation of CH*. The contribution of the Reaction 2.9 to the formation of CH* might become significant for higher-order hydrocarbon combustion (e.g. liquid fuels), as the concentration of C_2 increases in this case [94].

The electronically excited CH* radical can return to the ground state by collisional quenching (cf. Reaction 2.12) or by the emission of a photon (cf. Reaction 2.13) [94].

$$CH^* + M \longrightarrow CH + M \tag{2.12}$$

$$CH^* \longrightarrow CH + \frac{hc}{\lambda} \tag{2.13}$$

M represents again a collision partner. CH* chemiluminescence is most prominent at a wavelength of approximately 431 nm [40]. Hence, CH* chemiluminescence is in the visible range of electromagnetic radiation.

2.2.3 CO_2* Chemiluminescence

Previous studies have shown that the chemiluminescence intensity of CO_2* is directly related to the concentration of CO and O and have reported the following three-body reaction as the main source of CO_2* [112]:

$$CO + O + M \longrightarrow CO_2^* + M \tag{2.14}$$

Return to ground state occurs either by emission of a photon or by collisional quenching [112]:

$$CO_2^* \longrightarrow CO_2 + \frac{hc}{\lambda} \tag{2.15}$$

$$CO_2^* + M \longrightarrow CO_2 + M \tag{2.16}$$

CO_2* exhibits a broadband emission spectrum observable between 300 and 600 nm [10]. It is often referred to as background radiation due to its superposition on the emission spectra of the typical flame observables (like OH* and CH*).

2.3 Equivalence Ratio Measurement From Flame Chemiluminescence

Previous studies highlighted that monitoring flame chemiluminescence is a viable approach for measuring the equivalence ratio in the reaction zone [27, 46, 90]. This section provides a brief literature review addressing equivalence ratio measurements via flame chemiluminescence. Most

common method to measure the equivalence ratio is using intensity ratios of different chemiluminescence species.

The first researcher to establish a relationship between the equivalence ratio and the ratios of various chemiluminescence signals was Clark [19]. He investigated propane-air flames under atmospheric conditions and observed a clear relationship between the C_2^*/CH* ratio and the equivalence ratio. In later studies, Kojima et al. reported a correlation between the OH*/CH*, C_2^*/CH* and C_2^*/OH* ratio and the equivalence ratio in premixed laminar methane-air flames, thus allowing the determination of the local equivalence ratio in the reaction zone [65]. He observed the C_2^*/OH* ratio to be the most sensitive to the equivalence ratio. However, in lean premixed flames, the C_2^* chemiluminescence intensity is very low, indicating ratios involving C_2^* chemiluminescence to be inappropriate for determining the equivalence ratio. Similar observations have been published by Hardalupas and Orain for premixed counterflow flames fueled with natural gas and propane [46, 96, 97]. They found a monotonic relationship between the OH*/CH* ratio and the equivalence ratio, which is independent of the strain rate. These findings were supported by numerical simulations of counterflow flames by Panoutsos [98]. He studied eight different mechanisms with detailed chemistry extended by elementary reactions accounting for the formation and deactivation of OH* and CH* chemiluminescence. The numerical results agreed well with the experimental data. He also found that the OH*/CH* ratio is not affected by the flame strain rates, although the chemiluminescence intensity of individual species strongly depends on the strain rate.

Further studies showed that flame parameters such as turbulence intensity and strain rate have a strong influence on the chemiluminescence intensity of OH* and CH*, but the CH*/OH* ratio is almost independent of these parameters in turbulent flames under atmospheric conditions [44]. Muruganandam et al. investigated the applicability of equivalence ratio sensing for technical applications by studying the OH*/CH* ratio in different natural gas combustors at pressures up to 7.8 bar [90]. They observed that neither slight changes in fuel, nor preheating of air,

nor velocity affect the relation between the OH*/CH* ratio and the equivalence ratio. In addition, a non-monotonic behavior of the OH*/CH* ratio was observed when varying the equivalence ratio with increasing pressure. Lee and Seo studied the chemiluminescence spectrum of a swirl-stabilized flame fueled with kerosene [71]. They observed the OH*/CH* ratio to assume values close to one regardless of the equivalence ratio and the preheating temperature, consequently not exhibiting a monotonic relationship to the equivalence ratio. The C_2^*/CH* ratio was found to be linearly related to the equivalence ratio. They reported the gradient of the C_2^*/CH* ratio to decrease with increasing swirl number. Similar results were published for the combustion of diesel oil by Józsa and Kun-Balog [54]. They also observed a non-monotonic relationship of the OH*/CH* ratio to the equivalence ratio. They also found that the OH*/CH* ratio depends on the atomization air pressure. The C_2^*/CH* and C_2^*/OH* ratios were observed to have a monotonic relationship to the equivalence ratio and also showed very low sensitivity to atomization pressure.

However, the chemiluminescence intensity of these diatomic molecules is superimposed by a broadband background radiation, mainly attributable to CO_2*, as already outlined in Section 2.2.3 [91]. The abovementioned studies have taken this into account, meaning that all ratios have been corrected for background radiation. The influence of background radiation on the relationship between the ratio of different chemiluminescence species and the equivalence ratio has only been addressed in very few studies. The correlation between the C_2^*/CH* ratio without background correction and the equivalence ratio was studied by Reyes et al. for gasoline in a constant volume combustion chamber at pressures up to 10 bar [109]. The C_2^*/CH* ratio was found to be monotonically related to the equivalence ratio for all charge pressures examined. They also observed an increase in the sensitivity of the C_2^*/CH* ratio as charge pressure increased. García-Armingol et al. investigated turbulent swirling flames and reported the CH*/CO_2* ratio to be the only ratio that exhibits a monotonic correlation to the equivalence ratio without background correction [39]. These observations are corroborated by Bobusch et al. [14].

They observed a linear relationship between the CH^*/CO_2^* ratio and the equivalence ratio for lean premixed natural gas combustion, which is also independent of the flame strain rate. The CH^*/CO_2^* ratio increases as the equivalence ratio increases. Yi et al. studied turbulent kerosene flames and found that the chemiluminescence spectrum is very similar to that of gas flames [131].

3 Acoustics

This chapter outlines the fundamentals of acoustics related to thermoacoustic instabilities in lean premixed combustors. First, the wave equation is derived based on the conservation equations. Here, one-dimensional linear wave propagation is discussed in more detail. Subsequently, the convective wave equation is derived, which considers mean flow. Low-order network models are then presented in order to describe the propagation of waves in acoustic systems. In addition, equivalence ratio fluctuations are subject of this chapter, representing one mechanism for triggering combustion instabilities. The generation and propagation of equivalence ratio fluctuations are discussed further. A literature review of previous studies examining equivalence ratio fluctuations is also provided. Finally, modeling approaches to describe the propagation of equivalence ratio fluctuations are presented.

3.1 Linear Acoustics

The propagation of acoustic waves can be described based on the conservation equations for mass (cf. Equation 3.1) and momentum (cf. Equation 3.2) [122]:

$$\frac{D\rho}{Dt} + \rho(\nabla \cdot \mathbf{u}) = 0 \tag{3.1}$$

$$\rho\frac{D\mathbf{u}}{Dt} + \nabla p = 0 \tag{3.2}$$

Body forces are neglected for the conservation equation for momentum. Considering evaporating sprays, the conservation equation for mass is not completely accurate, since an additional source term is present in

this case [23]. However, for the present work, this effect is assumed to be small and is therefore neglected. D describes the material derivative and is defined as follows:

$$\frac{D}{Dt} = \frac{\partial}{\partial t} + \mathbf{u} \cdot \nabla \tag{3.3}$$

For low-frequency oscillations (as studied in the present work), the radial dimensions of the combustor examined are small compared to the axial extension, hence one-dimensional wave propagation can be assumed [87]. Consequently, wave propagation is further considered only along the axial direction. The time-dependent local flow variables can be expressed by a mean value and a fluctuating component yielding:

$$p(x,t) = \bar{p}(x,t) + p(x,t)' \tag{3.4}$$

$$\rho(x,t) = \bar{\rho}(x,t) + \rho(x,t)' \tag{3.5}$$

$$u(x,t) = \bar{u}(x,t) + u(x,t)' \tag{3.6}$$

The fluctuating component of the variables is assumed to be significantly smaller compared to the corresponding mean value. Thus, products of two fluctuating variables are neglected hereafter. Assuming isentropic flows, the following relationship is derived for acoustic pressure and density:

$$p' = c^2 \rho' \tag{3.7}$$

Here c is the speed of sound.

3.1.1 Wave Equation

In this section, the wave equation is derived, neglecting mean flow ($\bar{u} = 0$). Linearizing around the mean value, the conservation equations for mass and momentum can be simplified as follows:

$$\frac{\partial \rho'}{\partial t} + \bar{\rho} \frac{\partial u'}{\partial x} = 0 \tag{3.8}$$

$$\bar{\rho} \frac{\partial u'}{\partial t} + \frac{\partial p'}{\partial x} = 0 \tag{3.9}$$

Partial derivation of the conservation equation for mass (cf. Eq. 3.8) with respect to t and the conservation equation for momentum (cf. Eq. 3.9) with respect to x followed by subtraction of one equation from the other yields the linearized one-dimensional wave equation [103]:

$$\frac{\partial^2 p'}{\partial t^2} - c^2 \frac{\partial^2 p'}{\partial x^2} = 0 \tag{3.10}$$

An analytical solution of the wave equation can be derived using d'Alembert's method:

$$\frac{p'}{\bar{\rho} c}(x,t) = f(x - ct) + g(x + ct) \tag{3.11}$$

Here, f and g represent waves traveling upstream and downstream, respectively, specified by boundary and initial conditions. They are also referred to as Riemann invariants. Substituting the general solution of the wave equation (cf. Eq. 3.11) into the linearized conservation equation of momentum (cf. Eq. 3.9), the acoustic velocity is given in terms of f and g as:

$$u'(x,t) = f(x - ct) - g(x + ct) \tag{3.12}$$

Simplified, Equations 3.11 and 3.12 can be represented as follows:

$$\frac{p'}{\bar{\rho} c} = f + g \tag{3.13}$$

$$u' = f - g \tag{3.14}$$

Reshaping Equations 3.13 and 3.14 yields the expression for the Riemann invariants f and g:

$$f = \frac{1}{2}\left(\frac{p'}{\bar{\rho} c} + u'\right) \tag{3.15}$$

$$g = \frac{1}{2}\left(\frac{p'}{\bar{\rho} c} - u'\right) \tag{3.16}$$

Assuming the time-dependent Riemann invariants being harmonic functions, they can be expressed as follows [28]:

$$\frac{p'}{\bar{\rho} c}(x,t) = f \cdot e^{(i\omega t - ikx)} + g \cdot e^{(i\omega t + ikx)} \tag{3.17}$$

$$u'(x,t) = f \cdot e^{(i\omega t - ikx)} - g \cdot e^{(i\omega t + ikx)} \tag{3.18}$$

Here ω represents the angular frequency ($\omega = 2\pi f$) and k the wavenumber, which is defined as follows:

$$k = \frac{\omega}{c} \tag{3.19}$$

3.1.2 Convective Wave Equation

The convective wave equation, accounting for mean flow ($\bar{u} \neq 0$), can be derived in a similar manner as outlined in the previous section. Again, the conservation equations for mass and momentum can be simplified by linearizing around the mean as follows:

$$\left(\frac{\partial}{\partial t} + \bar{u}\frac{\partial}{\partial x}\right)\frac{p'}{c^2} + \bar{\rho}\frac{\partial u'}{\partial x} = 0 \tag{3.20}$$

$$\bar{\rho}\left(\frac{\partial u'}{\partial t} + \bar{u}\frac{\partial u'}{\partial x}\right) + \frac{\partial p'}{\partial x} = 0 \tag{3.21}$$

The convective wave equation can be derived from the linearized conservation equations for mass (cf. Eq. 3.20) and momentum (cf. Eq. 3.21), yielding [103]:

$$\left(\frac{\partial}{\partial t} + \bar{u}\frac{\partial}{\partial x}\right)^2 p' - c^2\frac{\partial^2 p'}{\partial x^2} = 0 \tag{3.22}$$

The solutions of the convective wave equation are given by:

$$\frac{p'(x,t)}{\bar{\rho}c} = f(x - (c + \bar{u})t) + g(x + (c - \bar{u})t) \tag{3.23}$$

$$u'(x,t) = f(x - (c + \bar{u})t) - g(x + (c - \bar{u})t) \tag{3.24}$$

Here, f is a wave propagating in flow direction with propagation speed c+ū, and g is a wave traveling with c-ū against flow direction. Again, assuming harmonic functions for f and g, these equations can be expressed as follows [28]:

$$\frac{p'}{\bar{\rho}c}(x,t) = f \cdot e^{\left(i\omega t - ik^+ x\right)} + g \cdot e^{\left(i\omega t + ik^- x\right)} \tag{3.25}$$

$$u'(x,t) = f \cdot e^{\left(i\omega t - ik^+ x\right)} - g \cdot e^{\left(i\omega t + ik^- x\right)} \tag{3.26}$$

Here, $k^{\pm}$ describes the convective wave number, which is defined as follows:

$$k^{\pm} = \frac{\omega}{c \pm \bar{u}} \tag{3.27}$$

3.1.3 Reflection Coefficient and Impedance

The reflection coefficient or the impedance can be utilized to characterize the boundary conditions of an acoustic system. The frequency dependent reflection coefficient represents the ratio between the reflected wave and the incident wave and is given by:

$$R = \frac{g}{f} \tag{3.28}$$

Considering a rigid wall resulting in a vanishing acoustic velocity ($u'=0$), the reflection coefficient becomes 1. In case of an open end, the acoustic pressure vanishes ($p'=0$) and the reflection coefficient is -1. A special case is given for an anechoic end, implying the incident wave f is not being reflected, thus yielding a reflection coefficient of zero.

The acoustic impedance Z is defined as the ratio of acoustic pressure to velocity, yielding:

$$Z = \frac{1}{\bar{\rho} c} \frac{p'}{u'} \tag{3.29}$$

Based on Equation 3.28 and 3.29, a relationship between the impedance and the reflection coefficient is obtained as follows:

$$Z = \frac{f+g}{f-g} = \frac{1+R}{1-R} \tag{3.30}$$

Table 3.1 presents an overview of the reflection coefficient and impedance for different boundary conditions.

Table 3.1: Reflection coefficient and impedance for different boundary conditions.

Boundary condition	Reflection coefficient R	Impedance Z
Open end	-1	0
Rigid wall	1	∞
Anechoic end	0	1

3.1.4 Eigenfrequencies of a Duct

Based on the solution of the wave equation, with the Riemann invariants being harmonic functions (cf. Eq. 3.17 and 3.18), the natural modes in a duct with constant cross section can be analyzed. For a duct with length l and rigid walls at both ends, implying that the acoustic velocity is zero ($u'(x = 0, t) = u'(x = l, t) = 0$), only the following values of the wave number satisfy the boundary conditions [80]:

$$k = \frac{n\pi}{l}, \quad n = 0, 1, 2, \ldots \tag{3.31}$$

Thus, the eigenfrequencies of the duct are given by:

$$f_n = \frac{\omega}{2\pi} = \frac{kc}{2\pi} = \frac{nc}{2l} \tag{3.32}$$

Hence, the eigenfrequencies are integer multiples of the first natural mode, implying $f_2 = 2f_1, f_3 = 3f_1$ and so on. The n=1 mode shape represents half a sine wave and is commonly known as $1/2$ wave mode. Equation 3.32 also applies to a duct with open ends on both sides, which means that the acoustic pressure fluctuations vanish ($p'(x = 0, t) = p'(x = l, t) = 0$).

For mixed boundary conditions, such as $u'(x = 0, t) = p'(x = l, t) = 0$, the eigenfrequencies of the duct are derived as follows:

$$f_n = \frac{(2n - 1)c}{4l}, \quad n = 0, 1, 2, \ldots \tag{3.33}$$

Here the eigenfrequencies are odd multiples of the first natural mode, meaning $f_2 = 3f_1, f_3 = 5f_1$ and so on. The n=1 mode shape corresponds to a quarter sine wave and is often referred to as $1/4$ wave mode.

Finally, periodic boundary conditions are discussed. That means that either the unsteady acoustic pressure or the acoustic velocity is equal at both ends, resulting in $p'(x = 0, t) = p'(x = l, t)$ or $u'(x = 0, t) = u'(x = l, t)$. For the periodic boundary conditions, the eigenfrequency of a duct is given by:

$$f_n = \frac{nc}{l}, \quad n = 0, 1, 2, \ldots \tag{3.34}$$

3.2 Low Order Network Modeling

The propagation of waves in acoustic systems is commonly described using low order network models [88, 89]. The description of a system is based on networks of elements with known acoustic properties. The acoustic element is considered as a two-port system, consisting of two inputs and two outputs each. The acoustic properties of each element are represented by transfer matrices that linearly link the acoustic state variables upstream (x_{us}) and downstream (x_{ds}) of the element. Such a network can include analytically, numerically, or experimentally derived elements. Basic elements like ducts, joints, forks or area jumps can be analytically expressed [36]. The transfer matrix does not specify the detailed physical processes in the corresponding element, however it describes how state vectors propagate across the system boundaries of the acoustic element. In particular, thermoacoustic systems are usually represented by acoustic network models [99,100,120,121]. The transfer matrix couples either the Riemann invariants f and g or the acoustic pressure and velocity

fluctuations upstream and downstream of the element as follows [123]:

$$\begin{bmatrix} f \\ g \end{bmatrix}_{ds} = \underbrace{\begin{bmatrix} \mathrm{TM}_{11} & \mathrm{TM}_{12} \\ \mathrm{TM}_{21} & \mathrm{TM}_{22} \end{bmatrix}}_{\mathbf{TM}^{\mathrm{fg}}} \begin{bmatrix} f \\ g \end{bmatrix}_{us} \tag{3.35}$$

$$\begin{bmatrix} \frac{p}{\bar{\rho}c} \\ u \end{bmatrix}_{ds} = \underbrace{\begin{bmatrix} \mathrm{TM}_{11} & \mathrm{TM}_{12} \\ \mathrm{TM}_{21} & \mathrm{TM}_{22} \end{bmatrix}}_{\mathbf{TM}^{\mathrm{pu}}} \begin{bmatrix} \frac{p}{\bar{\rho}c} \\ u \end{bmatrix}_{us} \tag{3.36}$$

A conversion of the transfer matrix $\mathbf{TM}^{\mathrm{fg}}$ to $\mathbf{TM}^{\mathrm{pu}}$ and vice versa is possible via the following linear transformation [8]

$$\mathbf{TM}^{\mathrm{pu}} = \mathbf{\Omega} \cdot \mathbf{TM}^{\mathrm{fg}} \cdot \mathbf{\Omega}^{-1} \tag{3.37}$$

$$\mathbf{TM}^{\mathrm{fg}} = \mathbf{\Omega}^{-1} \cdot \mathbf{TM}^{\mathrm{pu}} \cdot \mathbf{\Omega} \tag{3.38}$$

Here $\mathbf{\Omega}$ represents a transformation matrix and $\mathbf{\Omega^{-1}}$ the corresponding inverse transformation matrix, which are defined as follows:

$$\mathbf{\Omega} = \begin{bmatrix} 1 & 1 \\ 1 & -1 \end{bmatrix} \tag{3.39}$$

$$\mathbf{\Omega}^{-1} = \frac{1}{2} \begin{bmatrix} 1 & 1 \\ 1 & -1 \end{bmatrix} \tag{3.40}$$

Another convenient representation of the acoustic properties of the element is the scattering matrix $\mathbf{SM}^{\mathrm{fg}}$. The scattering matrix links the waves traveling towards the element from both directions ($\mathrm{f_{us}}$ and $\mathrm{g_{ds}}$) with the waves traveling outwards ($\mathrm{g_{us}}$ and $\mathrm{f_{ds}}$) as follows [1]:

$$\begin{bmatrix} f_{ds} \\ g_{us} \end{bmatrix} = \underbrace{\begin{bmatrix} T^{+} & R^{-} \\ R^{+} & T^{-} \end{bmatrix}}_{\mathbf{SM}^{\mathrm{fg}}} \begin{bmatrix} f_{us} \\ g_{ds} \end{bmatrix} \tag{3.41}$$

The acoustic element can be interpreted in terms of a scattering process. The waves entering the element are decomposed into a transmitted and a reflected wave, which is specified by the complex transmission (T^+, T^-) and reflection coefficients (R^+, R^-) of the scattering matrix. A conversion between the transfer matrix $\mathbf{TM}^{\mathrm{fg}}$ and the scattering matrix $\mathbf{SM}^{\mathrm{fg}}$ is possible using the following transformation [36]:

$$\mathbf{SM}^{\mathrm{fg}} = \frac{1}{\mathrm{TM}_{22}^{\mathrm{fg}}} \begin{bmatrix} \mathrm{TM}_{11}^{\mathrm{fg}}\mathrm{TM}_{22}^{\mathrm{fg}} - \mathrm{TM}_{12}^{\mathrm{fg}}\mathrm{TM}_{21}^{\mathrm{fg}} & \mathrm{TM}_{12}^{\mathrm{fg}} \\ -\mathrm{TM}_{21}^{\mathrm{fg}} & 1 \end{bmatrix} \tag{3.42}$$

3.3 Equivalence Ratio Fluctuations

As briefly addressed in Section 1.2.2, equivalence ratio fluctuations represent one mechanism for triggering thermoacoustic instabilities, which will be discussed in more detail in this section. First, the generation and propagation of equivalence ratio fluctuations are examined. Subsequently, a brief review of previous studies concerning equivalence ratio fluctuations is presented. Finally, a modeling approach to describe the propagation of equivalence ratio waves is provided.

3.3.1 Generation and Propagation of Equivalence Ratio Fluctuations

Acoustic pressure and velocity oscillations at the fuel injection location result in fluctuations of the air and fuel mass flow and thus lead to fluctuations of the equivalence ratio. A sketch of a typical lean premixed combustion system to visualize the generation and propagation of equivalence ratio fluctuations is given in Figure 3.1. After the equivalence ratio waves are generated at the location of fuel injection, they are convectively transported to the flame. Due to convective transport, there is a time delay between the generation of the equivalence ratio wave and its arrival in the reaction zone. The overall time delay can be separated into a time

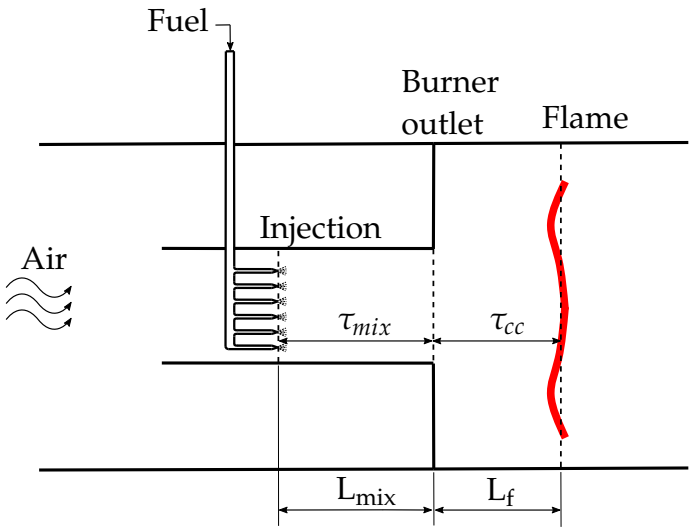

Figure 3.1: Sketch of a lean premixed combustion system to illustrate the generation and transport of equivalence ratio fluctuations. Adapted from Freitag [38].

delay in the mixing tube τ_{mix} and a time delay in the combustion chamber τ_{cc}. A detailed description of the individual time delays is provided in Section 8.2. The equivalence ratio ϕ is defined as the ratio of fuel mass flow rate to air mass flow rate in relation to the ratio for stoichiometric combustion and is given by [126]:

$$\phi = \frac{\left(\dot{m}_{fuel}/\dot{m}_{air}\right)}{\left(\dot{m}_{fuel}/\dot{m}_{air}\right)_{st}} \tag{3.43}$$

After linearization, the equivalence ratio fluctuations at the fuel injection location are obtained [79]:

$$\frac{\phi'_{inj}}{\bar{\phi}_{inj}} = \frac{\dot{m}'_{fuel,inj}}{\bar{\dot{m}}_{fuel,inj}} - \frac{\dot{m}'_{air,inj}}{\bar{\dot{m}}_{air,inj}} \tag{3.44}$$

Using Bernoulli's equation, the fuel mass flow rate at the injector can be calculated as follows [38]:

$$\dot{m}_{fuel,inj} = A\sqrt{\frac{2\Delta p \rho_{fuel}}{\zeta}} \tag{3.45}$$

Here A represents the cross-sectional area of the fuel orifices, ρ_{fuel} is the density of the fuel, and ζ is the pressure loss coefficient. The pressure

drop Δp is given by the instantaneous pressure upstream (i.e. in the fuel supply line) and downstream of the fuel orifice:

$$\Delta p = \left(\bar{p}_{sup} + p'_{sup}\right) - \left(\bar{p}_{inj} + p'_{inj}\right) \tag{3.46}$$

After linearization, the following equation is derived for the fluctuations of the fuel mass flow rate:

$$\frac{\dot{m}'_{fuel,inj}}{\bar{\dot{m}}_{fuel,inj}} = \frac{p'_{sup}}{2\bar{\Delta p}} - \frac{p'_{inj}}{2\bar{\Delta p}} \tag{3.47}$$

If the pressure drop is high, the fuel supply line can be assumed to be acoustically decoupled ($\Delta p \gg p_{sup}'$). If the pressure drop is also significantly larger than the pressure fluctuations in the burner ($\Delta p \gg p_{inj}'$), the fuel injection is considered to be choked, resulting in $\dot{m}'_{fuel,inj} = 0$.

Assuming choked injection and neglecting density fluctuations, a correlation between the fluctuations of the equivalence ratio and the velocity fluctuations at the injector can be derived [115]. If the distance between the injector and burner outlet is considerably smaller than the acoustic wavelength of interest, the acoustic quantities at these locations can be considered identical [38]. In this study, only low-frequency oscillations up to f=400 Hz are investigated, so the burner can be assumed to be acoustically compact. The generation of equivalence ratio fluctuations at the injector can thus be formulated as follows:

$$\frac{\phi'_{inj}}{\bar{\phi}_{inj}} = -\frac{u'_{inj}}{\bar{u}_{inj}} = -\frac{u'_b}{\bar{u}_b} \tag{3.48}$$

Here, the subscript b denotes the burner outlet. Thus, the generation of equivalence ratio fluctuations at the injector is directly proportional to the velocity fluctuations at the burner outlet. The negative proportionality coefficient implies that as the air flow velocity (and thus the air mass flow rate) increases, the equivalence ratio decreases and vice versa.

After generation, the mixture fraction perturbations are convectively transported with the local flow velocity to the flame, being subjected to diffusion and dispersion [78, 115]. Arriving at the flame, they lead to a

modulation of the heat release rate. Owing to the fairly low convection velocity, a large time delay τ_ϕ can occur. The equivalence ratio fluctuations may cause a modulation of the heat release rate in several ways. First, the oscillating energy content of the reactive flow results in a modulation of the heat release rate. In addition, the burning velocity depends on the equivalence ratio. This also affects the surface area of the flame, also contributing to the heat release rate modulation [119].

A transfer function is derived relating equivalence ratio fluctuations in the flame to velocity oscillations at burner outlet, reading:

$$TF_\phi = \frac{\phi'_f / \bar{\phi}_f}{u'_b / \bar{u}_b} \tag{3.49}$$

The transfer function is referred to as equivalence ratio transfer function TF_ϕ. A similar approach describing the propagation of equivalence ratio fluctuations was reported by Kather referred to as mixing transfer function [55]. The low frequency limit behavior of the equivalence ratio transfer function (cf. Eq. 3.49) therefore results from Equation 3.48:

$$\lim_{\omega \to 0} |TF_\phi| = 1 \tag{3.50}$$

$$\lim_{\omega \to 0} \angle(TF_\phi) = \pi \tag{3.51}$$

According to the Rayleigh criterion, an instability can occur when pressure and heat release fluctuations at the flame are in phase [107]. If the equivalence ratio fluctuations result in a modulation of the heat release rate that is in phase with the pressure fluctuation, they can significantly contribute to the occurrence of thermoacoustic instabilities. Consequently, the convective time delay of the equivalence ratio wave τ_ϕ is of crucial importance for driving combustion instabilities.

3.3.2 Literature Review

The influence of acoustic waves on the formation and propagation of equivalence ratio waves has been investigated in many studies, espe-

cially in the context of premixed combustion [17, 105, 110, 115, 116, 121]. Equivalence ratio fluctuations were first reported by Keller [60]. He studied the generation and propagation of entropy waves and identified equivalence ratio oscillations causing entropy waves. Lieuwen and Hubbard successfully demonstrated that the convective time delay of the equivalence ratio wave from injector to flame significantly influences the stability of the combustion process [51,79]. They showed that the ratio of convective time delay to acoustic period is of major importance to adequately describe the instability behavior of the combustor under investigation.

Several studies have already been published on the experimental determination of equivalence ratio fluctuations using different measurement techniques. Lee investigated equivalence ratio fluctuations during unstable combustion in the mixing section of the combustor using direct absorption spectroscopy (DAS) [73, 74]. The infrared absorption technique allows the determination of the hydrocarbon concentration in the unburned mixture. He identified equivalence ratio fluctuations to be the main driver for the heat release fluctuations observed at the unstable operating conditions investigated in this work. Li and Blümner utilized wavelength modulation spectroscopy (WMS) to study equivalence ratio fluctuations [13, 76]. WMS shows advantages compared to DAS in terms of improved sensitivity and accuracy. Blümner experimentally determined equivalence ratio fluctuations at two different axial positions in the mixing tube in order to describe the propagation of equivalence ratio waves. He compared his results to two different models that account for diffusion and dispersion and revealed substantial differences. He suggested that coherent oscillations of the transport velocity significantly affect the mixing process and thus the propagation of the equivalence ratio waves.

Bobusch and Kather investigated equivalence ratio oscillations in the reaction zone of the combustor based on chemiluminescence measurements [14, 55]. They utilized the relationship between the CH*/CO_2* ratio and the equivalence ratio, as already outlined in Section 2.3, to resolve

the equivalence ratio fluctuations spatially and temporally in the reaction zone. Kather showed that the simplified model describing the generation of equivalence ratio fluctuations at the injector (cf. Eq. 3.48) applies to linear acoustic forcing amplitudes, but not to nonlinear amplitudes. He indicated that a one-dimensional transport model accounting for turbulent diffusion and dispersion adequately describes the propagation of equivalence ratio fluctuations.

The influence of equivalence ratio fluctuations on the heat release rate was studied by Bade [8]. She compared FTFs of a perfectly premixed combustion to FTFs of a technically premixed combustion and showed that the influence of equivalence ratio fluctuations in the low frequency range leads to a reduction of the FTF amplitude. At high frequencies, however, there is no difference between the perfectly and technically premixed case. This leads to the conclusion that equivalence ratio fluctuations no longer play a role in this range. It has also been shown that equivalence ratio fluctuations can be reduced by choosing a longer mixing tube, which is useful for improving combustion stability.

In all the studies presented, natural gas has been used as fuel. However, for the combustion of liquid fuels, the formation and propagation of equivalence ratio fluctuations has hardly been investigated so far. For liquid fuel combustion, additional sub-processes involving fuel atomization and evaporation may act as sources of instabilities influencing the generation of equivalence ratio waves. This leads in particular to a different route for the formation of equivalence ratio fluctuations at the burner outlet.

The influence of acoustic velocity fluctuations on the atomization and thus on the droplet size distribution for non-premixed, rich combustion was published by Eckstein [32]. He observed that even small velocity fluctuations can significantly affect the droplet size distribution and thus cause a significant modulation of the heat release rate. The velocity fluctuations in the atomization area are a direct response to the pressure fluctuations in the combustion chamber. He reported the unstable oscillation

frequency to be dominated by the transport and combustion time scales of the droplets. Christou examined the influence of air mass flow oscillations on the atomization process of a prefilming airblast atomizer [18]. He observed that air mass flow fluctuations lead to an oscillation of the Sauter Mean Diameter of the droplets as well as a modulation of the droplet velocity. He proposed that the oscillating air flow results in time-dependent segregation of the droplets, leading to unsteady spray characteristics.

3.3.3 Low Order Modeling Approaches

Several one-dimensional models describing the generation and propagation of equivalence ratio fluctuations have already been published. Lieuwen presented a model in which the generated equivalence ratio fluctuations are convected from the injector to the flame [79]:

$$\phi'_f(x,t) = \phi'_{inj} e^{i\omega(t-x/\bar{u})} \tag{3.52}$$

The model describes the propagation of the equivalence ratio wave in axial direction with mean flow velocity $\bar{u}$. This model reflects a pure time delay of the equivalence ratio wave and neglects effects such as dispersion and diffusion. The equivalence ratio wave consequently arrives at the flame with a time delay, but with the same amplitude as at the injector.

To account for the effects of distributed fuel injection, flame shape, and diffusion, Schuermans et al. proposed a model with distributed time delays to describe the propagation of equivalence ratio waves [119]. Assuming a Gaussian distribution of the time delays, the model can be expressed in the frequency domain as follows:

$$\phi'_f(\omega) = \phi'_{inj}(\omega) e^{-i\omega\tau_\phi - \frac{1}{2}\omega^2\sigma_\phi^2} \tag{3.53}$$

Here τ_ϕ indicates the time delay of the equivalence ratio wave from injector to flame and σ_ϕ the standard deviation of the time delay. Based on

Equation 3.53, it can be seen that the fluctuations of the equivalence ratio at the flame vanish in case of high frequencies or large values of σ_ϕ.

A similar approach was presented by Sattelmayer, taking dispersive effects into account [115]:

$$\begin{aligned}\frac{\phi'_f(\omega)}{\phi'_{inj}(\omega)} =& \frac{1}{2\Delta\tau(i\omega)^2} e^{-i\omega\tau_\phi} \left[e^{i\omega\Delta\tau} \left(\frac{\Delta C}{C} + i\omega - \frac{\Delta C}{C}\Delta\tau i\omega \right) \right. \\ & \left. - e^{-i\omega\Delta\tau} \left(\frac{\Delta C}{C} + i\omega + \frac{\Delta C}{C}\Delta\tau i\omega \right) \right]\end{aligned} \tag{3.54}$$

The equation represents the dispersion of the equivalence ratio wave with respect to the minimum ($\tau_\phi - \Delta\tau$) and maximum ($\tau_\phi + \Delta\tau$) delay time. $\frac{\Delta C}{C}$ denotes the gradient of the probability density function between those two delay times.

Blümner modeled the propagation of equivalence ratio fluctuations as a one-dimensional convection-diffusion process, reading [13]:

$$\frac{\phi'_f(\omega)}{\phi'_{inj}(\omega)} = \exp\left[\frac{\mathrm{Pe}}{2} \left(1 - \sqrt{1 + i2\pi \mathrm{Sr}_T \frac{4}{\mathrm{Pe}}} \right) \right] \tag{3.55}$$

Here Pe represents the Peclet number (indicating the ratio of diffusive time delay to convective time delay) and is defined as follows:

$$\mathrm{Pe} = \frac{\tau_d}{\tau_c} = \frac{\bar{u} l}{\Gamma_{\mathrm{eff}}} \tag{3.56}$$

Γ_{eff} is an effective diffusivity, $\bar{u}$ the bulk flow velocity and l the distance between injector and flame. The transport Strouhal number includes the frequency dependency and is obtained as follows:

$$\mathrm{Sr}_T = \frac{f l}{\bar{u}} \tag{3.57}$$

3.3.4 Time Delay Modeling

This section provides an approach to estimate the time delay of the equivalence ratio oscillation τ_ϕ based on one-dimensional physical models.

Three individual processes that contribute to the overall delay are presented.

The first process describes the time delay in the mixing tube τ_{mix}, thus the convective transport from injector to burner outlet. In this section, incompressible flow is assumed due to constant temperatures and low Mach numbers. The axial velocity u(x) is calculated along the burner axis based on the continuity equation considering the burner geometry. A block profile in radial direction is assumed for the axial velocity. The time delay in the mixing tube τ_{mix} is calculated by integrating the reciprocal of the axial velocity along the burner axis from the position of fuel supply to burner outlet [38]:

$$\tau_{\text{mix}} = \int_{x_{\text{inj}}}^{x_{\text{b}}} \frac{1}{u(x)}\, dx \tag{3.58}$$

The second process describes the time delay in the combustion chamber τ_{cc}, meaning from burner outlet to flame. A model for predicting the time delay τ_{cc} was introduced by Alemela [5, 6]:

$$\tau_{cc} = C_\tau \left[\frac{L_f}{\bar{u}_b} \left[1 + \frac{C}{2} \left(\frac{T_{cc}}{T_{pre}} - 1 \right) \right]^{-1} \right] \tag{3.59}$$

Here, C_τ and C are proportionality factors. The present thesis uses the same values as those calibrated by Alemela. T_{pre} is the preheating temperature and T_{cc} the temperature in the combustion chamber. The temperature in the combustion chamber is calculated taking heat losses into account, analogous to the procedure proposed by Bade [8]. L_f represents the flame length. The flame length is calculated using the improved flame length model from Alemela [5]:

$$L_f = 0.247 \cdot L_{f,geo} \cdot Re_t^{0.2} \cdot Ka^{0.076} \tag{3.60}$$

$L_{f,geo}$ indicates the flame length according to the geometric model of Alemela [6]. Alemela approximates the flame shape by a conical shell, with the angle and surface area determined by the swirl jet angle and turbulent flame speed. The turbulent flame speed is calculated according

to Schmid as follows [118]:

$$s_t = s_l + u_t \cdot \left(1 + Da_t^{-2}\right)^{-0.25} \tag{3.61}$$

Here, s_l is the laminar flame speed calculated for natural gas based on the correlation of Liao [77] and for kerosene using the correlation of Wu [130]. Further, u_t denotes the root mean square of the fluctuating velocity and Da_t represents the turbulent Damköhler number, which is calculated as follows [6]:

$$Da_t = 0.09 \frac{l_t}{u_t} \cdot \frac{s_l^2}{\nu} \tag{3.62}$$

Here l_t describes the turbulent length scale and ν the kinematic viscosity. A detailed description of the geometric flame length model and its parameters is given by Alemela [6]. The improved model (cf. Eq. 3.60) takes into account the influence of the turbulent Reynolds number Re_t and the Karlovitz number Ka_t, which are defined as follows [6]:

$$Re_t = \frac{u_t \cdot l_t}{\nu} \tag{3.63}$$

$$Ka = \frac{\sqrt{Re_t}}{Da_t} \tag{3.64}$$

Deviating from Alemela, the turbulent quantities are determined using turbulence correlations, which have already been appropriately adapted to the A^{2}EV burner by Bade [8]. The turbulent quantities of the swirling jet are determined at two-thirds of the flame length. The fluctuating velocity is given by:

$$\frac{u_t}{\bar{u}_b} = \begin{cases} \frac{u_{t,0}}{\bar{u}_b} + 0.2 \cdot \frac{f_{core}}{6.57} \cdot \frac{x}{d_h} & \text{for } \frac{x}{d_h} \leq \frac{6.57}{f_{core}} \\ \frac{1.315}{f_{core}} \cdot \frac{d_h}{x} \end{cases} \tag{3.65}$$

Here d_h is the hydraulic diameter of the annular jet and $\frac{u_{t,0}}{\bar{u}_b}$=0.1 is assumed. f_{core} represents the core area factor and is determined as follows:

$$f_{core} = \frac{N_s}{\cos\left(\arctan\left(S_{eff}\right)\right) \cdot \cos\left(\arctan\left(0.9 \cdot S_{eff}\right)\right)} \tag{3.66}$$

N_s denotes the number of shear layers, which is two in the case of the swirling jet and S_{eff} represents the effective swirl number. The turbulent length scale is given by:

$$\frac{l_t}{d_h} = \frac{l_{t,0}}{d_h} + 0.11 \cdot f_{core} \cdot \frac{x}{d_h} \tag{3.67}$$

The last process addresses the time delay for droplet acceleration τ_{acc}. Due to the negligible inertia of natural gas, the gas accelerates almost instantaneously to bulk flow velocity $\bar{u}_b$ after being injected. Consequently, there is no additional time delay caused by the injection process. Unlike natural gas, droplet inertia cannot be neglected for liquid fuel injection due to the large density difference between air and fuel [34]. Since the liquid fuel is first being accelerated at the nozzle outlet, there is an additional time delay for the droplets to accelerate to bulk flow velocity. Using the equation of motion for a droplet at constant air velocity, the time scale for droplet acceleration can be estimated. For spherical particles, this equation can be simplified to a balance between inertia force and drag force as follows [48]:

$$\rho_{fuel} \frac{\pi d_{fuel}^3}{6} \frac{du_{fuel}}{dt} = -\frac{\rho_{air}}{2} c_w \frac{\pi d_{fuel}^2}{4} \left(u_{fuel} - u_{air}\right) \left|u_{fuel} - u_{air}\right| \tag{3.68}$$

Here ρ_{air} is the density and u_b the velocity of the air, d_{fuel} represents the Sauter Mean Diameter, ρ_{fuel} the density and u_{fuel} the velocity of the droplets. The drag coefficient c_w can be approximated by an extended Stokes law for droplet Reynolds numbers $Re < 1000$ [68]:

$$c_w = \frac{24}{Re} \left(1 + 0.15 Re^{0.68}\right) \tag{3.69}$$

Re represents the droplet Reynolds number and is defined as follows:

$$Re = \frac{d_{fuel} \left|u_{fuel} - u_{air}\right|}{\nu_{air}} \tag{3.70}$$

Here ν_{air} denotes the kinematic viscosity of the air. Substituting the equation for the drag coefficient (cf. Eq. 3.69) into the equation of motion for

a spherical particle (cf. Eq. 3.68) yields the following first order nonlinear ordinary differential equation for the velocity of the particle:

$$\frac{du_{fuel}}{dt} = -18\frac{\nu_{air}}{d^2}\frac{\rho_{air}}{\rho_{fuel}}\left(1 + 0.15Re^{0.68}\right)\left(u_{fuel} - u_{air}\right) \tag{3.71}$$

Solving Equation 3.71 with the initial velocity of the droplets, a formulation for the velocity profile of a droplet is obtained. The time delay τ_{acc} is then calculated as the time required for the droplets to reach 63% of the gas velocity. This was deduced by Eckstein to be a characteristic time scale for droplet acceleration [34]. Simplifying, it is assumed that the velocity of the air in the burner is constant, resulting in $\mathrm{u_{air}} = \bar{\mathrm{u}}_{\mathrm{b}}$.

4 Experimental Setup

All experimental investigations are carried out in an atmospheric single burner test rig. The individual components of the test rig are presented first. Subsequently, the modular swirl burner is described in detail including all modifications of the burner for the investigation of spray combustion.

4.1 Single Burner Test Rig

A sketch of the atmospheric single burner test rig is shown in Figure 4.1. The main air flow is provided by a 12 bar compressed air supply in the laboratory. The air is filtered and depressurized to 10 bar to compensate for pressure fluctuations in the supply line. Subsequently, the main air flow is preheated in an electric preheater to provide a constant combustor inlet temperature of T_{pre}=573 K. In perfectly premixed natural gas operation (NGp), the fuel is supplied immediately after the preheater. This results in a long mixing section of air and natural gas to avoid equivalence ratio fluctuations. Upstream of the plenum section, the flow is divided into two partial flows, one of which flows directly to the plenum via a bypass and the other is fed to the upstream siren for acoustic excitation. The siren generates a harmonic acoustic signal by means of a disc with double sine shaped orifices. In order to control the rotational speed, the siren shaft is mounted to a 1.1 kW three-phase motor, which provides a nominal torque of 3.7 Nm. Excitation frequencies of up to f = 800 Hz can be achieved, whereby the excitation amplitudes are depending on the supplied air mass flow. A detailed description of the siren is given by Eckstein [32]. A second siren is mounted perpendicular to the flow di-

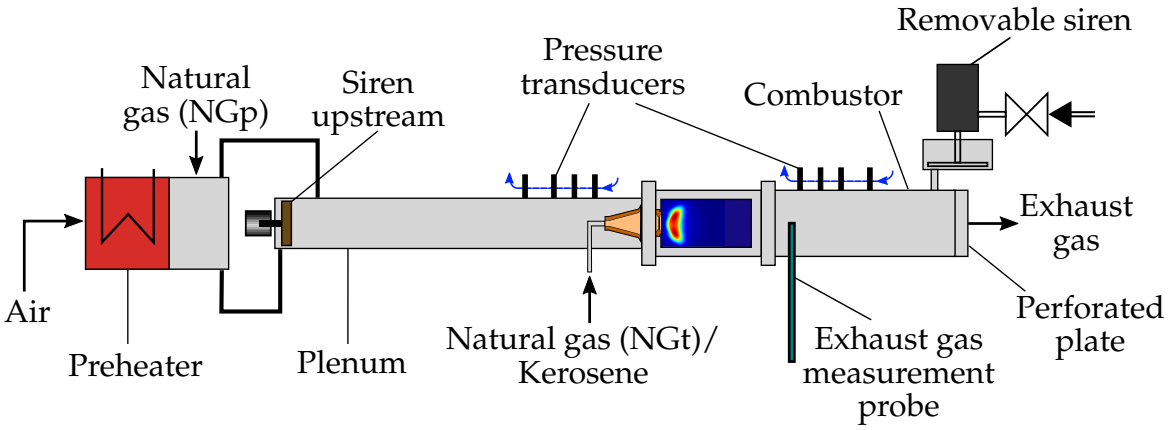

Figure 4.1: Sketch of the Single Burner Test Rig. Adapted from Stadlmair [123].

rection downstream of the combustor, which is fed with compressed air passing through a fast-switching modulator valve.

The plenum is constructed of several insulated cylindrical pipe segments with an inner diameter of 124 mm and a total length of 1725 mm. The combustion chamber is square in cross-section with side length of 150 mm and an overall length of 730 mm. It features a quartz glass window for optical combustion diagnostics. The combustion chamber is cooled with an impingement air cooling. A perforated plate is installed at the combustion chamber outlet. The plate is used to achieve low acoustic reflection during acoustically excited measurements.

The test rig is equipped with a total of eight water-cooled piezoelectric pressure transducers of the type PCB 106B. Four of them are installed in the plenum and four in the combustion chamber. This configuration allows to reconstruct the fluctuating acoustic pressure and velocity fields upstream and downstream of the burner [101]. In addition, an exhaust gas measurement probe is installed 540 mm downstream of the burner outlet. The measurement probe used for exhaust gas analysis is water-cooled to provide a constant exhaust gas temperature of T_{eg}=353 K. This quenches the reactions continuing in the exhaust gas and also avoids humidity condensing in the gas. Since NO_2 is partially soluble in water, con-

densation in the exhaust gas has to be prevented, otherwise NO_x measurement would be incorrect [86]. The sampled exhaust gas is analyzed in an ECOphysics CLD700ELht chemiluminescence detector.

4.2 Dual Fuel Swirl Burner

A downscaled version of the A^2EV burner, developed by Sangl [113] and Mayer [85], is used in this study. The burner is optimized for a wide operating range in terms of low NO_x emissions and high flame flashback safety. A schematic of the burner is provided in Figure 4.2. The burner is divided into two parts, a diverging swirler followed by a converging mixing tube. The swirler has an head air inlet at its tip and four tangential slots. The mixing tube has a length of $l_{MT} = 1.875\ d_b$, where d_b represents the burner outlet diameter. In technically premixed operation, natural gas is fed directly into the swirler (NGt). The fuel is injected at each of the four trailing edges of the slots through ten equally spaced holes.

The sudden change in cross section between burner outlet and combustion chamber causes vortex breakdown. Consequently, shear layers of the inner and outer recirculation zones are formed as well as a stagnation of the flow at the burner centerline. As a result, the flame stabilizes within the core flow at the top of the recirculation zone and propagates in the inner shear layer following local flow direction. In the outer shear layer, no reaction occurs due to high strain rates and heat losses to the combustion chamber walls [62].

In the present work, the burner is extended by a central twin-fluid nozzle on the burner axis to enable the injection of liquid fuel. Figure 4.2 already shows the burner with the nozzle installed. The nozzle is inserted through the head air inlet of the burner and thus blocks the free area of the head air. As a result, the mass flow through the tangential slots is increased, leading to higher tangential velocities and thus to an increased swirl number. However, blocking the head air inlet also leads to

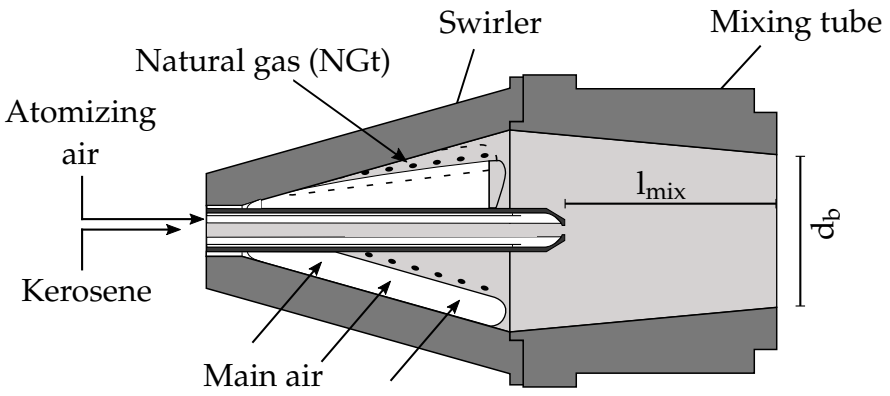

Figure 4.2: Sketch of the A^{2}EV dual fuel burner.

a decrease in axial velocity, which affects the position of the recirculation zone [8]. The nozzle is fed with kerosene and air. A jet of high velocity atomizing air is brought into contact with a liquid flow. As a result, this nozzle can produce fine droplets at low liquid velocities [7]. The atomizing air is additionally swirled in the nozzle to improve atomization. The swirl direction is equal to that of the main air mass flow. The ratio of atomizing to main air flow is kept constant and set to $\dot{m}_{at}/\dot{m}_{air}$=3.5% for all investigations involving kerosene. The mixing length, representing the distance from the tip of the nozzle to the burner outlet, measures l_{mix} = 2.2 d_b. All experiments involving natural gas are carried out without the twin-fluid nozzle installed.

A blue oil flame is observed for kerosene combustion indicating the flame to be premixed. The premixed characteristic of the kerosene flame can be verified indirectly by examining the NO_x emissions. Based on NO_x emissions, the degree of premixing of a combustion system can be evaluated. As the degree of premixing decreases, inhomogeneities of the mixture composition in the reaction zone increase. Local hotspots occur in areas of the flame where a richer mixture than the global equivalence ratio is present. This leads to an increase in NO_x emissions, as these are dependent on the local combustion temperature (cf. Fig. 1.1) [11,75].

Figure 4.3 shows NO_x emissions for different mass flow rates for perfectly

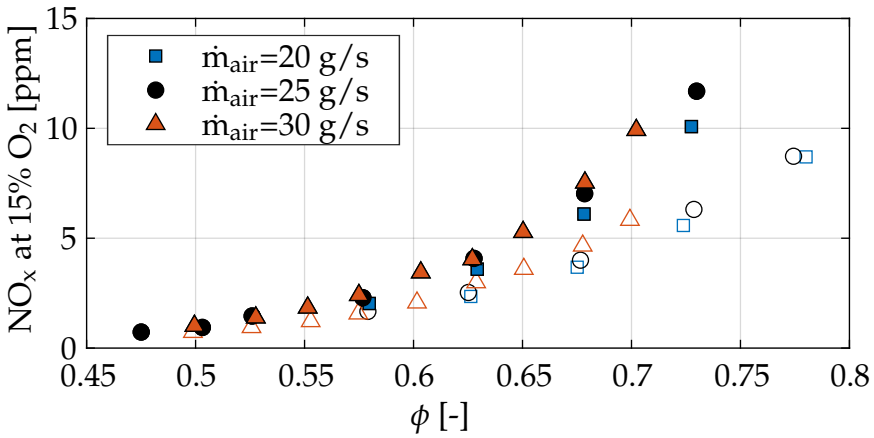

Figure 4.3: NO_x emissions for different mass flow rates. Unfilled symbols denote perfectly premixed natural gas, filled ones kerosene combustion [58].

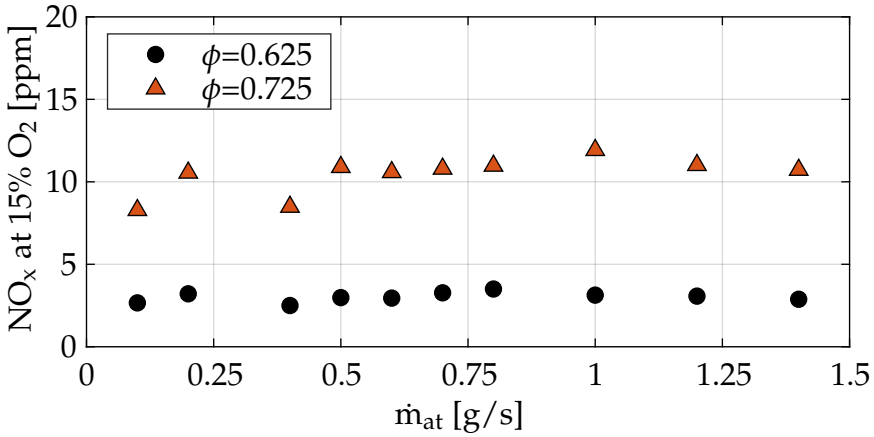

Figure 4.4: Influence of the atomizing air mass flow $\dot{m}_{air}$ on NO_x emissions for kerosene combustion at a constant air mass flow rate of $\dot{m}_{air}$=25 g/s [58].

premixed natural gas combustion as well as kerosene combustion. An exponential increase in NO_x emissions with increasing equivalence ratio is observed for both fuels. In addition, the NO_x emissions are independent of the total mass flow rate. Here, the NO_x emissions for perfectly premixed natural gas combustion are considered as benchmark, since premixed combustion can be assumed in advance. NO_x emissions for kerosene combustion are slightly higher compared to natural gas, which

could be due in part to the different chemical composition [72]. However, NO_x emissions from kerosene combustion are always close to those from natural gas combustion, indicating a well premixed system.

Figure 4.4 shows the influence of the atomizing air mass flow $\dot{m}_{air}$ on NO_x emissions for kerosene combustion. It can be seen that NO_x emissions are independent of the atomizing air mass flow rate. The atomization quality of the injector is primarily affected by the air-liquid ratio and thus by the atomizing air mass flow rate. This indicates that the mixing section is sufficiently long to ensure complete vaporization of the fuel and homogeneous mixing of vaporized fuel and air. Thus, it can be concluded that a premixed kerosene flame is achieved over the entire operating range.

5 Acoustic and Optical Measurement Techniques

This chapter introduces the acoustic and optical measurement techniques for investigation of flame dynamics. First, the method for determining acoustic scattering matrices based on dynamic pressure measurements is outlined. The scattering matrices are required to determine the velocity fluctuations at burner outlet. Subsequently, the optical measurement techniques for monitoring flame chemiluminescence are presented. A description of the measurement technique for spectrally resolved chemiluminescence using a spectrometer is provided first. Here, the global characteristics of chemiluminescence spectra and their correlation to the equivalence ratio are in the focus of interest. The bandpass filtered chemiluminescence technique utilizing an image intensified high speed camera is presented afterwards. This allows high temporal and spatial resolution for investigating unsteady combustion phenomena.

5.1 Determination of Scattering Matrices

The acoustic characteristics of the burner are considered by acoustic scattering matrices. The scattering matrices allow the reconstruction of the velocity fluctuations at the burner outlet, taking into account the acoustic losses of the burner. Figure 5.1 shows a schematic of the method for determining the acoustic scattering matrices by dynamic pressure measurements.

The objective of the procedure is the determination of the scattering matrix SM according to Equation 3.41. In order to determine the four, fre-

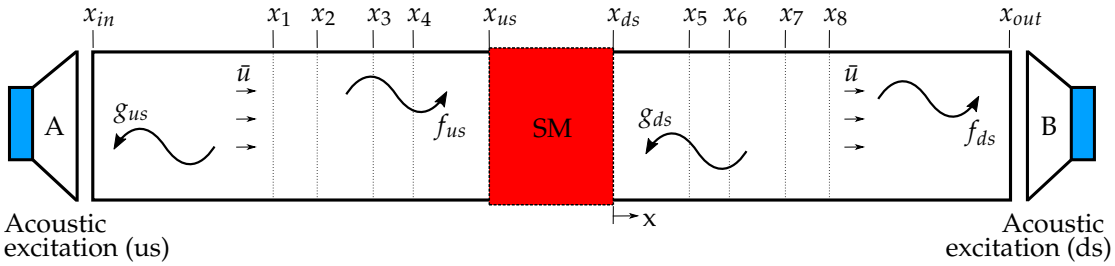

Figure 5.1: Experimental determination of scattering matrices. Adapted from Stadlmair [123].

quency dependent matrix elements of the scattering matrix, two linearly independent excitation states are required. For this purpose, one acoustic source is located upstream and one downstream of the element to be investigated, also referred to as the two-source method [89]. Dynamic pressure is measured at four positions upstream (x_1 - x_4) and downstream (x_5 - x_8) of the element. According to Equation 3.25, the Riemann invariants f and g can then be calculated based on dynamic pressure measurements. This method is also known as multi-microphone method (MMM) [36, 101]. The MMM is an extended technique of the two-microphone method (TMM), which significantly improves the stability of the measurement method [2, 3]. The TMM utilizes only two microphones each for reconstructing the acoustic waves, which can lead to the occurrence of singularities if the distance between the two measurement points is exactly half a wavelength [37]. The resulting system of equations for calculating the Riemann invariants is solved by a least squares method, reading [123]:

$$\begin{bmatrix} f^A_{us/ds}(\omega) & f^B_{us/ds}(\omega) \\ g^A_{us/ds}(\omega) & g^B_{us/ds}(\omega) \end{bmatrix} = \mathbf{H}^{\dagger}_{us/ds}\mathbf{p}'_{us/ds} \tag{5.1}$$

Here, † represents the pseudo-inverse of the matrix H, which is defined as follows:

$$\mathbf{H}^{\dagger} = \left(\mathbf{H}^{\top} \cdot \mathbf{H}\right)^{-1} \cdot \mathbf{H}^{\top} \tag{5.2}$$

The matrix H comprises the respective wavenumbers and locations of dynamic pressure measurement in the upstream and downstream duct,

yielding:

$$\mathbf{H}_{us} = \begin{bmatrix} \exp\left(-ik_{us}^{+}x_1\right) & \exp\left(ik_{us}^{-}x_1\right) \\ \vdots & \vdots \\ \exp\left(-ik_{us}^{+}x_4\right) & \exp\left(ik_{us}^{-}x_4\right) \end{bmatrix} \tag{5.3}$$

$$\mathbf{H}_{ds} = \begin{bmatrix} \exp\left(-ik_{ds}^{+}x_5\right) & \exp\left(ik_{ds}^{-}x_5\right) \\ \vdots & \vdots \\ \exp\left(-ik_{ds}^{+}x_8\right) & \exp\left(ik_{ds}^{-}x_8\right) \end{bmatrix} \tag{5.4}$$

Here, p′ denotes the Fourier transform of the pressure measurement at the respective forcing frequency, with $\mathbf{p'_{us}}$ containing the acoustic pressure signals in the upstream duct, $\mathbf{p'_{ds}}$ those in the downstream duct:

$$\mathbf{p}'_{us} = \begin{bmatrix} p'^{A}\left(x_1,\omega\right) & p'^{B}\left(x_1,\omega\right) \\ \vdots & \vdots \\ p'^{A}\left(x_4,\omega\right) & p'^{B}\left(x_4,\omega\right) \end{bmatrix} \tag{5.5}$$

$$\mathbf{p}'_{ds} = \begin{bmatrix} p'^{A}\left(x_5,\omega\right) & p'^{B}\left(x_5,\omega\right) \\ \vdots & \vdots \\ p'^{A}\left(x_8,\omega\right) & p'^{B}\left(x_8,\omega\right) \end{bmatrix} \tag{5.6}$$

Thus, the following system of linear equations is obtained to determine the coefficients of the scattering matrix [123]:

$$\underbrace{\begin{bmatrix} T^{+} & R^{-} \\ R^{+} & T^{-} \end{bmatrix}}_{\mathbf{SM}} = \begin{bmatrix} f_{\mathrm{ds}}^{A} & f_{\mathrm{ds}}^{B} \\ g_{us}^{A} & g_{us}^{B} \end{bmatrix} \begin{bmatrix} f_{us}^{A} & f_{us}^{B} \\ g_{\mathrm{ds}}^{A} & g_{\mathrm{ds}}^{B} \end{bmatrix}^{-1} \tag{5.7}$$

5.2 Chemiluminescence Spectroscopy

Figure 5.2 shows a sketch of the spectrally resolved chemiluminescence technique. A *SpectraPro 275* imaging spectrometer from *Acton Research Cooperation* is used for the investigations. It is a Czerny-Turner monochromator of 275 mm focal length with an aperture ratio of 1:3.8. A diffraction grating with 150 grooves per millimeter is chosen, allowing the observation of about 300 nm of the flame spectrum. The flame chemiluminescence is focused on the inlet slit of the spectrometer using a UV lens with a focal length of 45 mm and a maximum aperture ratio of 1:1.8. The slit width is adjusted to 10 µm. A *LaVision StreakStar* image intensified camera system is attached to the spectrometer for recording the spectra. For each operation point 20 spectrally resolved images are taken with a resolution of 384x286 pixels. An exposure time of 5 ms is set to provide a good signal to noise ratio. The measured spectrum is recorded by the camera as an image.

An additional calibration measurement is required to determine the exact wavelengths corresponding to each pixel. Therefore, the spectrum of a mercury arc lamp is recorded using the imaging spectrometer. The mea-

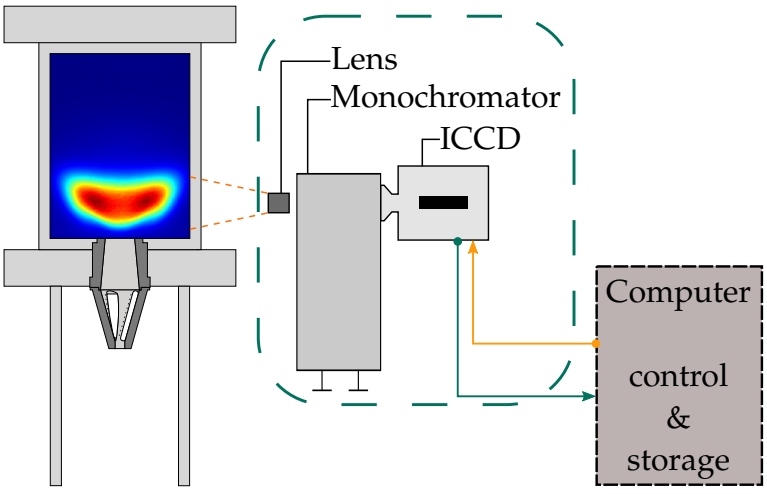

Figure 5.2: Sketch of the spectrally resolved measurement technique.

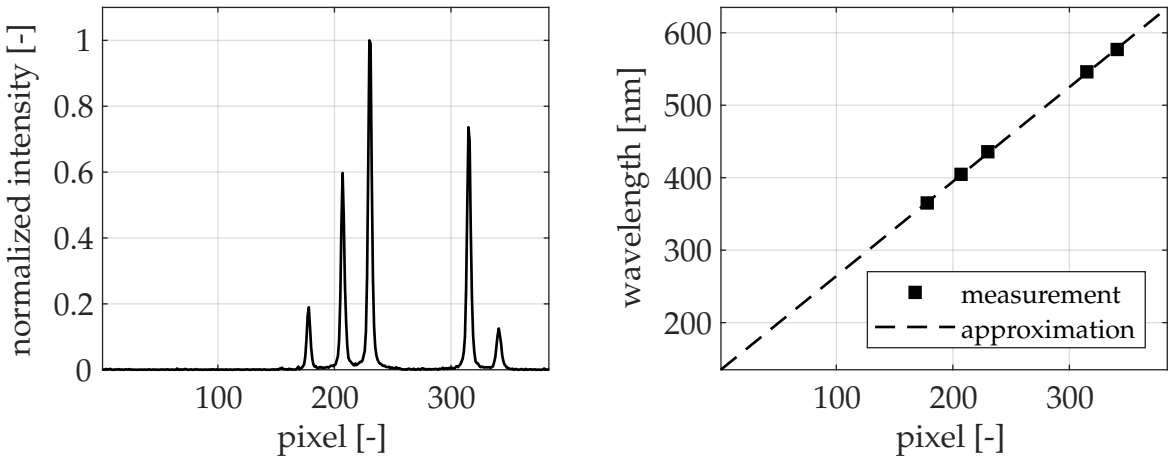

Figure 5.3: Measured spectrum of a mercury arc lamp for wavelength calibration (left) and conversion rule between pixel scale and nm scale of the measurement setup (right).

sured spectrum of the mercury arc lamp is shown in the left plot of Figure 5.3. The normalized intensity is plotted over the individual pixels of the image. Five distinct spectral lines are clearly visible in the measured spectrum. The characteristic wavelengths of the individual spectral lines of the mercury arc lamp are known from Reader et al. [108]. Thus, the pixel numbers of the identified spectral lines can be converted to the corresponding wavelengths. The right plot of Figure 5.3 presents the correlation between the nm scale and the pixel scale. The measured data points can be approximated by a first degree polynomial.

In addition, the entire measurement system has an unknown wavelength-dependent sensitivity. This sensitivity can be determined by a second calibration. The spectrum of a calibrated halogen lamp is recorded and compared to the reference spectrum of this lamp. The reference spectrum is provided by the manufacturer. Thus, a wavelength-dependent calibration factor can be determined, which is subsequently applied to all measured spectra. Figure 5.4 shows the normalized intensities of the reference spectrum and the measured spectrum of the halogen lamp and the calculated calibration factor.

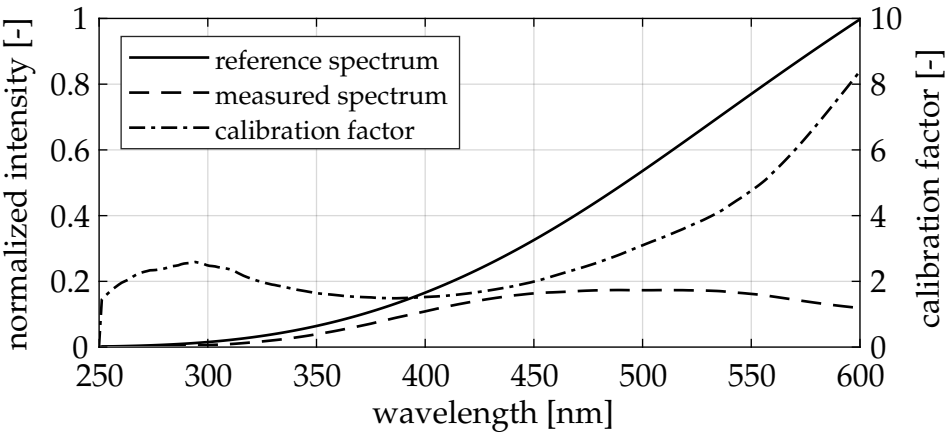

Figure 5.4: Reference spectrum and measured spectrum of the halogen lamp together with the wavelength-dependent calibration factor.

Spectrally resolved measurements are conducted for different thermal powers in the range of 40 to 60 kW. The equivalence ratio is varied between ϕ=0.525 and ϕ=0.8 at constant fuel flow rates. During post-processing, the images are averaged, and the respective spectra are filtered with a Savitzky-Golay filter. The Savitzky-Golay filter approximates successively 2m+1 interpolation points with a polynomial of degree p (p$\leq$2m). The least squares method is applied to obtain a smoothed value for the center of these interpolation points. The n-th derivative (0$\leq$n$\leq$p) at the center of the respective interpolation points is obtained by differentiating the calculated polynomial. Finally, this method of least squares can be repeated several times and thus for each data point a smoothed value can be calculated [83]. For all spectra the Savitzky-Golay filter with fifth degree polynomials is used. For the approximation of these polynomials, 19 interpolation points are used respectively.

A typical chemiluminescence spectrum of a lean premixed kerosene flame under atmospheric conditions is shown in Figure 5.5. The OH*, CH* and C_2* chemiluminescence is superimposed by a broadband background radiation. This background radiation is mainly attributed to CO_2*. To determine the true intensities of OH* and CH*, the corresponding background radiation has to be subtracted from the respective ar-

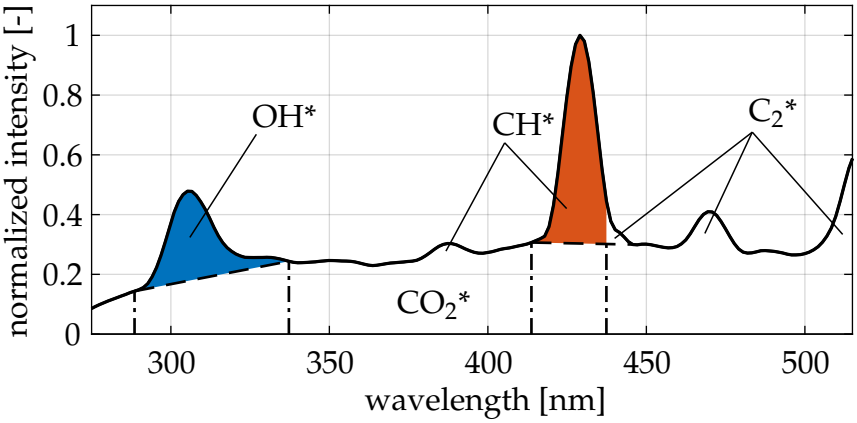

Figure 5.5: Typical chemiluminescence spectrum of a lean premixed kerosene flame under atmospheric conditions.

eas in the relevant wavelength ranges. For this purpose, the CO_2* background radiation is linearly interpolated within the individual radical ranges (indicated by the dashed lines). Accordingly, only the area between the linear interpolation and the peak of each radical emission represents the true chemiluminescence of the respective radical. These areas are highlighted in Figure 5.5. The intensity of the OH* radical is shown in blue and the intensity of the CH* radical in red. The corresponding wavelength ranges are indicated by the dash-dotted lines.

5.3 Bandpass Filtered Chemiluminescence

The bandpass filtered measurement system consists of a *Photron FastCam SA-X2* high-speed camera equipped with a *Hamamatsu C10880* image intensifier and a silica glass camera lens. The lens has a focal length of 45 mm and a maximum aperture of 1:1.8. An image doubler from *LaVision* is mounted in front of the camera lens. The image doubler provides a projection of an image pair onto one camera chip. Two different bandpass filters are mounted simultaneously on the image doubler. The following filters are used in this study:

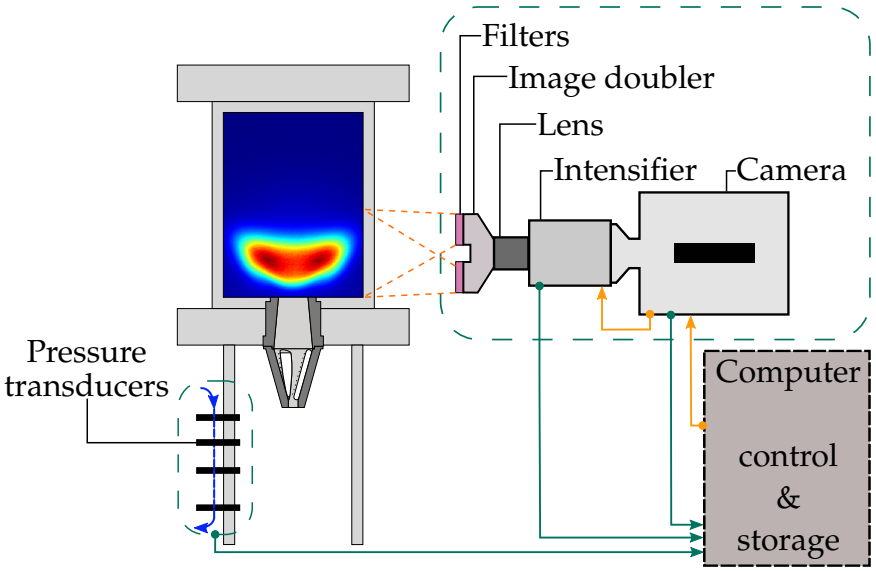

Figure 5.6: Sketch of the bandpass filtered measurement technique.

- CH*-filter with a center wavelength (CWL) of 431.39 nm, a peak transmission of 48.63% and a full width at half maximum (FWHM) of 10.6 nm
- CO_2*-filter with a CWL of 456.42 nm, a peak transmission of 68.18% and a FWHM of 2.4 nm

Hence, the image doubler enables the CH* and CO_2* chemiluminescence signal of the flame to be recorded onto one camera chip. A sketch of the optical measurement system for bandpass filtered chemiluminescence investigations is shown in Figure 5.6. The data acquisition system comprises a measurement computer equipped with a *National Instruments PCI-4472* measurement card. In addition to the high-speed images, time series of a total of six signals are recorded synchronously. The pressure curves of the four pressure sensors in the plenum as well as the exposure times of the camera and the image intensifier are recorded. The applied sampling frequency is f_s=65536 Hz. Images of the entire flame front can be taken through the quartz glass optical access. The focus of the lens is set to the center plane of the combustion chamber. The image intensifier is triggered by the camera. An exposure time of 200 µs is set for the inten-

sifier. For stationary measurements, a frame rate of 125 frames per second is selected for the camera and 1000 images are acquired. For acoustically excited measurements, 6000 images are recorded for each excitation frequency with a frame rate of 2000 frames per second.

5.3.1 Processing of Stationary Image Data

Figure 5.7 shows a sketch of the processing of the stationary flame images. The image pair is first divided into two separate images for CH* and CO_2*. After averaging the CH* and CO_2* images individually, an image distortion correction procedure is applied. Stereoscopic imaging using the image doubler results in perspective distortion of the image pair. A calibration measurement is required to determine the distortion. Therefore, a reference target is placed in the center plane of the combustion chamber and recorded using the bandpass filtered system. A transformation algorithm is determined for both halves of the image and subsequently applied to all flame images. The absorption of chemiluminescence in the flame is not accounted for, as this has been found to be negligible in atmospheric flames [52]. The distortion corrected images represent the integrated line-of-sight intensity distribution. Assuming a rotationally symmetric flame, the intensity distribution in the center plane can be reconstructed from the time-averaged measurements. Therefore, an Abel inversion using the BASEX method is applied [29, 47]. The local CH*/CO_2* distribution is then calculated for each pixel where the intensity of both CH* and CO_2* is at least 50% of the respective maximum chemiluminescence intensity. The global CH*/CO_2* ratio is calculated by integrating the local ratio distribution over the flame area.

The flame is characterized based on the CH* chemiluminescence distribution in the center plane. The flame length is determined as the axial distance between the burner outlet and the flame center of gravity x_{cg}.

The center of gravity is calculated as follows:

$$x_{cg} = \frac{\sum_{i=1}^{x_{max}} \left(x_i \sum_{j=1}^{r_{max}} I_{ij} \right)}{\sum_{i=1}^{x_{max}} \sum_{j=1}^{r_{max}} I_{ij}} \tag{5.8}$$

Thus, the chemiluminescence intensity is first integrated in radial direction and then weighted by the corresponding axial position x_i.

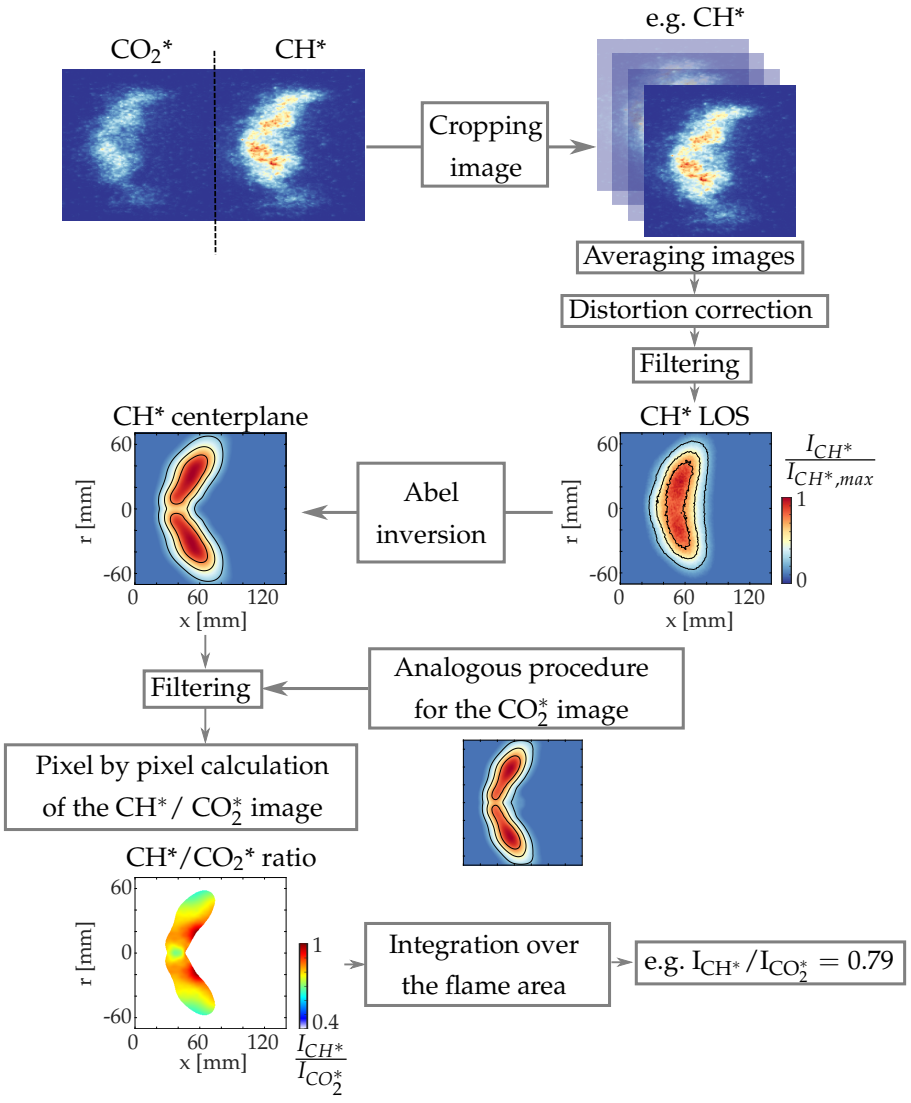

Figure 5.7: Processing of flame images for evaluating bandpass filtered chemiluminescence.

5.3.2 Determination of Equivalence Ratio Oscillations

For the reconstruction of flame dynamics during acoustic excitation, the synchronization of pressure and image data is performed. The procedure for correlating image and pressure data is shown schematically in Figure 5.8. First, the points in time at which an image was captured are determined. The signals from the high-speed camera and the image intensifier are utilized for this purpose. The image intensifier signal (II) indicates the time of image acquisition along with the corresponding exposure time, while the recording signal from the camera provides time stamps indicating the beginning and termination of the entire acquisition process. Based on the pressure data, the phase of the oscillation is identified. The phase of the oscillation is calculated using the Hilbert transform. The Hilbert transform has emerged as a fundamental method in the analysis of thermoacoustic systems [43, 92]. The individual images are then sorted according to the phase of the pressure oscillation at the sensor in the plenum closest to the burner inlet. The phase is divided into 12 subintervals of equal size and all images are assigned to subintervals according to their phase. Average flame images for each phase interval are then

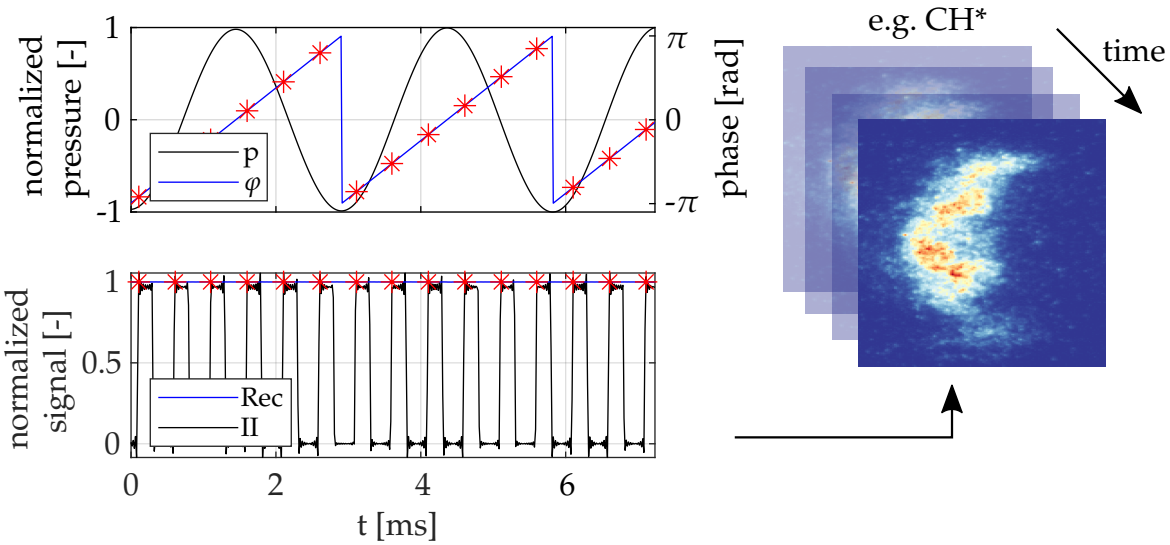

Figure 5.8: Procedure for correlating image and pressure data. Red stars indicate the point in time at which an image was acquired.

calculated separately. Each of these 12 phase-averaged flame images is thus calculated using approximately 500 single images. The centerplane distribution of CH* and CO_2* intensity of the phase-averaged images is determined by Abel inversion using the BASEX method [29, 47]. Subsequently, the ratio of CH*/CO_2* is determined pixel by pixel for each phase-averaged image. For ensuring a sufficient signal-to-noise ratio, the CH*/CO_2* ratio is only evaluated in the area where the chemiluminescence intensity of the individual species involved exceeds 50% of the respective maximum intensity. Applying the calibration chart (which will be presented in Figure 6.5) and integrating the local distribution over the flame area yields the phase-averaged global equivalence ratio $\langle\phi\rangle$.

For an unsteady flow, the equivalence ratio can be expressed by a time-averaged, deterministic and random component as follows:

$$\phi = \bar{\phi} + \phi' + \tilde{\phi} \tag{5.9}$$

As this study utilizes only phase-averaged quantities using a sufficiently large number of images for averaging, the random component is likely to become negligible. Thus, the deterministic component is determined by the following equation:

$$\phi' = \langle\phi\rangle - \bar{\phi} \tag{5.10}$$

ϕ' denotes the fluctuating component of the equivalence ratio, $\langle\phi\rangle$ the phase-averaged one and $\bar{\phi}$ the time-averaged equivalence ratio. A discrete Fourier transform is applied to each excitation frequency to derive the complex-valued representation of the oscillating component of the equivalence ratio. Finally, the equivalence ratio transfer function is derived (cf. Eq. 3.49) relating equivalence ratio fluctuations in the flame to velocity oscillations at the burner outlet.

To facilitate comparison of the transfer functions for different operating points, the dimensionless Strouhal number is utilized, which is defined as follows [111]:

$$Sr = \frac{f \cdot \Delta x}{\bar{u}_b} \tag{5.11}$$

The Strouhal number represents the ratio of the convective distance to the convective wavelength. Here, f denotes the excitation frequency, Δx the distance between fuel injection and flame and $\bar{u}_b$ the axial velocity at the burner outlet.

6 Equivalence Ratio From Flame Chemiluminescence

The results of the stationary studies are shown and discussed in the following sections. Firstly, the results of the spectrally resolved investigations are presented. As already mentioned in Section 5.2 the chemiluminescence from OH* and CH* is superimposed by a broadband background radiation, which must be taken into account in the evaluation procedure. The subtraction of the broadband background radiation from the respective chemiluminescence intensities is referred to as background correction in the following. The focus of the spectrally resolved measurements is on the influence of the background correction on the correlation between different intensity ratios of the respective species and the equivalence ratio. Only the global spectral characteristics of the different chemiluminescence species are considered here. Secondly, the results of the bandpass-filtered chemiluminescence measurements are discussed. Here, the applicability of the measurement technique for determining equivalence ratio fluctuations during acoustic excitation is examined in more detail. All results presented in this chapter involving natural gas represent perfectly premixed natural gas combustion (NGp).

6.1 Chemiluminescence Spectroscopy

The objective of this study is to identify correlations between intensity ratios of chemiluminescence species and the equivalence ratio for lean, premixed natural gas and kerosene combustion. For natural gas, C_2* chemiluminescence is only observable for rich conditions and disap-

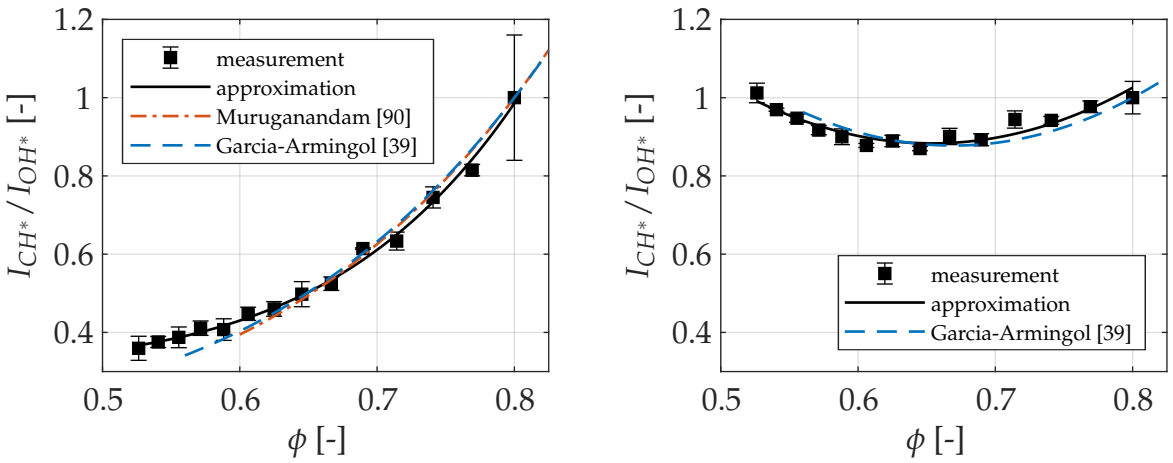

Figure 6.1: The dependence of the CH*/OH* chemiluminescence ratio on the equivalence ratio ϕ for background corrected intensities (left) and total intensities (right) for natural gas combustion. Reference results from Muruganandam and Garcia-Armingol are presented additionally. Data are normalized with their value at ϕ=0.8. Error bars indicate the standard deviation.

pears for lean conditions [39]. In contrast, C_2* chemiluminescence is detectable in kerosene flames even for lean conditions. This study only addresses species present for both fuels and thus focuses on OH*, CH*, and CO_2* chemiluminescence. The background radiation, which is mainly attributed to CO_2*, can be evaluated in a specific range of the spectrum, where no characteristic peaks of other radicals are present. For the investigations presented here, the range from 455 to 457 nm was chosen. In the following, this evaluated intensity will be referred to as CO_2* chemiluminescence. First, the intensity ratios for perfectly premixed natural gas combustion are examined in detail.

Figure 6.1 shows the relation of the CH*/OH* ratio and the equivalence ratio for the combustion of natural gas under atmospheric conditions. The intensities of CH* and OH* are background corrected in the left plot and uncorrected in the right one. In addition, reference results from Muruganandam [90] and Garcia-Armingol [39] are presented. For comparability, all data are normalized with their value at ϕ=0.8. It can be seen that

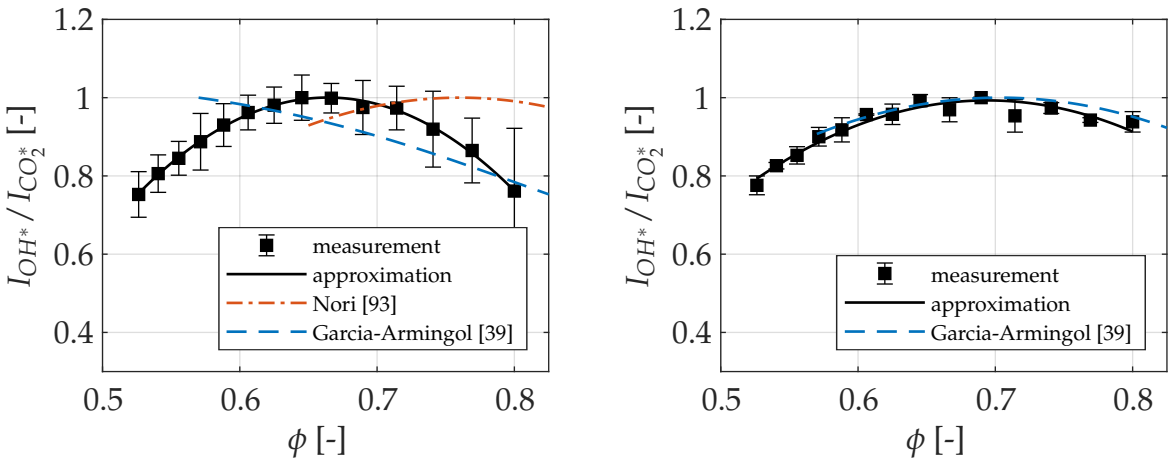

Figure 6.2: The dependence of the OH*/CO_2* chemiluminescence ratio on the equivalence ratio ϕ for background corrected intensities (left) and total intensities (right) for natural gas combustion. Reference results from Nori and Garcia-Armingol are presented additionally. Data are normalized with their maximum value. Error bars indicate the standard deviation.

the CH*/OH* ratio with background correction exhibits a monotonic dependence on the equivalence ratio. The ratio increases with increasing equivalence ratio. The measured data points can be approximated accurately by a power law. The results presented are in good agreement with the findings of Muruganandam and Garcia-Armingol. Thus, it can be assumed that the measurement setup used has been calibrated and adjusted appropriately and therefore provides reliable results. In contrast, the CH*/OH* ratio without background correction shows no monotonic dependence on the equivalence ratio within the investigated range. This observation is also consistent with the findings of Garcia-Armingol [39]. The ratio shows a parabolic trend with a minimum at about ϕ=0.65. Thus, the CH*/OH* ratio can only be utilized as a measure for the equivalence ratio when it is corrected for background radiation.

Figure 6.2 depicts the relationship between the OH*/CO_2* ratio and the equivalence ratio for the combustion of natural gas. It can be seen that the OH*/CO_2* ratios show no monotonic dependence on the equiva-

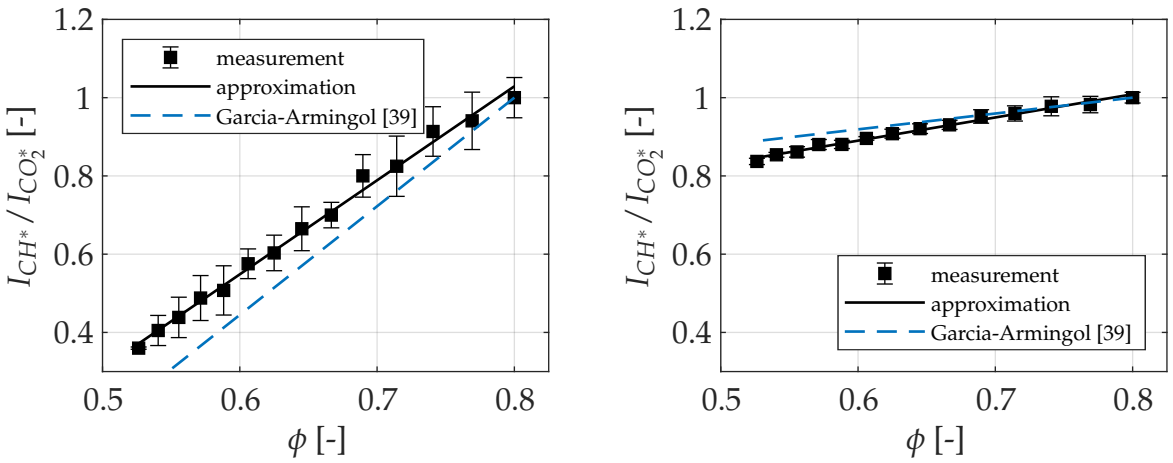

Figure 6.3: The dependence of the CH*/CO_2* chemiluminescence ratio on the equivalence ratio ϕ for background corrected intensities (left) and total intensities (right) for natural gas combustion. Reference results from Garcia-Armingol are presented additionally. Data are normalized with their value at ϕ=0.8. Error bars indicate the standard deviation.

lence ratio for either the background corrected or uncorrected intensities. The experimental data are approximated with a second order polynomial. The maximum for both ratios is between ϕ=0.65 and ϕ=0.7 and decreases for increasing as well as decreasing equivalence ratios. Reference data from Nori [93] indicate a similar trend for the ratio with background correction, but here the maximum ratio was observed at ϕ=0.75. For the ratio with background correction, Garcia-Armingol [39] reported a monotonic trend in the investigated range. He observed an increase in the OH*/CO_2* ratio with decreasing equivalence ratio. However, the ratio without background correction agrees almost perfectly with the results from Garcia-Armingol.

Lastly, the relationship between the CH*/CO_2* ratio and the equivalence ratio for the combustion of natural gas is presented in Figure 6.3. A clear correlation between the CH*/CO_2* ratio and the equivalence ratio is identified in both the uncorrected and the background corrected results. Both data sets are approximated by a first order polynomial. The

ratio increases monotonically with increasing equivalence ratio. It can be seen that the background corrected CH*/CO_2* ratio shows a substantially higher sensitivity to the equivalence ratio than the ratio without background correction. While the ratio with background correction decreases to a value below 40% of its maximum value, the ratio only decreases by about 20% without background correction in the investigated range. These results are in line with studies from Garcia-Armingol indicating that the background correction increases the sensitivity of the CH*/CO_2* ratio to the equivalence ratio [39].

Figure 6.4 depicts the same three chemiluminescence ratios for the combustion of kerosene that have already been discussed for natural gas combustion. Analogously, the chemiluminescence intensities of CH* and OH* are background corrected in the left plots and uncorrected in the right plots. All data are normalized with their maximum value. The CH*/OH* and CH*/CO_2* ratios exhibit a monotonic relationship to the equivalence ratio in both the background corrected and uncorrected data. An increase in the ratio with increasing equivalence ratio can be observed, respectively. The CH*/OH* ratio with background correction is approximated by a first order polynomial, while the ratio without background correction seems to follow a power law. The CH*/CO_2* ratio shows a linear trend both with and without background correction. Similar as observed for natural gas combustion, the CH*/CO_2* ratio with background correction shows higher sensitivity to the equivalence ratio than the ratio without background correction. While the CH*/CO_2* ratio without background correction still exceeds 70% of the maximum value at an equivalence ratio of ϕ=0.525, the ratio drops below 50% of the maximum value in the case with background correction. In contrast, the OH*/CO_2* ratio does not reveal a monotonic relationship to equivalence ratio neither for the ratio with nor without background correction. In the case with background correction, the ratio takes its maximum value at an equivalence ratio of ϕ=0.625 and decreases again for both increasing and decreasing equivalence ratios. In addition, the high standard deviation for equivalence ratios ϕ <0.65 is noticeable. A similar trend to natural gas com-

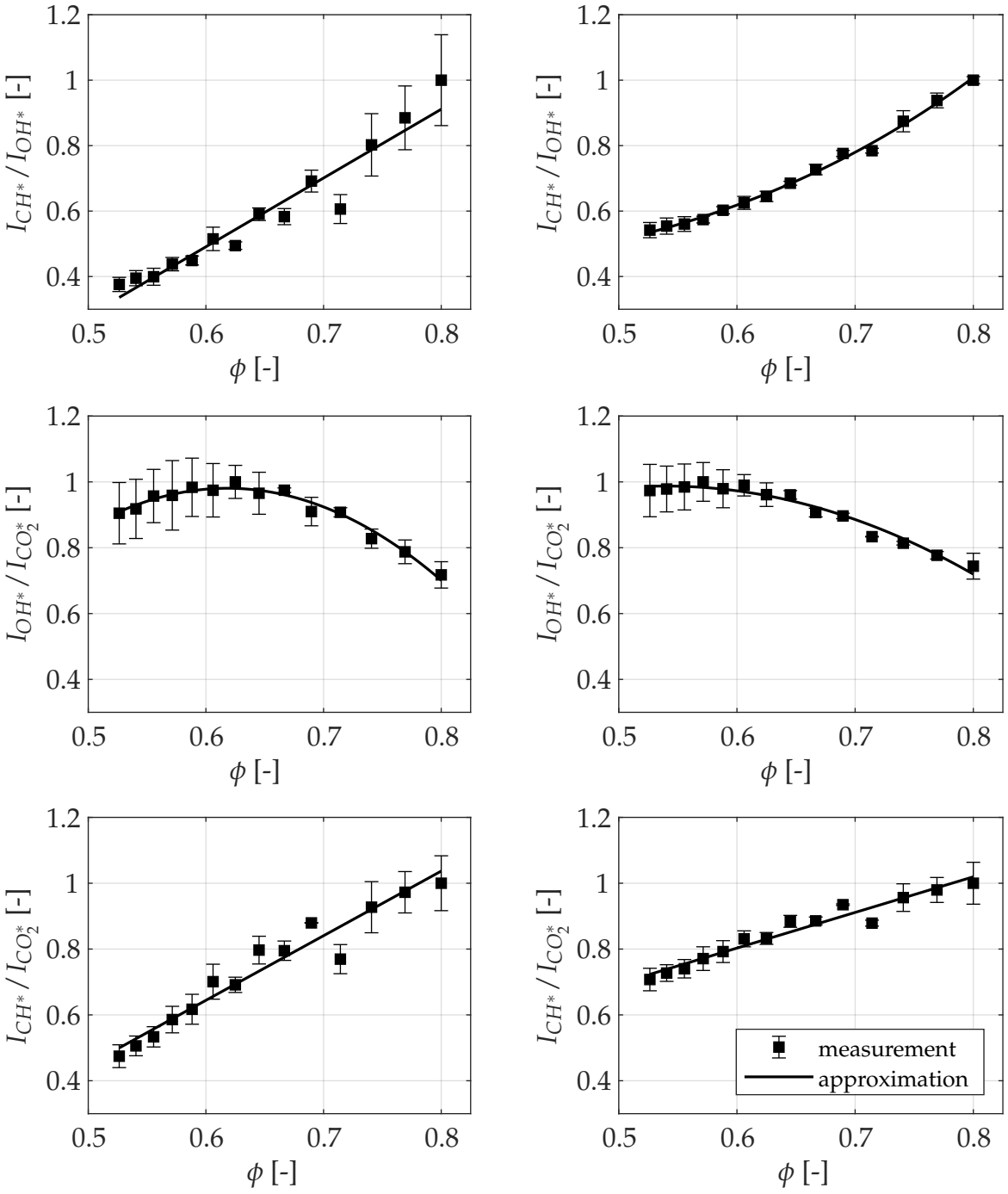

Figure 6.4: The dependence of different chemiluminescence ratios on the equivalence ratio ϕ for background corrected intensities (left) and total intensities (right) for kerosene combustion. Data are normalized with their maximum value. Error bars indicate the standard deviation.

bustion is observed, where both ratios can be approximated by a second order polynomial.

Finally, it can be summarized that the CH*/CO_2* ratio is the only ratio without background correction showing a monotonic relationship to the equivalence ratio for natural gas and kerosene combustion. Therefore, this ratio was chosen for the following bandpass-filtered chemiluminescence measurements.

6.2 Bandpass Filtered Chemiluminescence

As pointed out in Section 6.1, the CH*/CO_2* ratio will be utilized as measure for the equivalence ratio for all further studies. In stationary operation, the relationship between the CH*/CO_2* ratio and the equivalence ratio is first established to account for the transmission behavior of the measurement system and sensitivity of the camera chip. Figure 6.5 presents the relationship between the global CH*/CO_2* ratio and the equivalence ratio for natural gas and kerosene combustion. A clear correlation between the CH*/CO_2* chemiluminescence ratio and the equivalence ratio is also observed for the bandpass filtered chemiluminescence measurements. A linear increase in the ratio with increasing equivalence ratio can be seen for both natural gas and kerosene combustion. In addition, it becomes apparent that the total mass flow rate has only a minor influence on this ratio. For constant equivalence ratios, an increase in the CH*/CO_2* ratio with increasing mass flow rate is noticeable. Since previous studies have reported that the ratio is independent of the total mass flow rate, this aspect is examined in more detail in the following [14, 55].

Figure 6.6 shows the CH* flame images along with the corresponding spatial distribution of the CH*/CO_2* ratio for different equivalence ratios for natural gas combustion. The upper half of Figure 6.6 illustrates the CH* flame image and additionally the 50% isoline of CO_2* chemiluminescence intensity is shown in the dashed line. All images are normal-

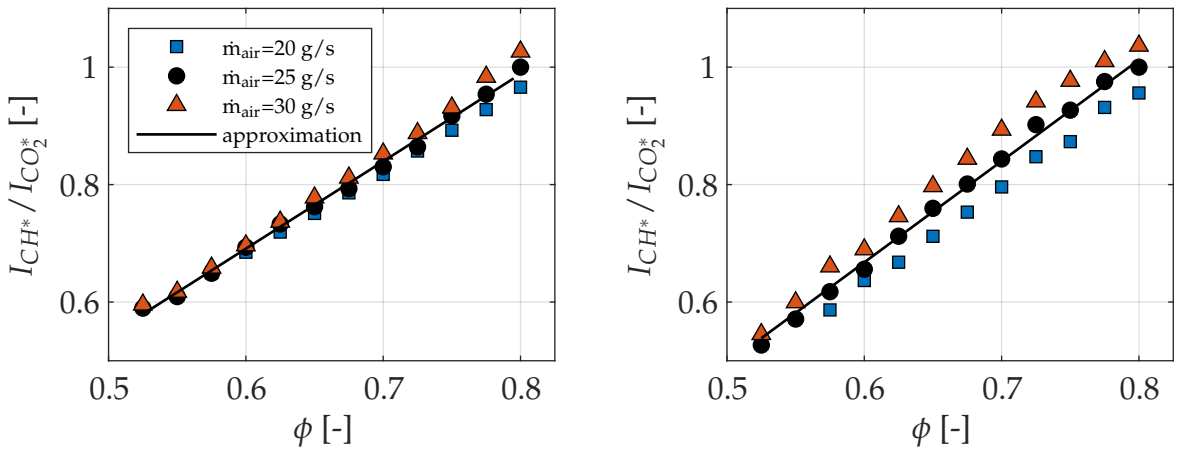

Figure 6.5: The correlation between the CH*/CO_2* chemiluminescence ratio and the equivalence ratio ϕ for natural gas (left) and kerosene combustion (right) under atmospheric conditions for different air mass flow rates. All values are normalized with the respective ratio at ϕ=0.8 and $\dot{m}_{air}$=25 g/s.

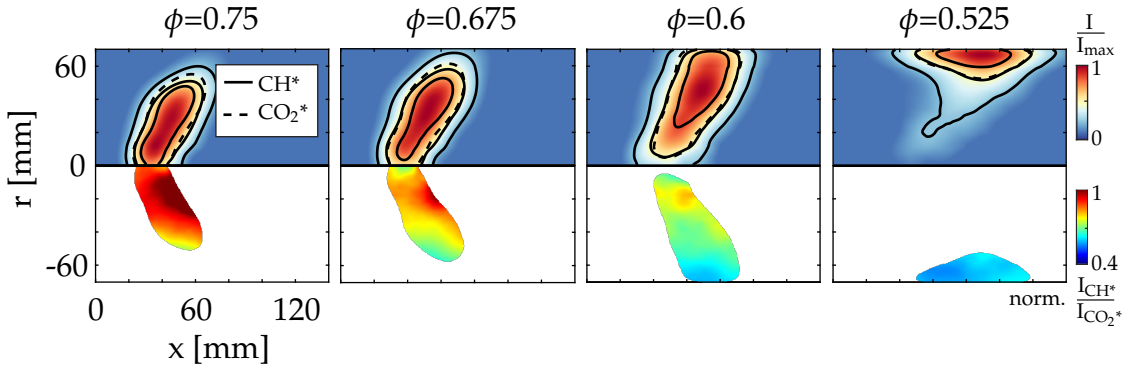

Figure 6.6: Upper half: Locally resolved CH* chemiluminescence intensity for natural gas combustion at an air mass flow rate of $\dot{m}_{air}$=25 g/s. The solid black lines represent the 75%, 50% and 25% isolines of the chemiluminescence intensity. The dashed black line represents the 50% isoline of the corresponding CO_2* chemiluminescence intensity. Lower half: Locally resolved CH*/CO_2* distribution. The values are normalized with the global CH*/CO_2* ratio at ϕ=0.8 and $\dot{m}_{air}$=25 g/s.

ized with their maximum value. The flame images show that the radial flame extension increases with decreasing equivalence ratio and that the flame moves downstream due to the lower reactivity. From the contour plots, it can be seen that CH* and CO_2* are formed at almost the same location. In the lower half of Figure 6.6, the corresponding CH*/CO_2* ratio is plotted. It can be seen that the local CH*/CO_2* ratio decreases with decreasing equivalence ratio. A homogeneous distribution of the CH*/CO_2* ratio and thus a homogeneous distribution of the equivalence ratio is observed in almost the entire flame region. In the largest part of the reaction zone, the local deviation from the global CH*/CO_2* ratio is less than 5%. If the ratio indeed depends only on the equivalence ratio, a homogeneous distribution over the entire flame front is to be expected, since no fluctuations of the equivalence ratio occur in perfectly premixed combustion. It is noticeable that the CH*/CO_2* distribution always deviates from the global ratio in the same two areas of the flame for all the ratios presented. In the area of the inner recirculation zone, a local increase of the CH*/CO_2* ratio is observed, and in the area close to the wall, the ratio is below the mean value. The local temperature in the reaction zone seems to influence the ratio, which will be investigated in more detail hereafter.

Figure 6.7 depicts the CH* flame images as well as the corresponding local CH*/CO_2* distribution for a variation of the air mass flow rate ranging between $\dot{m}_{air}$=20 g/s and $\dot{m}_{air}$=30 g/s at a constant equivalence ratio of ϕ=0.775. In contrast to the variation of the equivalence ratio, the flame structure hardly changes when the mass flow rate is varied. The flame is observed to extend only slightly in radial direction with increasing mass flow rate. This is due to the simultaneous variation of both the air and fuel mass flow rates at a fixed equivalence ratio, resulting in a self-similar flow field. A slight increase in the local CH*/CO_2* ratio with increasing mass flow rate can be seen. The CH*/CO_2* ratio again shows the same characteristics already observed in Figure 6.6. In the region of the inner recirculation zone, above-average ratio values are detected, while near the wall the ratio decreases. It is noticeable that with increasing mass

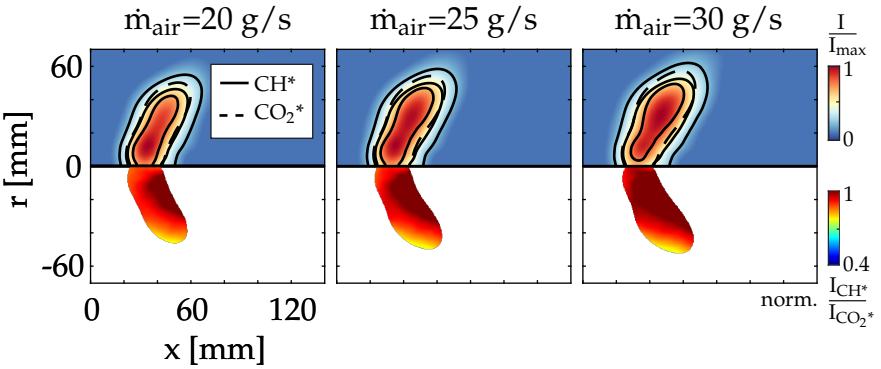

Figure 6.7: Upper half: Locally resolved CH* chemiluminescence intensity for natural gas combustion for an equivalence ratio of ϕ=0.775. The solid black lines represent the 75%, 50% and 25% isolines of the chemiluminescence intensity. The dashed black line represents the 50% isoline of the corresponding CO_2* chemiluminescence intensity. Lower half: Locally resolved CH*/CO_2* distribution. The values are normalized with the global CH*/CO_2* ratio at ϕ=0.8 and $\dot{m}_{air}$=25 g/s.

flow rate, the local CH*/CO_2* ratio increases slightly, although the flame shape and equivalence ratio remain almost unchanged.

Figure 6.8 shows the global CH*/CO_2* ratio for a variation of the air mass flow rate $\dot{m}_{air}$ for three different equivalence ratios. All three equivalence ratios show an increase in the CH*/CO_2* ratio with increasing mass flow rate. It is assumed that the impingement air cooling of the combustion chamber dissipates a constant heat flux, resulting in an increase in reaction zone temperature as the mass flow rate increases. This indicates that the CH*/CO_2* ratio is additionally affected by the local temperature in the reaction zone. To substantiate this assumption, the influence of the preheating temperature on the global CH*/CO_2* ratio is shown in Figure 6.9. The global CH*/CO_2* ratio is investigated for three different equivalence ratios for a variation of the preheating temperature in the range between 200 and 300°C. All values are normalized with the respective ratio at maximum preheating temperature. The ratio exhibits a linear decrease as the preheating temperature decreases for all equivalence ra-

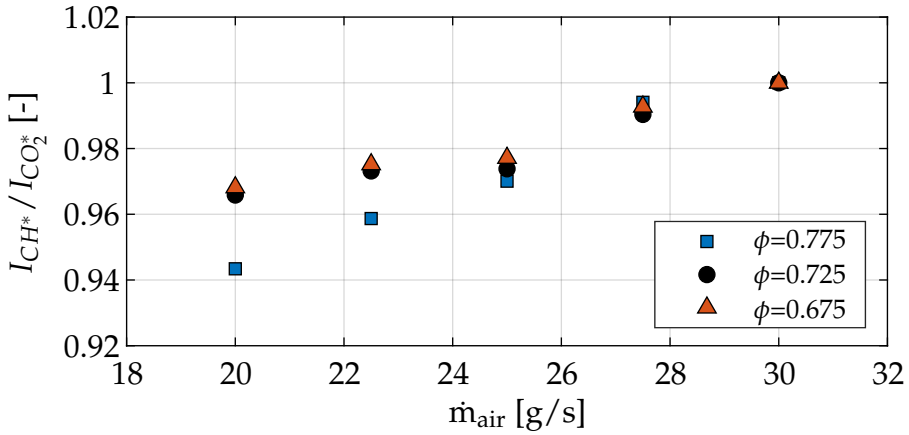

Figure 6.8: The correlation between the CH^*/CO_2^* chemiluminescence ratio and the air mass flow rate $\dot{m}_{air}$ for natural gas combustion for different equivalence ratios. All values are normalized with the respective ratio at $\dot{m}_{air}$=30 g/s.

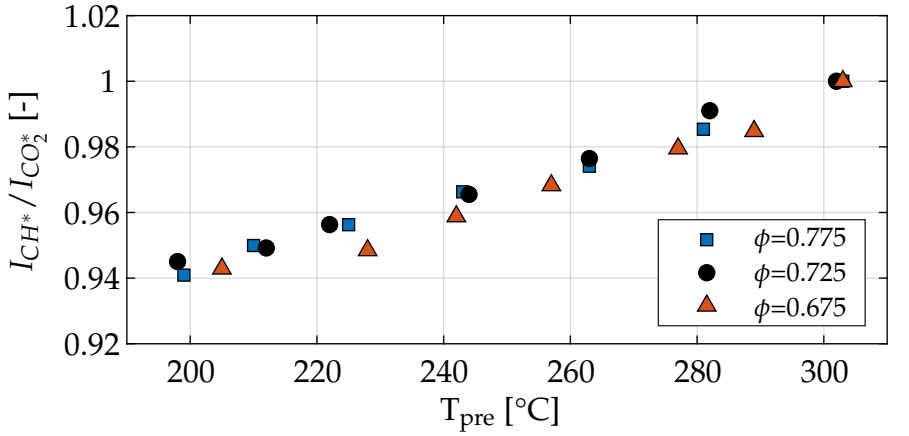

Figure 6.9: The correlation between the CH^*/CO_2^* chemiluminescence ratio and the preheating temperature T_{pre} for natural gas combustion for different equivalence ratios. All values are normalized with the respective ratio at maximum preheating temperature.

tios. Reducing the preheating temperature from 300 to 200°C results in a decrease of the global CH^*/CO_2^* ratio by about 6%. Decreasing the preheating temperature from 300 to 200°C leads to a reduction in adiabatic flame temperature of approximately 70 K for all three equivalence ratios. This strongly indicates that the CH^*/CO_2^* ratio is influenced by the temperature in the combustion chamber. This observation supports the hypothesis that the increase in the ratio with increasing mass flow rate is due to the increase in the temperature in the reaction zone (cf. Figure 6.8). Assuming the findings obtained from the global CH^*/CO_2^* ratio analysis to be applicable to the local CH^*/CO_2^* distribution as well, an inhomogeneous distribution of the ratio over the flame front might be attributable to temperature gradients in the reaction zone. Thus, the local deviations of the CH^*/CO_2^* as shown in Figure 6.7 may indicate temperature gradients in the reaction zone. Based on the CH^*/CO_2^* distribution, the assumed temperature in the region of the inner recirculation zone is thus higher than in the region of the outer recirculation zone. This is in line with expectations, since significantly higher heat losses are to be expected in the outer recirculation zone than in the inner recirculation zone. Due to the low velocity in the outer recirculation zone and the resulting long residence time, high heat losses are to be expected, leading to a significant reduction in reactivity in this area [63].

Figure 6.10 shows the CH^* flame images and the corresponding CH^*/CO_2^* distribution for kerosene combustion for different equivalence ratios at a constant air mass flow rate of $\dot{m}_{air}$=25 g/s. A trend similar to natural gas combustion is observed. As the equivalence ratio decreases, the flame is moving downstream and the radial extension increases due to decreasing reactivity. It can be clearly seen that the CH^*/CO_2^* ratio decreases with decreasing equivalence ratio. It is also noticeable for kerosene combustion that the ratio over the flame front shows deviations from the mean ratio in the same areas as observed for natural gas combustion. A local increase in the CH^*/CO_2^* ratio is observed in the region of the inner recirculation zone, and the ratio is below the mean in the region close to the wall. Considering the flow field in the

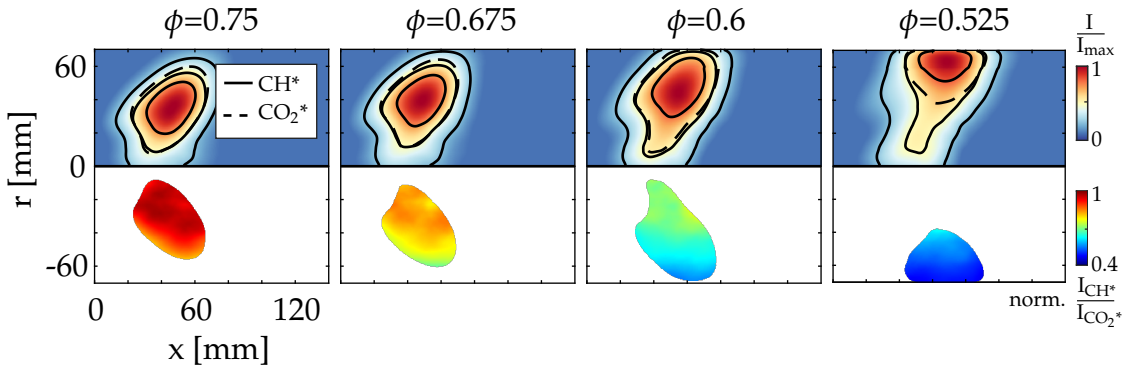

Figure 6.10: Upper half: Locally resolved CH* chemiluminescence intensity for kerosene combustion at an air mass flow rate of $\dot{m}_{air}$=25 g/s. The solid black lines represent the 75%, 50% and 25% isolines of the chemiluminescence intensity. The dashed black line represents the 50% isoline of the corresponding CO_2* chemiluminescence intensity. Lower half: Locally resolved CH*/CO_2* distribution. The values are normalized with the global CH*/CO_2* ratio at ϕ=0.8 and $\dot{m}_{air}$=25 g/s.

combustion chamber to be similar to that for natural gas combustion, it can be assumed that the local deviation of the ratio is again caused by temperature gradients in the reaction zone. The ratio is observed to be homogeneously distributed over most parts of the flame front, suggesting a homogeneous distribution of the equivalence ratio. Thus, the global analysis of flame chemiluminescence as carried out in parts of this study seems to be justified for premixed flames. This could not be anticipated in advance, as the fuel is injected into the burner, where perfect mixing cannot be assumed a priori. This indirectly proves that the system investigated is in fact a well premixed system, which was already verified by the low NO_x emissions [58].

7 Equivalence Ratio Fluctuations During Acoustic Excitation

In this chapter, equivalence ratio fluctuations during acoustic excitation for premixed natural gas and kerosene combustion are discussed. First, scattering matrices of the A^2EV burner without flame are presented to determine the influence of the twin-fluid nozzle on the acoustic properties of the swirl burner. These are required for determining the velocity fluctuations at burner outlet. Second, experimentally determined equivalence ratio fluctuations obtained by the bandpass filtered chemiluminescence technique are discussed. Finally, equivalence ratio transfer functions for different operating points for natural gas and kerosene combustion are presented. The objective is to identify the parameters affecting the propagation of the equivalence ratio wave. In addition, differences between gaseous and liquid fuel supply on the propagation of equivalence ratio waves are elucidated. Here, the influence of complex mixture preparation for liquid fuel operation on the equivalence ratio transfer function is investigated in more detail.

7.1 Velocity Fluctuations at the Burner Outlet

In order to calculate the velocity fluctuations at the burner outlet, the scattering matrices of the burner are required. The scattering matrices are determined experimentally in the test rig without flame with a main air mass flow of $\dot{m}_{air}$=25 g/s and a preheating temperature of T_{pre}=573 K. When using the burner with the twin-fluid nozzle, an additional atomizing air mass flow of 3.5% of the main air mass flow is supplied.

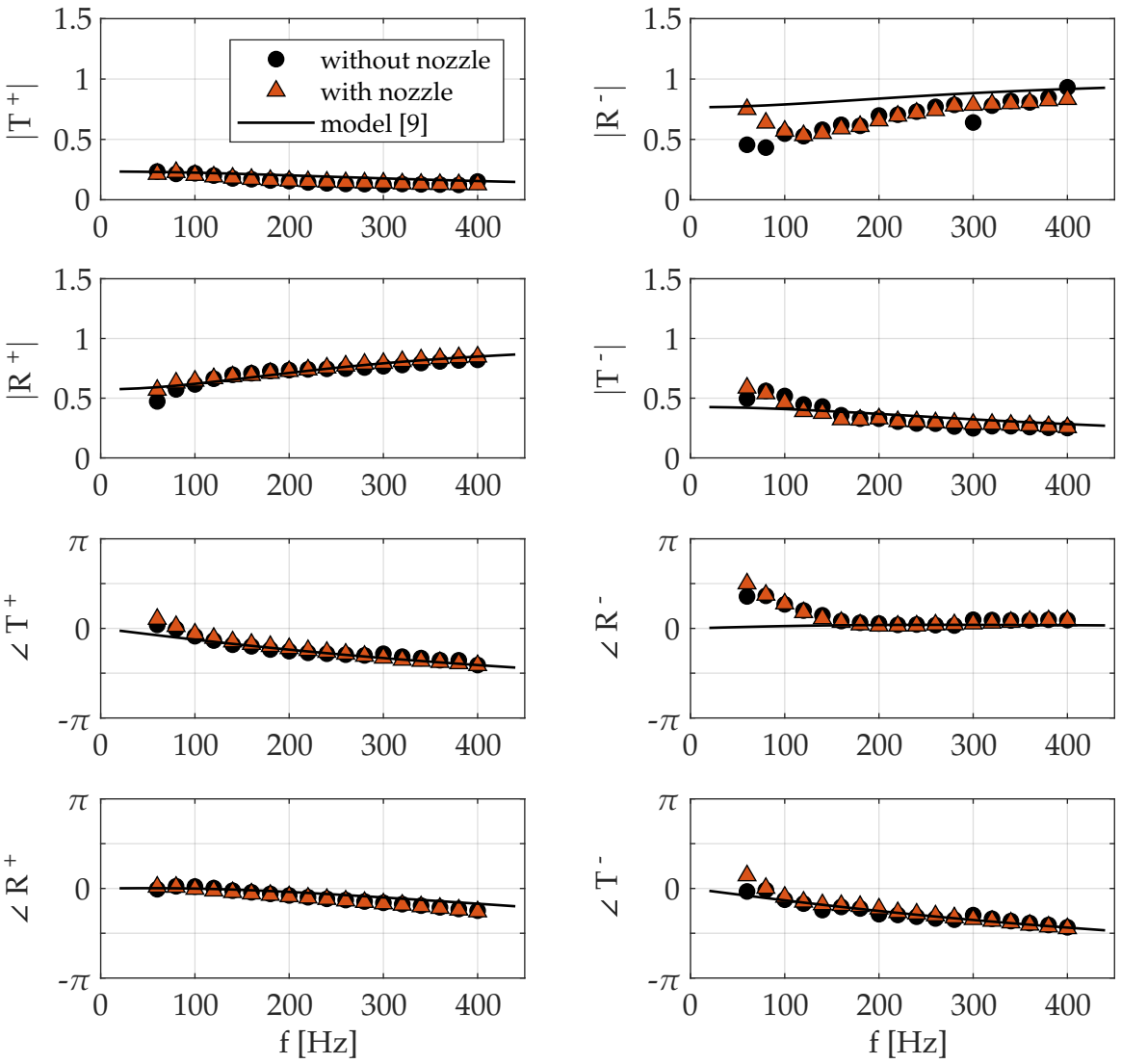

Figure 7.1: Comparison of the scattering matrices of the A^{2}EV burner in its original configuration and with the twin-fluid nozzle installed. In addition, the modeled scattering matrix derived from the network model of the burner by Bade is shown [9].

All experiments without combustion are carried out without fuel injection. Figure 7.1 shows the experimentally determined scattering matrices of the burner with the twin-fluid nozzle installed together with those of the original burner. Thus, the influence of the twin-fluid nozzle on the burner acoustics can be determined. It is observed that the scattering ma-

trices of the two burner configurations are almost identical. The maximum amplitude of the transmission coefficients $|T^+|$ and $|T^-|$ is found at 60 Hz and as the frequency increases, the amplitude decreases. The corresponding phases show a continuous decrease with increasing frequency. The amplitude of the reflection coefficient $|R^+|$ shows its minimum at a frequency of 60 Hz and increases with increasing frequency, slowly approaching a magnitude of unity. The corresponding phases decrease again continuously with increasing frequency. The amplitude response of the reflection coefficient $|R^-|$ shows a similar trend to the reflection coefficient $|R^+|$. The magnitude reaches its maximum of about one at a frequency of 400 Hz and decreases with decreasing frequency. For frequencies below 100 Hz, a slight increase in magnitude can be seen. The corresponding phase is zero over the major frequency range. For frequencies below 150 Hz, a slight increase in phase with decreasing frequency is observed. Thus, it can be concluded that the acoustic properties of the A^2EV burner are not influenced by the twin-fluid nozzle. Similar findings have already been reported by Stadlmair [123]. He installed a similar twin-fluid nozzle for water injection and observed the acoustic characteristics of the A^2EV burner to be unaffected by the modification.

Figure 7.1 also contains the modeled scattering matrix for the A^2EV burner at the same operating conditions. The scattering matrix was derived from the network model developed by Bade [9]. The network model consists of several tubular ducts, area changes as well as junctions and thus represents an accurate approximation of the real burner geometry. A detailed description of the network model is provided by Bade [8]. It can be seen that the model agrees very well with the experimentally determined scattering matrices. Only the magnitude and phase of the reflection coefficient R^- exhibit minimal deviations between the model and the experimentally determined scattering matrices in the low frequency range. These deviations might also be due to the weak acoustic forcing capacities of the downstream siren at low frequencies, which was already reported by Stadlmair [123]. Due to the excellent agreement of the model with the experimental data, only the modeled scattering matrices

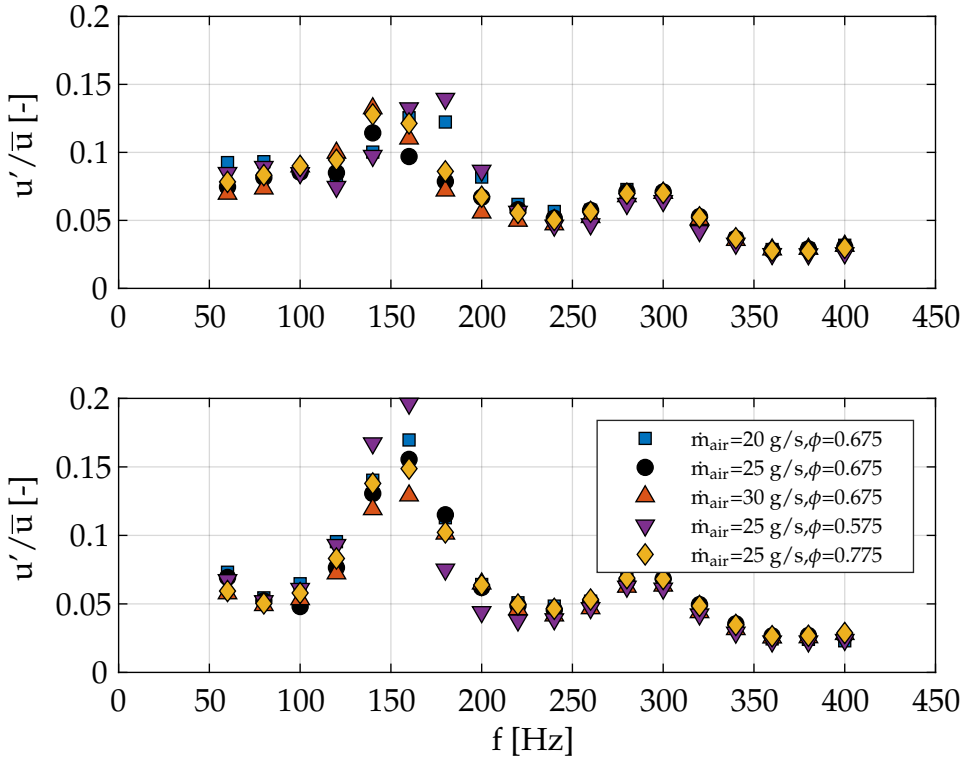

Figure 7.2: Relative magnitude of the acoustic velocity fluctuations at the burner outlet for natural gas (upper half) and kerosene combustion (lower half).

are used in the following to calculate the velocity at the burner outlet. The modeled scattering matrices used to calculate the velocity variations for different main air mass flows can be found in the Appendix.

The scattering matrix linearly links the Riemann invariants at the burner inlet to those at the burner outlet. According to equations 3.25 and 3.26, the acoustic pressure and velocity at the burner outlet is then calculated using the Riemann invariants f and g at the burner outlet. Figure 7.2 shows the amplitude of the velocity fluctuations at the burner outlet for technically premixed natural gas and kerosene combustion. A similar trend is observed for both burner configurations. For most of the frequency range investigated, the forcing amplitude is between 5% and 10%. For frequencies above 300 Hz, the excitation amplitude drops to values below 5%. Pronounced maxima of velocity fluctuations are ob-

served at frequencies of 150 and 300 Hz. These frequencies correspond to the eigenfrequencies of the plenum, resulting in an increase of the forcing amplitude [80]. The eigenfrequencies of the plenum are calculated according to Equation 3.32. The peak velocity fluctuations at the burner outlet are larger in the case of kerosene combustion compared to the natural gas case. The same observation was already reported by Kaufmann, who demonstrated that this effect depends on the flame structure and not on the fuel type [58]. The velocity fluctuations for perfectly premixed natural gas combustion at the reference operating point are identical to the technically premixed case.

7.2 Equivalence Ratio Fluctuations in the Reaction Zone

Equivalence ratio fluctuations are determined optically based on the CH* and CO_2* chemiluminescence intensity, as presented in Section 5.3.2. First, phase-resolved CH* and CO_2* flame images during acoustic excitation for perfectly and technically premixed natural gas as well as kerosene combustion are presented. Subsequently, global fluctuations of CH* and CO_2* chemiluminescence intensity and the equivalence ratio are discussed. All results presented in this subsection represent the reference operating point with an equivalence ratio of ϕ=0.675 and an air mass flow rate of $\dot{m}_{air}$=25 g/s.

Figure 7.3 presents phase-resolved flame images for four different oscillation phases for perfectly premixed natural gas combustion at an excitation frequency of 240 Hz. The upper half of the figure shows the CH* flame images, the lower half the corresponding CO_2* flame images. Due to the rotational symmetry of the flame, only half of the image is depicted. All images are normalized with the maximum value during oscillation. The dashed line additionally represents the 50% isoline of the time-averaged mean image of the respective species. Based on the contour plots, it can be seen that CH* and CO_2* appear almost at the same position. An axial movement of the reaction zone is recognizable over

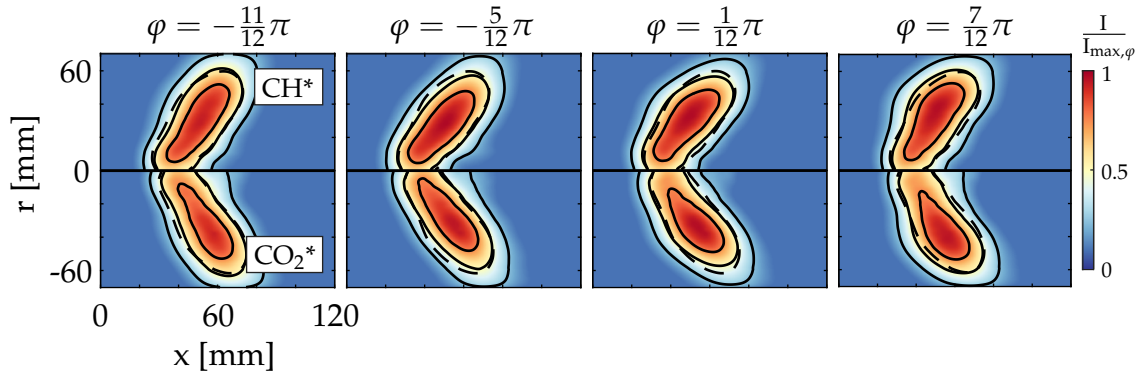

Figure 7.3: Phase-resolved CH* and CO_2* chemiluminescence intensity for perfectly premixed natural gas combustion at an excitation frequency of f=240 Hz. The solid black lines represent the 75%, 50% and 25% isolines of the chemiluminescence intensity. The dashed black line shows the 50% isoline of the time-averaged mean image.

one oscillation cycle. Only small intensity modulations are observed for both CH* and CO_2* chemiluminescence.

Figure 7.4 shows the phase-resolved CH* and CO_2* flame images for technically premixed natural gas combustion at the same operating point as for the perfectly premixed case. Significantly higher intensity variations are observed for technically premixed natural gas combustion compared to perfectly premixed combustion. At a phase of φ=1/12π, the chemiluminescence intensity drops almost below 75% of the maximum intensity. This is illustrated by nearly no visibility of the 75% isoline of the chemiluminescence intensity of the corresponding species. These significantly stronger intensity fluctuations indicate the presence of equivalence ratio fluctuations (which are not present for perfectly premixed combustion). Since the chemiluminescence intensity of the individual species depends exponentially on the equivalence ratio, small fluctuations in the equivalence ratio can already cause noticeable intensity fluctuations [44]. A similarly strong intensity oscillation is also observed for the kerosene flame, which is depicted in Figure 7.5

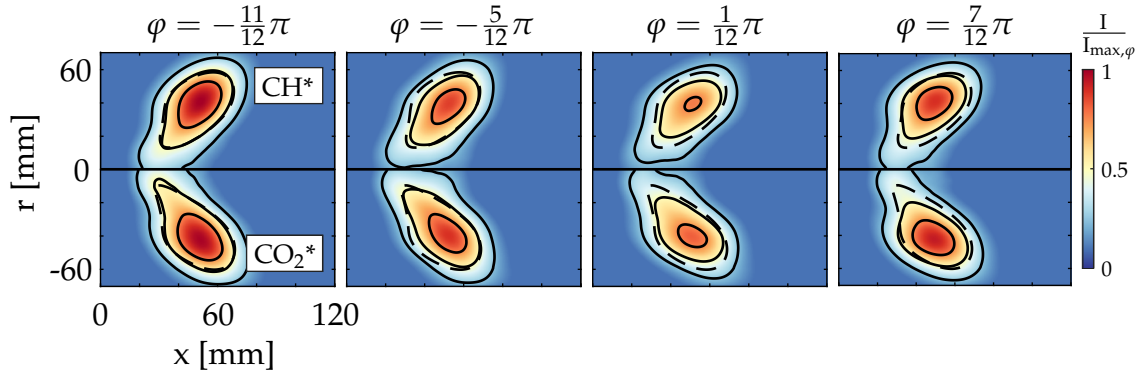

Figure 7.4: Phase-resolved CH* and CO_2* chemiluminescence intensity for technically premixed natural gas combustion at an excitation frequency of f=240 Hz. The solid black lines represent the 75%, 50% and 25% isolines of the chemiluminescence intensity. The dashed black line shows the 50% isoline of the time-averaged mean image.

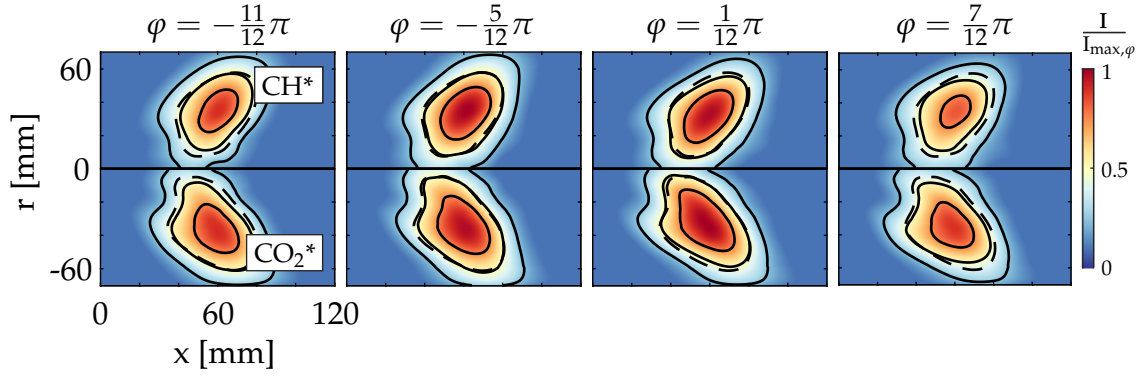

Figure 7.5: Phase-resolved CH* and CO_2* chemiluminescence intensity for kerosene combustion at an excitation frequency of f=240 Hz. The solid black lines represent the 75%, 50% and 25% isolines of the chemiluminescence intensity. The dashed black line shows the 50% isoline of the time-averaged mean image.

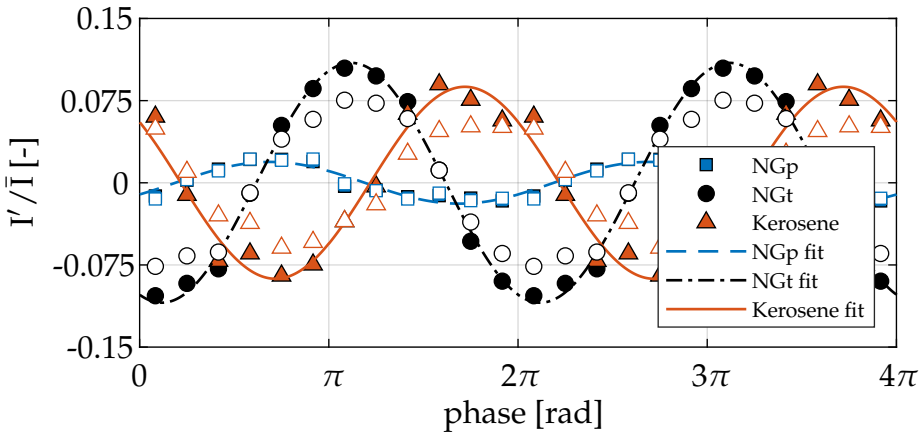

Figure 7.6: Chemiluminescence fluctuations over two oscillations at the reference operating point for an excitation frequency of f=240 Hz. Filled symbols denote CH* chemiluminescence, unfilled symbols represent CO_2* chemiluminescence. Lines indicate the approximation of CH* chemiluminescence.

By integrating the corresponding locally resolved intensity distributions over the flame front, global values for CH* and CO_2* chemiluminescence are obtained. Figure 7.6 presents the normalized fluctuating component of the global CH* and CO_2* chemiluminescence for natural gas and kerosene combustion at an excitation frequency of 240 Hz. The normalized forcing amplitudes obtained at this frequency at the burner outlet $|u'_b|/\bar{u}_b$ are about 5% for all three cases. It is clearly seen that the amplitude of CH* chemiluminescence for technically premixed natural gas combustion is significantly larger than in the perfectly premixed case. The amplitude for perfectly premixed natural gas combustion is barely over 2%, whereas in the technically premixed case it exceeds 10%. These differences in intensity fluctuations were already observed in the locally resolved images (cf. Fig. 7.3 and Fig 7.4). A similar finding was already reported by Peterleithner et al. for this burner [102]. They observed that the amplitude of OH* chemiluminescence oscillation in the technically premixed case is higher by a factor of 6 than in the perfectly premixed case at an excitation frequency of 200 Hz. As already mentioned above, equivalence ratio fluctuations lead to higher intensity fluctuations in the

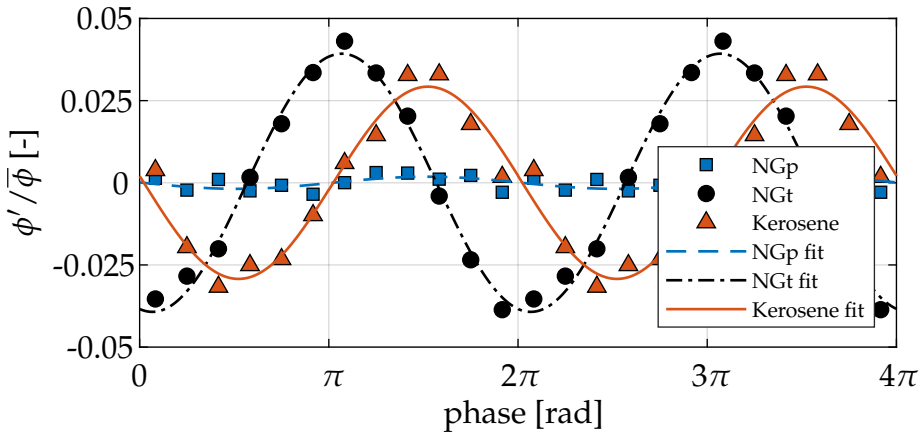

Figure 7.7: Equivalence ratio fluctuations over two oscillations at the reference operating point for an excitation frequency of f=240 Hz.

technically premixed case. The amplitudes for technically premixed natural gas and kerosene combustion are roughly of the same magnitude. In addition, Figure 7.6 also includes the intensity fluctuations for CO_2* chemiluminescence. Comparing the amplitudes of CH* and CO_2*, it is noticeable that the amplitude for CO_2* is slightly lower than for CH* for technically premixed natural gas and kerosene combustion. For perfectly premixed natural gas combustion, the CH* and CO_2* chemiluminescence fluctuation is exactly the same. No phase difference is observed between CH* and CO_2* oscillations for all three cases.

Equivalence ratio fluctuations during acoustic excitation are determined using the calibration chart (cf. Fig. 6.5) and the procedure presented in Section 5.3.2. Figure 7.7 illustrates the normalized fluctuating component of the equivalence ratio at the reference operating point during two oscillations for an excitation frequency of f=240 Hz. The amplitude of the equivalence ratio wave for technically premixed natural gas combustion is approximately 4% and for kerosene combustion around 3%. It can be clearly seen that the experimental data can be approximated quite accurately by a harmonic wave. Furthermore, the equivalence ratio wave for perfectly premixed natural gas combustion is presented. As expected, virtually no fluctuations in the equivalence ratio are observed. This can

be indirectly interpreted as a validation of the presented measurement technique.

7.3 Equivalence Ratio Transfer Functions

This section examines the influence of liquid fuel supply on the propagation of equivalence ratio fluctuations compared to gaseous fuel supply based on experimentally determined equivalence ratio transfer functions. As stated in Section 3.3.1, the equivalence ratio transfer function relates the equivalence ratio fluctuations in the flame to the velocity fluctuations at the burner outlet. First, the phase response of the equivalence ratio transfer function for different operating points for natural gas and kerosene combustion is presented. The phase response provides information regarding the time delay of the system. Subsequently, the amplitude of the transfer function at the reference operating point is depicted to highlight differences between gaseous and liquid fuel injection. Last, the influence of the global equivalence ratio as well as the air mass flow rate on the propagation of equivalence ratio fluctuations is investigated for both configurations.

Figure 7.8 shows the phase response of the equivalence ratio transfer function for five different operating points for natural gas and kerosene combustion, respectively. A linear phase slope is evident for all operating points, corresponding to a constant convective time delay between fuel injection and flame. The low frequency limit behavior is $\lim_{Sr\to 0} \angle(TF_\phi) = \pi$, implying a phase shift of equivalence ratio fluctuations and velocity fluctuations at the fuel injection location, already addressed in Section 3.3.1. Furthermore, it can be seen that the phase gradient for kerosene combustion is steeper than for natural gas combustion, indicating that the time delay from fuel injection to flame is larger for the liquid fuel than for the gaseous fuel. This finding suggests that there is an additional mechanism leading to an increased time delay for liquid fuel combustion compared to gas combustion. Droplet acceleration causes this additional

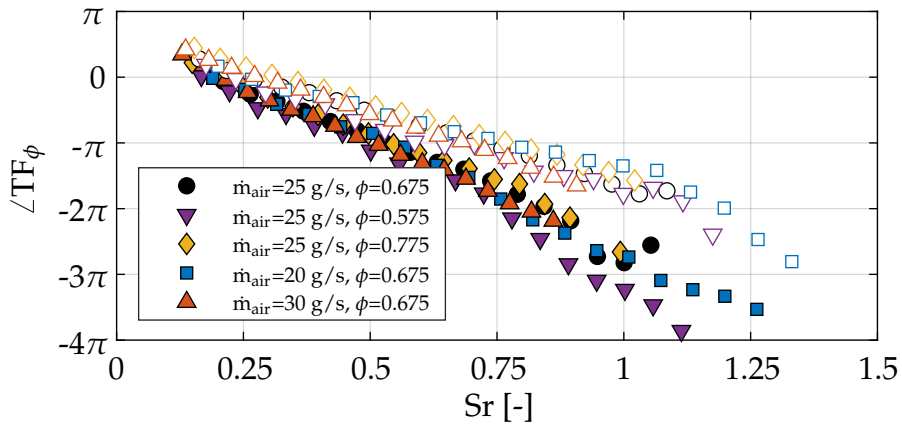

Figure 7.8: Phase of the equivalence ratio transfer function. Unfilled symbols denote natural gas, filled ones kerosene.

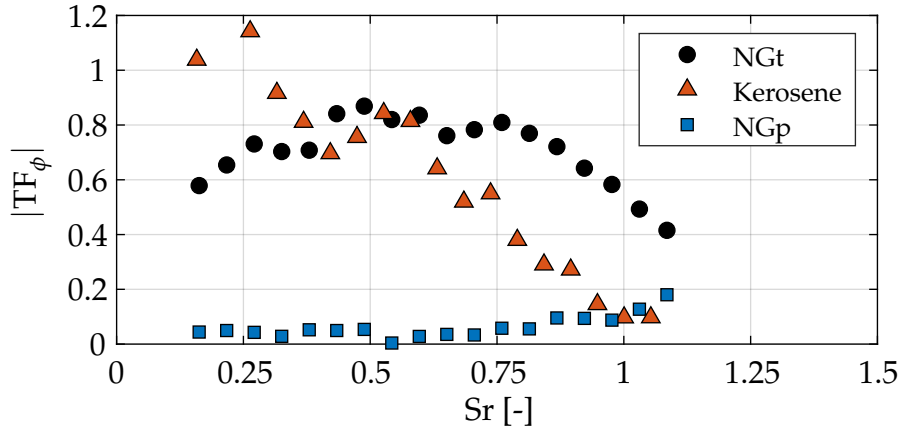

Figure 7.9: Amplitude of the equivalence ratio transfer function at the reference operating point ($\dot{m}_{air}$=25 g/s, ϕ=0.675).

time delay, which will be examined in more detail in Section 8.2.

The amplitude of the equivalence ratio transfer function at the reference operating point is depicted in Figure 7.9. Experimental results of premixed natural gas combustion are compared to kerosene combustion. Note that the Strouhal number for perfectly premixed combustion was set to the same value as for technical premixed combustion. As expected, for perfectly premixed natural gas combustion, an amplitude of approximately zero is observed over the entire frequency range, which successfully validates the presented measurement technique. For tech-

nically premixed natural gas and kerosene combustion, the amplitude of the equivalence ratio transfer function converges to unity for very low Strouhal numbers and decreases with increasing Strouhal number. A stronger decrease in gain is seen for kerosene combustion compared to natural gas. This might be due to the complex, spatially distributed mixture preparation for the liquid fuel, which leads to a stronger spatial dispersion of the equivalence ratio wave compared to the gas case. For natural gas, a decrease in gain with decreasing Strouhal number is furthermore observed for $\mathrm{Sr} < 0.4$. Strong swirl fluctuations are expected to be present in this range, resulting in increased mixing and thus contributing to a reduction in the amplitude of the equivalence ratio transfer function [49]. This assumption is corroborated by the observation of a strong axial movement of the flame in this range. Such strong axial movement is not observed for kerosene combustion. A significant influence of coherent flow structures on the propagation of equivalence ratio fluctuations for natural gas combustion was also observed by Bluemner [13].

Figure 7.10 shows the amplitude of the equivalence ratio transfer function for a variation of the main air mass flow. A stronger amplitude decay of the equivalence ratio transfer function with decreasing air mass flow rate is observed. As already reported by Schuermans et al. the axial flame extension cannot be considered negligibly small compared to the convective wavelength of the equivalence ratio wave [119]. The convective wavelength decreases with decreasing mass flow rate, whereas the axial flame extension is approximately the same for all three mass flow rates (cf. Fig. 8.7). As a result, the ratio of axial flame extension to convective wavelength increases as the mass flow rate decreases, leading to a stronger decrease in the gain of the equivalence ratio transfer function. Hence, it can be concluded that the ratio of axial flame extension to convective wavelength has a strong influence on the amplitude of the equivalence ratio transfer function. This observation will be examined in more detail in Section 8.3.

Finally, the influence of the global equivalence ratio on the transfer function is investigated. Figure 7.11 depicts the amplitude of the equivalence

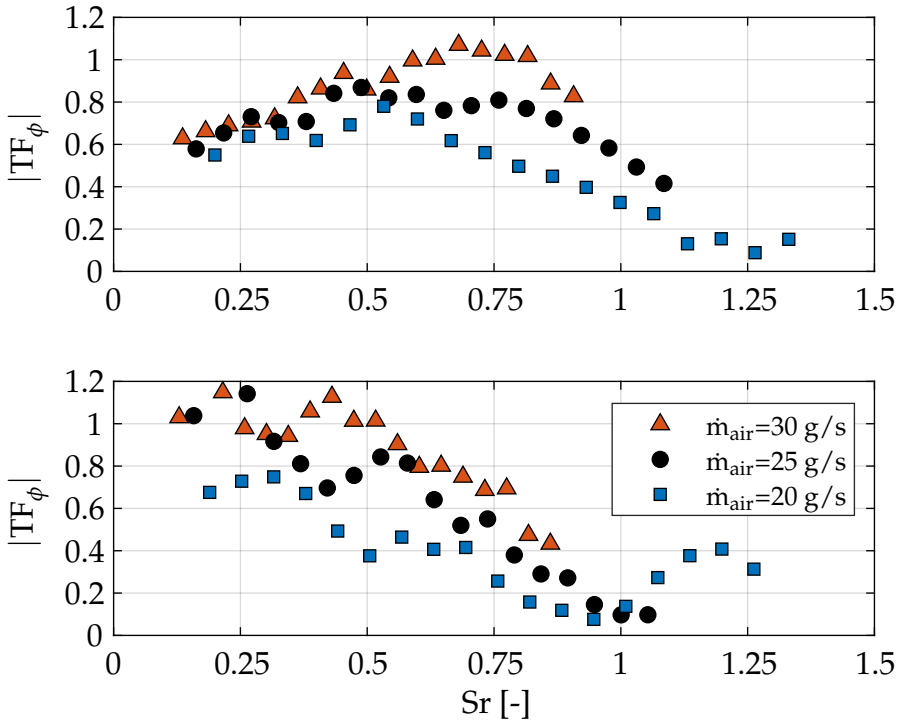

Figure 7.10: Amplitude of the equivalence ratio transfer function for different mass flow rates at a constant equivalence ratio of ϕ=0.675 for natural gas (upper half) and kerosene combustion (lower half).

ratio transfer function for a variation of the global equivalence ratio for natural gas and kerosene combustion. As the global equivalence ratio increases, the magnitude of the equivalence ratio transfer function declines less for both fuels. With decreasing equivalence ratio, an increase in axial flame extension is observed (cf. Fig. 8.7). Thus, the ratio of axial flame extension to convective wavelength increases as the equivalence ratio decreases, since the convective wavelength remains constant. As already observed in Figure 7.10, the gain of the equivalence ratio transfer function decreases more rapidly as the ratio of axial flame extension to convective wavelength increases. The axial flame extension for kerosene combustion is nearly the same for the equivalence ratios of ϕ=0.775 and ϕ=0.675. It is noticeable that an almost identical gain of the equivalence ratio transfer function is observed for these two operating points, which

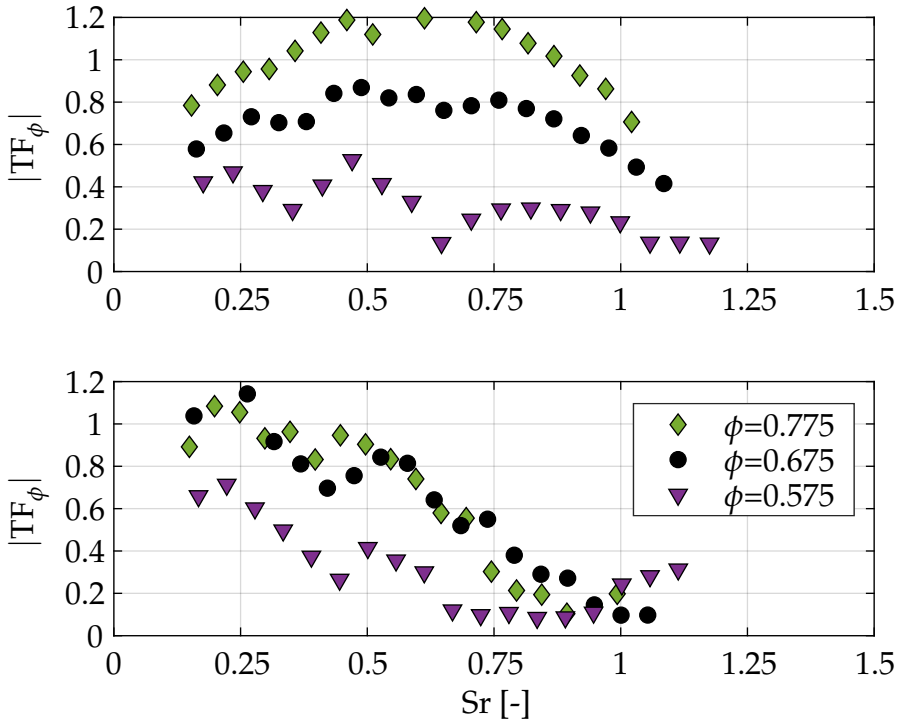

Figure 7.11: Amplitude of the equivalence ratio transfer function for different global equivalence ratios at a constant air mass flow rate of $\dot{m}_{air}$=25 g/s for natural gas (upper half) and kerosene combustion (lower half).

can be explained by a constant ratio of axial flame extension to convective wavelength. Consequently, it can be concluded that the ratio of axial flame extension to convective wavelength significantly affects the amplitude of the equivalence ratio transfer function.

8 Modeling of Equivalence Ratio Fluctuations

This section focuses on the modeling of the equivalence ratio transfer function. A time delay model is utilized to describe the propagation of equivalence ratio fluctuations, as already proposed by Schuermans et al. [119]. A model satisfying the low-frequency limit behavior from Equations 3.50 and 3.51 is chosen as follows:

$$TF_\phi = e^{i(-\omega\tau_\phi+\pi)}e^{-\frac{1}{2}\omega^2\sigma_\phi^2} \tag{8.1}$$

The time delay model contains two parameters, the time delay τ_ϕ and the time delay width σ_ϕ. First, the two parameters are determined by a least squares fit of the model to the experimental data. The objective is to verify the suitability of the model to adequately represent the equivalence ratio transfer function. Subsequently, the parameters of the time delay model are examined in more detail and a physical interpretation of these parameters is provided. Last, physically based models and empirical approaches are presented to predict the two parameters of the time delay model.

8.1 Time Delay Model

This section reviews the applicability of a time delay model to describe the propagation of equivalence ratio fluctuations adequately. Essential is the ability of the model to capture the differences observed for gaseous and liquid fuel supply. In order to model the propagation of equivalence ratio fluctuations, a time delay model with a Gaussian probability distribution of the time delay is employed (cf. Eq. 8.1). The two parameters

Table 8.1: Parameters of the time delay model.

Fuel	$\dot{m}_{air}$ [g/s]	ϕ [-]	τ_ϕ [ms]	σ_ϕ [ms]
NGt	25	0.675	3.69	0.46
	20	0.675	4.29	0.80
	30	0.675	3.36	0.15
	25	0.575	4.17	1.03
	25	0.775	3.31	0.01
Kerosene	25	0.675	4.78	0.72
	20	0.675	5.86	1.01
	30	0.675	4.10	0.39
	25	0.575	5.82	1.21
	25	0.775	4.40	0.68

of the model, the τ_ϕ and the time delay width σ_ϕ, are obtained by fitting the time delay model to the experimental data using the method of least squares for all operating points.

Table 8.1 presents the values for the time delay τ_ϕ and the time delay width σ_ϕ. First, it is noticeable that both the time delay and the time delay width for kerosene combustion are always larger than for the corresponding natural gas case. Clear trends can be identified for both parameters, which are valid for the natural gas as well as the kerosene case. A decrease in the time delay can be seen as the air mass flow rate increases. The convective transport velocity increases with increasing air mass flow rate, whereas the position of the flame remains almost unchanged, resulting in a reduction of the time delay. Furthermore, as the equivalence ratio decreases, the time delay increases. The flame stabilizes further downstream as the equivalence ratio decreases, consequently resulting in an increase in the time delay for constant transport velocity.

The time delay width indicates the decay of the gain of the equivalence ratio transfer function. An increasing time delay width results in a stronger decrease of the magnitude of the transfer function. The time delay width exhibits a decreasing trend with increasing air mass flow. As already identified in Section 7.3, the ratio of axial flame extension to convective wavelength significantly influences the magnitude of the transfer function. This ratio decreases with increasing air mass flow, which is also reflected by the time delay width. A decrease in the time delay width can also be seen as the equivalence ratio increases. This observation can also be explained based on the ratio of axial flame extension to convective wavelength. The ratio decreases as the equivalence ratio increases because the axial flame extension decreases, but the convective wavelength remains unchanged.

Figure 8.1 depicts the comparison of the experimentally determined equivalence ratio transfer functions with the corresponding time delay model for different air mass flow rates. Both, amplitude and phase are represented by the time delay model in very good agreement with experimental data for natural gas and kerosene combustion. The linear decreasing phase of the model is in excellent agreement with the experimental data. Also the decreasing gain of the equivalence ratio transfer function with increasing Strouhal number coincides very well with experimental data. The amplitude of the model approaches unity for low Strouhal numbers. For natural gas combustion, a significant deviation in amplitude between the experimentally determined transfer functions and the model is observed for $\mathrm{Sr} < 0.4$. As already suggested in Section 7.3, strong swirl fluctuations are causing the decreasing gain, which of course cannot be reproduced by the model. The comparison of the experimentally determined equivalence ratio transfer functions with the corresponding time delay model for different global equivalence ratios is presented in Figure 8.2. A good agreement of the model with the experimental data is also observed for the variation of the global equivalence ratio. Only for natural gas combustion at an equivalence ratio of ϕ=0.775 major deviations in amplitude between model and experimental data are seen.

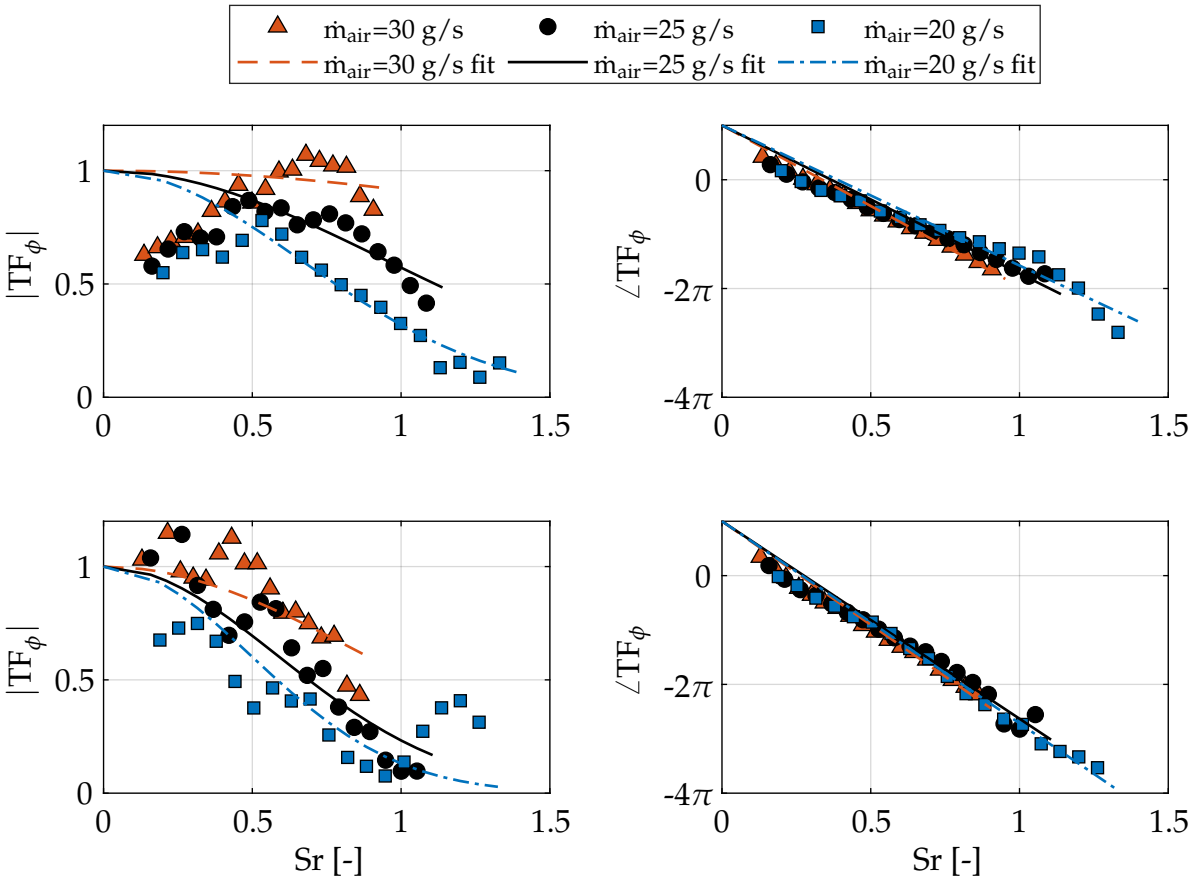

Figure 8.1: Comparison of the experimentally determined equivalence ratio transfer functions with the corresponding time delay model for different air mass flow rates at a constant equivalence ratio of ϕ=0.675. Model is fitted to the experimental data using least squares method. Data for natural gas combustion are shown in the upper half of the figure and for kerosene combustion in the lower half.

For this operating point, the amplitude of the experimentally determined transfer function has values greater than unity for most of the data. The presented time delay model cannot assume values greater than unity and thus fails to approximate this operating point in sufficiently good quality.

Summarizing, the propagation of equivalence ratio fluctuations can be adequately approximated by the time delay model. The time delay model is capable of approximating both the magnitude and phase of the equiv-

alence ratio transfer function in sufficiently good quality. However, the determined parameters of the time delay model are based only on a least squares fit of the model to the experimental data. Therefore, a physical interpretation and modeling of these parameters is provided in the following sections.

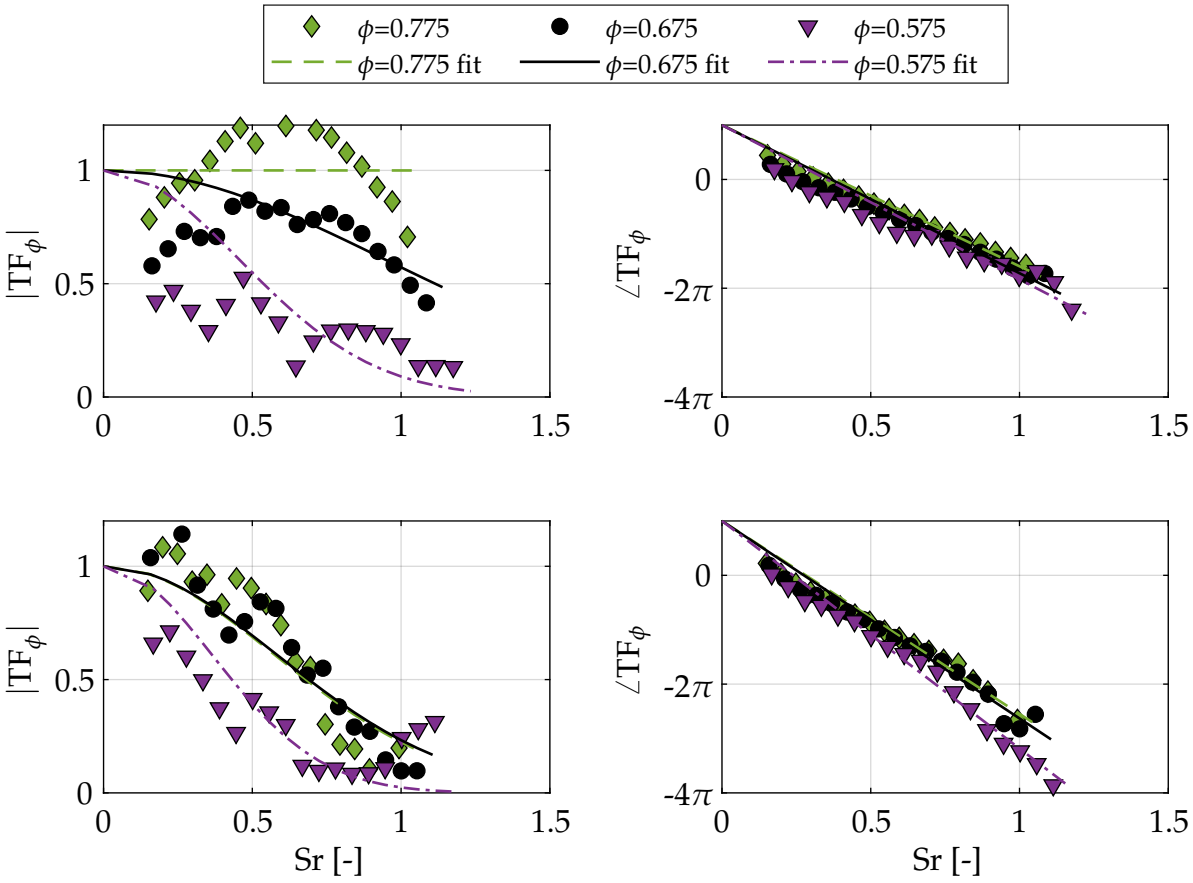

Figure 8.2: Comparison of the experimentally determined equivalence ratio transfer functions with the corresponding time delay model for different global equivalence ratios at a constant air mass flow rate of $\dot{m}_{air}$=25 g/s. Model is fitted to the experimental data using least squares method. Data for natural gas combustion are shown in the upper half of the figure and for kerosene combustion in the lower half.

8.2 Time Delay Analysis

This section presents an approach for calculating the time delay of the equivalence ratio transfer function for both natural gas and kerosene combustion based on one-dimensional physical models. The time delay specifies the time that elapses before the flame responds to a disturbance at the position of the fuel supply. Three individual processes are identified accumulating to the total time delay, which will be presented in detail subsequently.

The first part represents the time delay in the mixing tube τ_{mix}. The convective time delay from injector to burner outlet is calculated according to Equation 3.58. In the case of natural gas combustion, the fuel injection is distributed along the trailing edges of the swirl slots (cf. Fig. 4.2). Simplifying, it is assumed that the injection takes place at one position in the center of the slots. For kerosene combustion, the tip of the injector nozzle is chosen as the injection location. The fuel mass flow rate is neglected in the calculation, resulting in constant time delays for the operating points with the same air mass flow. The time delay decreases with increasing air mass flow, due to increasing flow velocities. In general, time delays are lower for the kerosene case since the distance from fuel supply to burner outlet is shorter than for the natural gas case.

The second part deals with the time delay in the combustion chamber τ_{cc}, hence from burner outlet to flame. Using the geometric flame length model of Alemela et al. [6] with customized model equations for the A^2EV burner according to Bade [8], the time delay in the combustion chamber τ_{cc} is calculated according to Equation 3.59. Figure 8.3 depicts a comparison of flame lengths from measured CH* chemiluminescence images and the flame length model of Alemela. The flame length model of Alemela generally agrees very well with the stationary flame images for both natural gas and kerosene combustion for equivalence ratios $\phi \geq 0.575$. For equivalence ratios $\phi < 0.575$, the model predicts a strong increase in flame length, which was not observed in experiments. It can

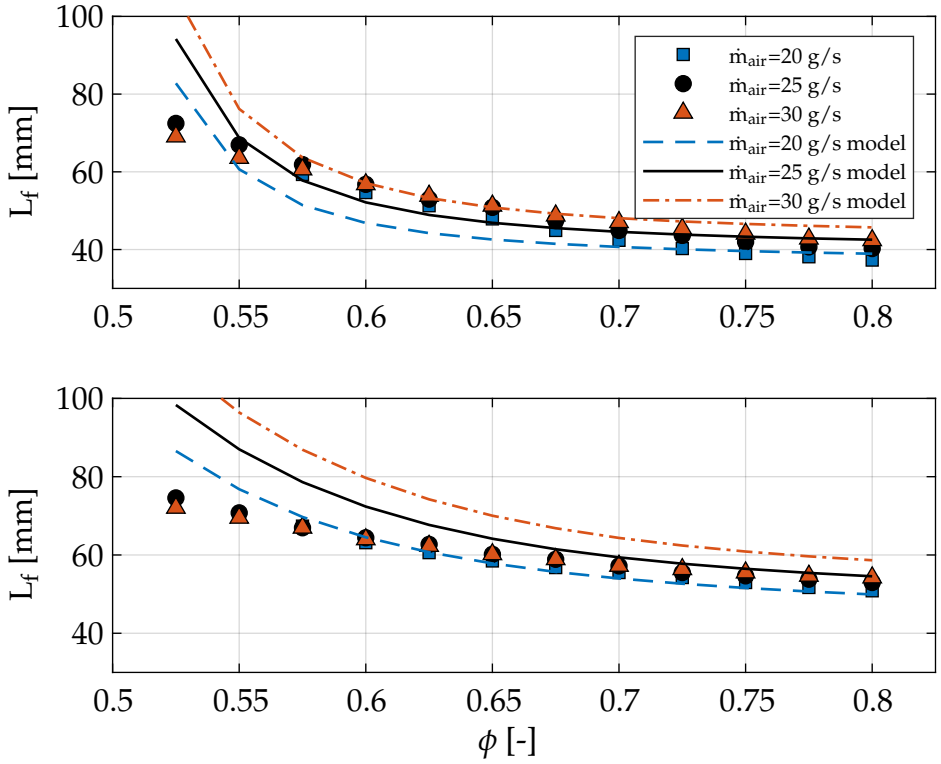

Figure 8.3: Comparison of flame lengths from measured CH* chemiluminescence images and the flame length model of Alemela [6]. Data for natural gas combustion are shown in the upper half of the figure and for kerosene combustion in the lower half.

also be seen that according to the model of Alemela, the flame length increases with increasing air mass flow rate, which, however, was only observed in the experiments for natural gas combustion for equivalence ratios $\phi > 0.675$. For kerosene combustion, the flame length is observed to be independent of the air mass flow rate over the entire investigated range.

The last process covers the time delay for droplet acceleration τ_{acc}. Owing to the negligible inertia of natural gas, a quasi instantaneous acceleration of the gas to bulk flow velocity after injection takes place. Consequently, if gaseous fuel is supplied, there is no additional time delay associated with the injection process. Unlike natural gas, droplet inertia is not negligible for liquid fuel injection, due to the huge density difference between

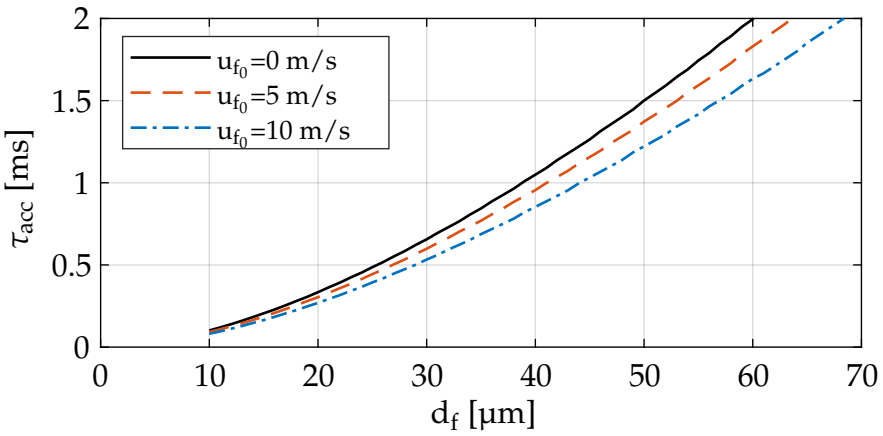

Figure 8.4: Influence of different initial droplet velocities u_{f_0} on the time delay τ_{acc} for a main air mass flow rate of $\dot{m}_{air}$=25 g/s.

air and fuel [34]. The liquid fuel is being accelerated at nozzle outlet resulting in an additional time delay for the acceleration of the droplets. Droplet velocity is calculated solving the nonlinear differential equation derived by Eckstein (cf. Eq. 3.71) [34]. Since it is very difficult to obtain accurate data regarding the size as well as the axial velocity component of the droplets due to the lack of optical accessibility to the swirler, a sensitivity analysis of the model regarding the input parameters is conducted first. According to the manufacturer's specifications, a Sauter Mean Diameter of about d_{32}=40 µm is to be expected for the twin-fluid nozzle used. Simplifying, it is assumed that all droplets have the same axial velocity and diameter, are also perfectly spherical and there is no interaction between droplets. Figure 8.4 shows the influence of different initial droplet velocities u_{f_0} on the time delay τ_{acc} for a main air mass flow rate of $\dot{m}_{air}$=25 g/s. It can be seen that increasing the initial droplet velocity results in a reduction of the time delay. For a droplet diameter of d_f=40 µm, the time delay is reduced from 1.1 ms to 0.85 ms as the initial droplet velocity is increased from 0 to 10 m/s. Figure 8.5 illustrates the influence of different bulk flow velocities $\bar{u}_b$ on the time delay τ_{acc} for an initial droplet velocity of u_{f_0}=0 m/s. An increase in bulk flow velocity leads to a decrease in the time delay for droplet acceleration. Based on Figures 8.4 and 8.5, it can be concluded that for a droplet diameter of d_f=40 µm, an

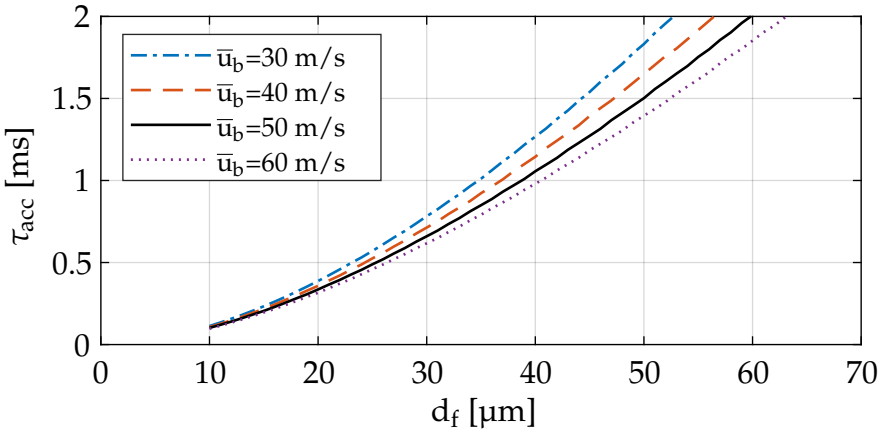

Figure 8.5: Influence of different bulk flow velocities $\bar{u}_b$ on the time delay τ_{acc} for an initial droplet velocity of u_{f_0}=0 m/s.

additional time delay of approximately 1 ms occurs for the acceleration of the droplets (which is not present in the case of gaseous fuel supply).

These three presented time delays are then accumulated to yield the total time delay τ_{calc}:

$$\tau_{calc} = \tau_{mix} + \tau_{cc} + \tau_{acc} \tag{8.2}$$

Table 8.2 shows the calculated time delays for the three individual processes as well as the total time delay of the system τ_{calc}. In addition, the time delay τ_ϕ obtained by least squares fit of the model to the experimental data is presented. For the natural gas case, τ_{acc} is assumed to be zero. The calculated time delays τ_{calc} are observed to agree very well with the time delays determined in the experiment τ_ϕ. Except for one operating point (kerosene case, $\dot{m}_{air}$=25 g/s, ϕ=0.575), the relative deviation of τ_{calc} to τ_ϕ is less than 10% for all operating points. Therefore, it can be concluded that the acceleration of the droplets cause the increased total time delay in the kerosene case compared to the natural gas case, which has already been observed in Figure 7.8. In summary, it can be stated that the phase of the equivalence ratio transfer function can be adequately modeled for both natural gas and kerosene combustion.

Table 8.2: Parameters of the time delay analysis.

Fuel	$\dot{m}_{air}$ [g/s]	ϕ [-]	τ_ϕ [ms]	τ_{calc} [ms]	τ_{mix} [ms]	τ_{cc} [ms]	τ_{acc} [ms]
NGt	25	0.675	3.69	3.58	2.32	1.26	0
	20	0.675	4.29	4.33	2.89	1.44	0
	30	0.675	3.36	3.06	1.93	1.13	0
	25	0.575	4.17	3.93	2.32	1.61	0
	25	0.775	3.31	3.49	2.32	1.17	0
Kerosene	25	0.675	4.78	4.45	1.97	1.34	1.14
	20	0.675	5.86	5.22	2.47	1.52	1.23
	30	0.675	4.10	3.91	1.64	1.21	1.06
	25	0.575	5.82	4.67	1.97	1.73	0.97
	25	0.775	4.40	4.49	1.97	1.20	1.32

8.3 Empirical Modeling of the Time Delay Width

As already conjectured in Section 7.3, the ratio of axial flame extension to convective wavelength has an influence on the gain of the equivalence ratio transfer function. A stronger decay of the gain was observed with increasing ratio of axial flame extension to convective wavelength. The amplitude of the equivalence ratio transfer function is represented by the time delay width σ_ϕ in the time delay model and is analyzed in more detail in the following. Since the convective wavelength is directly proportional to the convective transport velocity (approximated by $\bar{u}_b$), the ratio of axial flame extension to transport velocity is subject of further discussion. Axial flame extension is defined as the maximum axial extension of the flame at which the CH* chemiluminescence intensity is above 18% of its maximum value, which was introduced as a typical threshold by Bade [8].

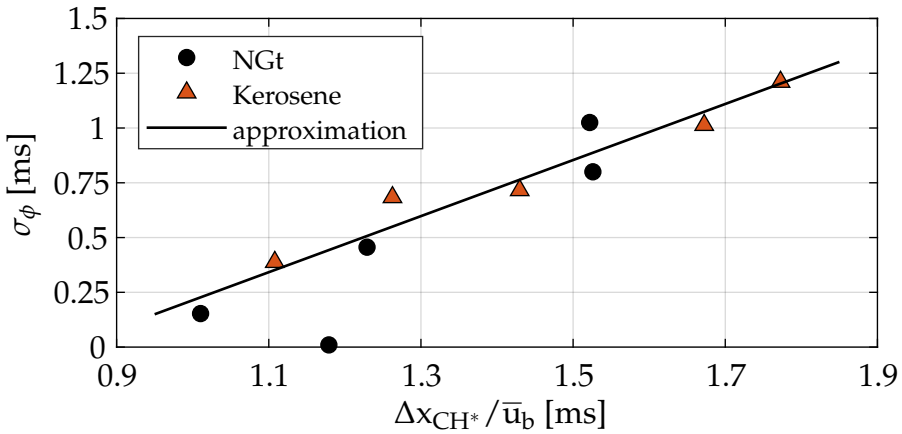

Figure 8.6: Correlation of the ratio of axial flame extension to bulk flow velocity $\Delta x_{CH^*}/\bar{u}_b$ with the time delay width σ_ϕ.

Figure 8.6 shows the correlation of the ratio of axial flame extension to bulk flow velocity $\Delta x_{CH^*}/\bar{u}_b$ with the time delay width σ_ϕ. A linear relationship is clearly evident between the two quantities, regardless of whether liquid or gaseous fuel is injected. The time delay width increases as the ratio of axial flame extension to bulk flow velocity increases. Only one outlier is observed, corresponding to the operating point for natural gas combustion with an air mass flow rate of $\dot{m}_{air}$=25 g/s and an equivalence ratio of ϕ=0.775. This outlier may be due to the limited quality of the result of the fitting procedure for this operating point, as already observed in Figure 8.2. The correlation observed in Figure 8.6 thus confirms the hypothesis of Schuermans et al. [119] that the axial flame extension influences equivalence ratio oscillations.

Since the axial flame extension consequently plays a significant role in modeling equivalence ratio fluctuations, an empirical model is developed to describe axial flame extension for the A^{2}EV burner. Figure 8.7 shows the axial flame extension for natural gas and kerosene combustion for different operating points based on CH* chemiluminescence images. For both natural gas and kerosene combustion, the axial flame extension can be approximated by an exponential function. As the equivalence ratio decreases, the axial flame extension increases. Furthermore, it can be seen that the main air mass flow has almost no influence on the axial

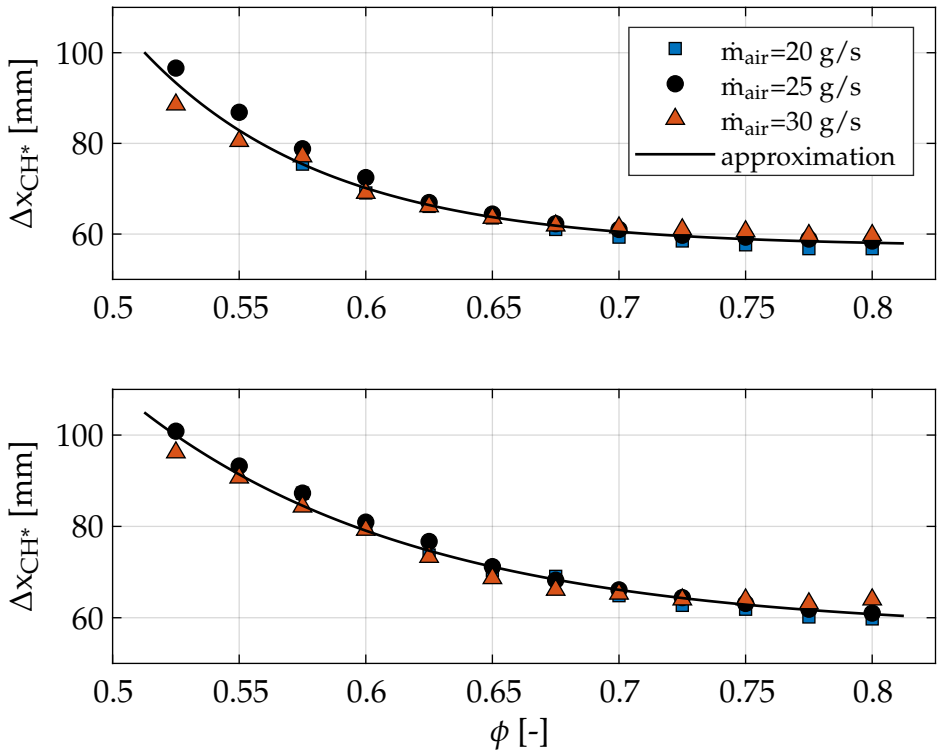

Figure 8.7: Influence of the equivalence ratio on the axial flame extension for natural gas (upper half) and kerosene combustion (lower half).

flame extension. Thus, the empirical approach provides an excellent approximation to accurately predict the axial flame extension for the entire operating range.

Figure 8.8 depicts a comparison of the time delay model containing experimentally determined parameters (obtained by least squares fitting of the model to experimental data) to modeled parameters for the reference operating point. For both, amplitude and phase, the model agrees very well with the least squares fit. The model is clearly capable of explaining the differences observed for the cases with liquid and gaseous fuel supply using the additional droplet acceleration model. Summarizing, the presented one-dimensional model provides excellent prediction of the propagation of equivalence ratio fluctuations for both liquid and gaseous fuel supply.

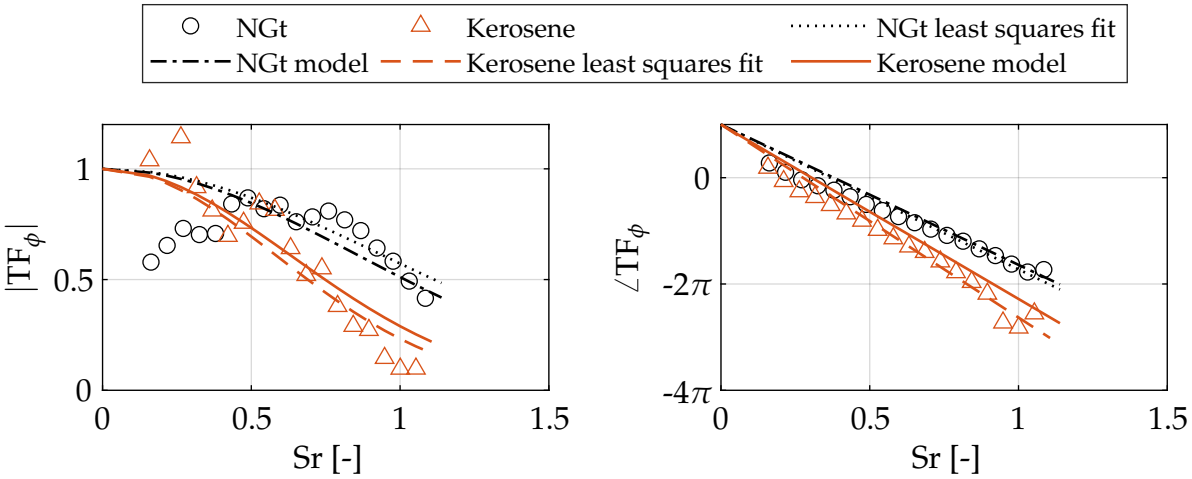

Figure 8.8: Comparison of the time delay model with parameters determined by least squares fitting of the model to experimental data to purely modeled parameters at the reference operating point.

9 Summary and Conclusion

Equivalence ratio fluctuations represent one mechanism for driving thermoacoustic instabilities in lean premixed gas turbine combustors. To ensure the stability of a combustion system, a precise understanding of this mechanism is therefore essential. However, the generation and propagation of equivalence ratio oscillations for liquid fuel operation is scarcely elucidated. This thesis focused on the investigation of equivalence ratio fluctuations for lean premixed spray combustion. The influence of the complex mixture preparation for liquid fuel operation on the propagation of equivalence ratio oscillations compared to natural gas operation was studied in detail.

Experimental investigations were conducted in a single burner test rig under atmospheric conditions using a downscaled version of the A^2EV burner. The burner was extended by a central twin-fluid nozzle for liquid fuel injection. It was verified by NO_x measurements that a premixed spray flame was achieved. Flame parameters such as center of gravity and axial flame extension were evaluated using CH* flame chemiluminescence for both natural gas and kerosene combustion for different equivalence ratios and overall mass flow rates.

First, fundamental investigations into the relationship between the ratio of the different chemiluminescence signals and the equivalence ratio for both lean premixed natural gas and kerosene combustion were conducted using an imaging spectrometer. Previous studies revealed that ratios of different chemiluminescence signals can be utilized for equivalence ratio sensing in the flame. The main findings can be summarized as follows:

- The broadband background radiation significantly influences the sensitivity of all ratios studied to the equivalence ratio. Ratios corrected for background radiation show significantly higher sensitivity to the equivalence ratio compared to the corresponding ratios without background correction.

- The CH*/CO_2* ratio is the only ratio that exhibits a monotonic relationship to the equivalence ratio for both natural gas and kerosene combustion without background correction.

- The CH*/CO_2* ratio (without background correction) exhibits a linear relationship to the reaction zone temperature. The ratio increases as the temperature rises.

Based on the previous findings, a measurement technique was developed to determine equivalence ratio fluctuations in a lean premixed combustor during unstable combustion. An image doubler was mounted in front of an intensified high-speed camera and equipped with a CH* and CO_2* bandpass filter allowing simultaneous acquisition of the two chemiluminescence species on one camera chip. A calibration chart was utilized to determine equivalence ratio fluctuations during acoustic excitation in a phase-resolved manner. Equivalence ratio fluctuations were investigated for gas and spray combustion for different operating conditions in a frequency range from f=60 Hz to f=400 Hz. An equivalence ratio transfer function was established, relating the equivalence ratio fluctuations in the flame to the velocity fluctuations at the burner outlet. The key findings from these studies can be recapitulated as follows:

- The magnitude of this transfer function approaches unity for very low frequencies and decreases as the frequency increases.

- A stronger decrease in gain was observed for liquid fuel combustion compared to gas combustion, attributable to the more complex mixture preparation increasing spatial dispersion.

- The time delay of the equivalence ratio wave from injector to flame is prolonged in case of liquid fuel injection compared to gas injection, due to an additional time delay related to droplet acceleration.

Last, it was validated that the propagation of equivalence ratio fluctuations can be adequately approximated by a time delay model. The time delay from fuel injection to flame and the axial flame extension were identified as the major parameters affecting the equivalence ratio fluctuations in the flame. In addition, physical and empirical approaches were outlined to predict the parameters of the time delay model.

Although the propagation of equivalence ratio oscillations can be accurately predicted using the time delay model, the determination of the time delay associated with droplet acceleration is still based on the droplet characteristics provided by the manufacturer. Future work might therefore focus on the interaction of droplets with the oscillating air mass flow in more detail. Phase-resolved measurements of droplet size and velocity distribution in the mixing tube could provide a deeper understanding of the complex mixture preparation of liquid fuels during acoustic excitation. In particular the influence of acoustic oscillations on the acceleration of the droplets from injection to complete evaporation, taking into account the decreasing diameter of the droplets, could be studied in more detail.

A Appendix

In order to calculate the velocity fluctuations at the burner outlet, the scattering matrix of the burner for the corresponding operating point is required. In this study, velocity fluctuations for three different main air mass flows were investigated. Figure A.1 presents the modeled scattering matrices for the different main air mass flows that were used to calculate the velocity fluctuations at the burner outlet. The scattering matrices were derived from the network model developed by Bade [9]. The temperature of the air mass flow was set to T_{pre}=573 K.

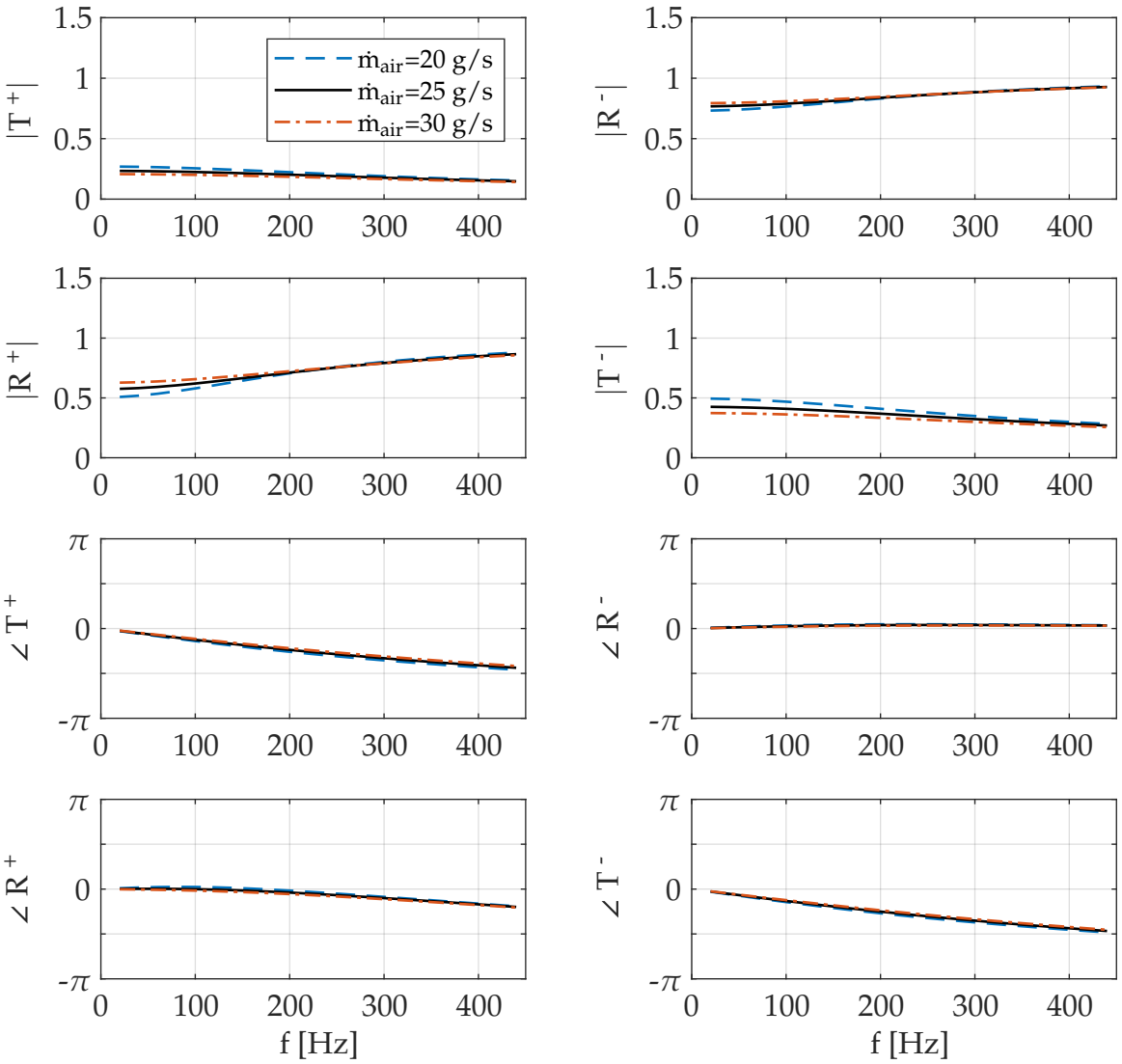

Figure A.1: Comparison of the modeled scattering matrices of the A^{2}EV burner for different main air mass flows. Scattering matrices were derived from the network model developed by Bade [9].

Previous Publications

Parts of this Ph.D. thesis have been published by the author in conference proceedings and journal papers [58, 127, 128]. All of these publications are registered according to the valid doctoral regulations. Therefore, they are not necessarily quoted explicitly in the text. Whether they were referenced, depended on maintaining comprehensibility and providing all necessary context. All of these publications are listed below:

- Vogel, M. Bachfischer, M., Kaufmann, J., Sattelmayer T. Experimental investigation of equivalence ratio fluctuations in a lean premixed kerosene combustor. *Experiments in Fluids* 62, 5 (2021), 93.
- Vogel, M. Bachfischer, M., Kaufmann, J., Sattelmayer T. Optical equivalence ratio measurement of a dual fuel burner for natural gas and kerosene. *Fluids* 7, 2 (2022), 43.
- Kaufmann, J. Vogel, M., Papenbrock, J., Sattelmayer T. Comparison of the flame dynamics of a premixed dual fuel burner for kerosene and natural gas. *International Journal of Spray and Combustion Dynamics* 14, 1-2 (2022), 176-185.
- Vogel, M., Kaufmann, J., Völkl, V., Hirsch, C., Sattelmayer T. Comparison of equivalence ratio fluctuations in a lean premixed combustor for kerosene and natural gas. In *Proceedings of the ASME Turbo Expo* (Boston, Massachusetts, USA, 2023), GT2023-101091.
- Kaufmann, J., Vogel, M., Sattelmayer T. Comparison of the flame dynamics of a liquid fueled swirl stabilized combustor for different de-

grees of fuel-air premixing. In *Proceedings of the ASME Turbo Expo* (Boston, Massachusetts, USA, 2023), GT2023-102448.

- John, T., Magina, N., Han, F., Kaufmann, J., Vogel, M., Sattelmayer T. Modeling flame transfer functions of an industrial premixed burner. In *Proceedings of the ASME Turbo Expo* (Boston, Massachusetts, USA, 2023), GT2023-103246.

Supervised Student Theses

Associated with this Ph.D. thesis, a number of student theses were supervised by the author of the present work. These were prepared at the Chair of Thermodynamics at the Technical University of Munich in the years 2019 to 2022 under the close supervision of the author. Parts of these supervised theses may be incorporated into the present thesis. The author would like to express his sincere gratitude to all formerly supervised students for their commitment and support of this research project.

Name	Title / Thesis
Michael Bachfischer	Spectral analysis of the combustion of kerosene in a combustion test rig for gas turbines, Bachelor's thesis, May 2020
Jannes Papenbrock	Highspeed camera images of combustion instabilities in a turbulent, swirl stabilized flame, Bachelor's thesis, May 2020
Tianxiao Gao	High-speed images of a turbulent, swirl-stabilized flame for the investigation of combustion instabilities, Semester thesis, July 2020
Justus Benteler	Experimental studies of combustion instabilities in turbulent, swirl-stabilized flame, Bachelor's thesis, January 2021
John Paul Panuthara	Numerical flow field simulations of a single burner gas turbine combustor, Semester thesis, March 2022
Caio Crisostomo Pereira	Optical investigations of flame characteristics of a dual fuel burner with variable degree of premixing, Master's thesis, August 2022
Vinzenz Völkl	Numerical investigation of equivalence ratio fluctuations in a lean premixed gas turbine combustor, Master's thesis, December 2022
Alexander Großhauser	Numerical Investigation of the Mixture Preperation in a Lean Premixed Gas Turbine Combustor, Semester thesis, December 2022

Bibliography

[1] ÅBOM, M. Measurement of the scattering-matrix of acoustical two-ports. *Mechanical Systems and Signal Processing 5*, 2 (1991), 89–104.

[2] ÅBOM, M. A note on the experimental determination of acoustical two-port matrices. *Journal of Sound and Vibration 155*, 1 (1992), 185–188.

[3] ÅBOM, M., AND BODÉN, H. Error analysis of two-microphone measurements in ducts with flow. *Journal of the Acoustical Society of America 83*, 6 (1988), 2429–2438.

[4] AKIMOTO, H. *Atmospheric reaction chemistry*. Springer, Tokyo, 2016.

[5] ALEMELA, P. R. *Measurement and scaling of acoustic transfer matrices of premixed swirl flames*. PhD Thesis, Technical University of Munich, Munich, 2009.

[6] ALEMELA, P. R., FANACA, D., HIRSCH, C., SATTELMAYER, T., AND SCHUERMANS, B. Determination and scaling of thermo acoustic characteristics of premixed flames. *International Journal of Spray and Combustion Dynamics 2*, 2 (2010), 169–198.

[7] ASHGRIZ, N. *Handbook of atomization and sprays: theory and applications*. Springer, New York, 2011.

[8] BADE, S. *Messung und Modellierung der thermoakustischen Eigenschaften eines modularen Brennersystems für vorgemischte Drallflammen*. PhD Thesis, Technical University of Munich, Munich, 2014.

[9] BADE, S., WAGNER, M., HIRSCH, C., SATTELMAYER, T., AND SCHUERMANS, B. Design for thermo-acoustic stability: modeling of burner and flame dynamics. *Journal of Engineering for Gas Turbines and Power 135*, 11 (2013), 111502.

[10] BALLESTER, J., AND GARCÍA-ARMINGOL, T. Diagnostic techniques for the monitoring and control of practical flames. *Progress in Energy and Combustion Science 36*, 4 (2010), 375–411.

[11] BÄSSLER, S. *Einfluss des Vorverdampfungsgrades auf die Stickoxidbildung in Sprayflammen*. PhD Thesis, Technical University of Munich, Munich, 2008.

[12] BAUERHEIM, M., NICOUD, F., AND POINSOT, T. Progress in analytical methods to predict and control azimuthal combustion instability modes in annular chambers. *Physics of Fluids 28*, 2 (2016), 021303.

[13] BLÜMNER, R., PASCHEREIT, C. O., AND OBERLEITHNER, K. Generation and transport of equivalence ratio fluctuations in an acoustically forced swirl burner. *Combustion and Flame 209* (2019), 99–116.

[14] BOBUSCH, C. B., CÓSIĆ, B., MOECK, J. P., AND PASCHEREIT, C. O. Optical measurement of local and global transfer functions for equivalence ratio fluctuations in a turbulent swirl flame. *Journal of Engineering for Gas Turbines and Power 136*, 2 (2014), 021506.

[15] CANDEL, S. Combustion dynamics and control: progress and challenges. *Proceedings of the Combustion Institute 29*, 1 (2002), 1–28.

[16] CANDEL, S., DUROX, D., SCHULLER, T., BOURGOUIN, J. F., AND MOECK, J. P. Dynamics of swirling flames. *Annual Review of Fluid Mechanics 46* (2014), 147–173.

[17] CHO, J. H., AND LIEUWEN, T. C. Modeling the response of premixed flames to mixture ratio perturbations. In *Proceedings of the ASME Turbo Expo* (Atlanta, Georgia, USA, 2003), GT2003-38089.

[18] CHRISTOU, T., STELZNER, B., AND ZARZALIS, N. Influence of an oscillating airflow on the prefilming airblast atomization process. *Atomization and Sprays 31*, 3 (2021), 1–14.

[19] CLARK, T. P. Studies of OH, CO, CH and C2 radiation from laminar and turbulent propane-air and ethylene-air flames - NACA Technical Note 4266. Tech. rep., National Advisory Committee for Aeronautics, Lewis Flight Propulsion Laboratory, Cleveland, Ohio, 1958.

[20] CLAVIN, P., AND SIGGIA, E. D. Turbulent premixed flames and sound generation. *Combustion Science and Technology 78*, 1-3 (1991), 147–155.

[21] CORREA, S. M. A review of NOx formation under gas-turbine combustion conditions. *Combustion Science and Technology 87*, 1-6 (1993), 329–362.

[22] CÓSIĆ, B., REISS, F., BLÜMER, M., FREKERS, C., GENIN, F., PÄHR, J., AND WASSMER, D. Development and integration of the dual fuel combustion system for the MGT gas turbine family. In *Proceedings of the ASME Turbo Expo* (Virtual, Online, jun 2021), GT2021-59162.

[23] CULICK, F. E. C. Combustion instabilities in liquid-fueled propulsion systems - an overview. In *AGARD Conference Proceedings No.450* (1988).

[24] CUMPSTY, N. A., AND MARBLE, F. E. Core noise from gas turbine exhausts. *Journal of Sound and Vibration 54*, 2 (1977), 297–309.

[25] DANDY, D. S., AND VOSEN, S. R. Numerical and experimental studies of hydroxyl radical chemiluminescence in methane-air flames. *Combustion Science and Technology 82*, 1-6 (1992), 131–150.

[26] DOCQUIER, N., AND CANDEL, S. Combustion control and sensors: a review. *Progress in Energy and Combustion Science 28*, 2 (2002), 107–150.

[27] DOCQUIER, N., LACAS, F., AND CANDEL, S. Closed-loop equivalence ratio control of premixed combustors using spectrally resolved chemiluminescence measurements. *Proceedings of the Combustion Institute 29*, 1 (2002), 139–145.

[28] DOWLING, A., AND FFOWCS WILLIAMS, J. E. *Sound and sources of sound*. Ellis Horwood Ltd., Chichester, 1983.

[29] DRIBINSKI, V., OSSADTCHI, A., MANDELSHTAM, V. A., AND REISLER, H. Reconstruction of abel-transformable images: the gaussian basis-set expansion abel transform method. *Review of Scientific Instruments 73*, 7 (2002), 2634–2642.

[30] DUCRUIX, S., SCHULLER, T., DUROX, D., AND CANDEL, S. Combustion dynamics and instabilities: elementary coupling and driving mechanisms. *Journal of Propulsion and Power 19*, 5 (2003), 722–734.

[31] ECKBRETH, A. C. *Laser diagnostics for combustion temperature and species*, 2nd ed. Gordon and Breach, New York, 1996.

[32] ECKSTEIN, J. *On the mechanisms of combustion driven low-frequency oscillations in aero-engines*. PhD Thesis, Technical University of Munich, Munich, 2004.

[33] ECKSTEIN, J., FREITAG, E., HIRSCH, C., AND SATTELMAYER, T. Experimental study on the role of entropy waves in low-frequency oscillations in a RQL combustor. *Journal of Engineering for Gas Turbines and Power 128*, 2 (2006), 264–270.

[34] ECKSTEIN, J., FREITAG, E., HIRSCH, C., SATTELMAYER, T., VON DER BANK, R., AND SCHILLING, T. Forced low-frequency spray characteristics of a generic airblast swirl diffusion burner. *Journal of Engineering for Gas Turbines and Power 127*, 2 (2005), 301–306.

[35] FENT, K. *Ökotoxikologie*, 4th ed. Thieme, Stuttgart, 2013.

[36] FISCHER, A. *Hybride, thermoakustische Charakterisierung von Drallbrennern*. PhD Thesis, Technical University of Munich, Munich, 2004.

[37] FISCHER, A., HIRSCH, C., AND SATTELMAYER, T. Comparison of multi-microphone transfer matrix measurements with acoustic network models of swirl burners. *Journal of Sound and Vibration 298*, 1-2 (2006), 73–83.

[38] FREITAG, E. *On the measurement and modelling of flame transfer functions at elevated pressure*. PhD Thesis, Technical University of Munich, Munich, 2009.

[39] GARCÍA-ARMINGOL, T., BALLESTER, J., AND SMOLARZ, A. Chemiluminescence-based sensing of flame stoichiometry: influence of the measurement method. *Measurement: Journal of the International Measurement Confederation 46*, 9 (2013), 3084–3097.

[40] GAYDON, A. G. *The spectroscopy of flames*, 2nd ed. Chapman and Hall, London, 1974.

[41] GAYDON, A. G., AND WOLFHARD, H. G. *Flames: their structure, radiation and temperature*, 4th ed. Chapman and Hall, London, 1979.

[42] GÜLEN, S. C., AND CURTIS, M. Gas turbine's role in energy transition. In *Proceedings of the ASME Turbo Expo* (Rotterdam, Netherlands, 2022), GT2022-81802.

[43] GÜTHE, F., AND SCHUERMANS, B. Phase-locking in post-processing for pulsating flames. *Measurement Science and Technology 18*, 9 (2007), 3036–3042.

[44] GUYOT, D., GUETHE, F., SCHUERMANS, B., LACARELLE, A., AND PASCHEREIT, C. O. CH*/OH* chemiluminescence response of an atmospheric premixed flame under varying operating conditions. In *Proceedings of ASME Turbo Expo* (Glasgow, UK, 2010), GT2010-23135.

[45] HALL, J. M., DE VRIES, J., AMADIO, A. R., AND PETERSEN, E. L. Towards a kinetics model of CH chemiluminescence. In *43rd AIAA Aerospace Sciences Meeting and Exhibit* (Reno, Nevada, USA, 2005), pp. 15175–15185.

[46] HARDALUPAS, Y., AND ORAIN, M. Local measurements of the time-dependent heat release rate and equivalence ratio using chemiluminescent emission from a flame. *Combustion and Flame 139*, 3 (2004), 188–207.

[47] HICKSTEIN, D. D., GIBSON, S. T., YURCHAK, R., DAS, D. D., AND RYAZANOV, M. A direct comparison of high-speed methods for the numerical abel transform. *Review of Scientific Instruments 90*, 6 (2019), 065115.

[48] HINZE, J. O. *Turbulence*, 2nd ed. McGraw-Hill, New York, 1975.

[49] HIRSCH, C., FANACA, D., REDDY, P., POLIFKE, W., AND SATTELMAYER, T. Influence of the swirler design on the flame transfer function of premixed flames. In *Proceedings of ASME Turbo Expo* (Reno, Nevada, USA, 2005), GT2005-68195.

[50] HUANG, Y., AND YANG, V. Dynamics and stability of lean-premixed swirl-stabilized combustion. *Progress in Energy and Combustion Science 35*, 4 (2009), 293–364.

[51] HUBBARD, S., AND DOWLING, A. P. Acoustic instabilities in premix burners. In *4th AIAA/CEAS Aeroacoustics Conference* (Toulouse, France, 1998), AIAA 98-2272.

[52] JOHN, R. R., AND SUMMERFIELD, M. Effect of turbulence on radiation intensity from propane-air flames. *Journal of Jet Propulsion 27*, 2 (1957), 169–175.

[53] JOHNSTON, H. S. Atmospheric ozone. *Annu. Rev. Phys. Chem. 1992 43* (1992), 1–32.

[54] JÓZSA, V., AND KUN-BALOG, A. Spectroscopic analysis of crude rapeseed oil flame. *Fuel Processing Technology 139* (2015), 61–66.

[55] KATHER, V., LÜCKOFF, F., PASCHEREIT, C. O., AND OBERLEITHNER, K. Interaction of equivalence ratio fluctuations and flow fluctuations in acoustically forced swirl flames. *International Journal of Spray and Combustion Dynamics 13*, 1-2 (2021), 72–95.

[56] KATHROTIA, T., FIKRI, M., BOZKURT, M., HARTMANN, M., RIEDEL, U., AND SCHULZ, C. Study of the H+O+M reaction forming OH*: kinetics of OH* chemiluminescence in hydrogen combustion systems. *Combustion and Flame 157*, 7 (2010), 1261–1273.

[57] KATHROTIA, T., RIEDEL, U., AND WARNATZ, J. A numerical study on the relation of OH*, CH*, and C2* chemiluminescence and heat release in premixed methane flames. In *4th European Combustion Meeting* (Vienna, Austria, 2009).

[58] KAUFMANN, J., VOGEL, M., PAPENBROCK, J., AND SATTELMAYER, T. Comparison of the flame dynamics of a premixed dual fuel burner for kerosene and natural gas. *International Journal of Spray and Combustion Dynamics 14*, 1-2 (2022), 176–185.

[59] KELLER, J. J. Thermoacoustic oscillations in combustion chambers of gas turbines. *AIAA Journal 33*, 12 (1995), 2280–2287.

[60] KELLER, J. J., EGLI, W., AND HELLAT, J. Thermally induced low-frequency oscillations. *Journal of Applied Mathematics and Physics 36* (1985), 250–274.

[61] KIM, K. T., LEE, J. G., QUAY, B. D., AND SANTAVICCA, D. A. Spatially distributed flame transfer functions for predicting combustion dynamics in lean premixed gas turbine combustors. *Combustion and Flame 157*, 9 (2010), 1718–1730.

[62] KLARMANN, N., SATTELMAYER, T., GENG, W., ZOLLER, B. T., AND MAGNI, F. Impact of flame stretch and heat loss on heat release distributions in gas turbine combustors: model comparison and validation. In *Proceedings of the ASME Turbo Expo* (Seoul, South Korea, 2016), GT2016-57625.

[63] KLARMANN, N. E. *Modeling turbulent combustion and CO emissions in partially-premixed conditions considering flame stretch and heat loss*. PhD Thesis, Technical University of Munich, Munich, 2019.

[64] KLIMCZAK, D. Influence of ukrainian crisis on the european gas market. *Energy & Environment 26*, 3 (2015), 425–435.

[65] KOJIMA, J., IKEDA, Y., AND NAKAJIMA, T. Spatially resolved measurement of OH*, CH*, and C2* chemiluminescence in the reaction zone of laminar methane/air premixed flames. *Proceedings of the Combustion Institute 28* (2000), 1757–1764.

[66] KOJIMA, J., IKEDA, Y., AND NAKAJIMA, T. Basic aspects of OH(A), CH(A), and C2(d) chemiluminescence in the reaction zone of laminar methane-air premixed flames. *Combustion and Flame 140*, 1-2 (2005), 34–45.

[67] KOMAREK, T., AND POLIFKE, W. Impact of swirl fluctuations on the flame response of a perfectly premixed swirl burner. *Journal of Engineering for Gas Turbines and Power 132*, 6 (2010), 061503.

[68] KRÄMER, M. *Untersuchungen zum Bewegungsverhalten von Tropfen in turbulenter Strömung im Hinblick auf Verbrennungsvorgänge*. PhD Thesis, TH Karlsruhe, Karlsruhe, 1988.

[69] LAKOWICZ, J. *Principles of fluorescence spectroscopy*, 3rd ed. Springer, New York, 2006.

[70] LECHNER, C., AND SEUME, J. *Stationäre Gasturbinen*, 3rd ed. Springer Vieweg, Berlin, 2019.

[71] LEE, H., AND SEO, S. Experimental study on spectral characteristics of kerosene swirl combustion. *Procedia Engineering 99* (2015), 304–312.

[72] LEE, J. C. Y., MALTE, P. C., AND BENJAMIN, M. A. Low NOx combustion for liquid fuels: atmospheric pressure experiments using a staged prevaporizer-premixer. *Journal of Engineering for Gas Turbines and Power 125*, 4 (2003), 861–871.

[73] LEE, J. G., KIM, K., AND SANTAVICCA, D. A. Measurement of equivalence ratio fluctuation and its effect on heat release during unstable combustion. *Proceedings of the Combustion Institute 28*, 1 (2000), 415–421.

[74] LEE, J. G., KIM, K., AND SANTAVICCA, D. A. A study of the role of equivalence ratio fluctuations during unstable combustion in a lean premixed combustor. In *38th AIAA/ASME/SAE/ASEE Joint Propulsion Conference and Exhibit* (Indianapolis, Indiana, USA, 2002), AIAA 2002-4015.

[75] LELLECK, S., AND SATTELMAYER, T. NOx-formation and CO-burnout in water-injected, premixed natural gas flames at typical gas turbine combustor residence times. *Journal of Engineering for Gas Turbines and Power 140*, 5 (2018), 051504.

[76] LI, H., WEHE, S. D., AND MCMANUS, K. R. Real-time equivalence ratio measurements in gas turbine combustors with a near-infrared diode laser sensor. *Proceedings of the Combustion Institute 33*, 1 (2011), 717–724.

[77] LIAO, S. Y., JIANG, D. M., AND CHENG, Q. Determination of laminar burning velocities for natural gas. *Fuel 83*, 9 (2004), 1247–1250.

[78] LIEUWEN, T., TORRES, H., JOHNSON, C., AND ZINN, B. A mechanism of combustion instability in lean premixed gas turbine combustors. *Journal of Engineering for Gas Turbines and Power 123*, 1 (2001), 182–189.

[79] LIEUWEN, T., AND ZINN, B. T. The role of equivalence ratio oscillations in driving combustion instabilities in low NOx gas turbines. *27th International Symposium on Combustion 27*, 2 (1998), 1809–1816.

[80] LIEUWEN, T. C. *Unsteady combustor physics*. Cambridge University Press, Cambridge, UK, 2012.

[81] LIEUWEN, T. C., AND YANG, V. *Combustion instabilities in gas turbine engines*. American Institute of Aeronautics and Astronautics (AIAA), Reston, VA, USA, 2005.

[82] LINDMAN, O., ANDERSSON, M., PERSSON, M., AND MUNKTELL, E. Development of a liquid fuel combustion system for SGT-750. In *Proceedings of ASME Turbo Expo* (Düsseldorf, Germany, 2014), GT2014-25380.

[83] LUO, J., YING, K., AND BAI, J. Savitzky-Golay smoothing and differentiation filter for even number data. *Signal Processing 85*, 7 (2005), 1429–1434.

[84] MARBLE, F. E., AND CANDEL, S. M. Acoustic disturbance from gas non-uniformities convected through a nozzle. *Journal of Sound and Vibration 55*, 2 (1977), 225–243.

[85] MAYER, C. *Konzept zur vorgemischten Verbrennung wasserstoffhaltiger Brennstoffe in Gasturbinen*. PhD Thesis, Technical University of Munich, Munich, 2012.

[86] MERKER, G. P., AND TEICHMANN, R. *Grundlagen Verbrennungsmotoren*, 8th ed. Springer Vieweg, Wiesbaden, 2018.

[87] MORSE, P. M., AND INGARD, K. U. *Theoretical acoustics*. Princeton University Press, Princeton, New Jersey, 1986.

[88] MUNJAL, M. L. *Acoustics of ducts and mufflers*. John Wiley and Sons, New York, 1987.

[89] MUNJAL, M. L., AND DOICES, A. G. Theory of a two source-location method for direct experimental evaluation of the four-pole parameters of an aeroacoustic element. *Journal of Sound and Vibration 141*, 2 (1990), 323–333.

[90] MURUGANANDAM, T. M., KIM, B. H., MORRELL, M. R., NORI, V., PATEL, M., ROMIG, B. W., AND SEITZMAN, J. M. Optical equivalence ratio sensors for gas turbine combustors. *Proceedings of the Combustion Institute 30*, 1 (2005), 1601–1609.

[91] NAJM, H. N., PAUL, P. H., MUELLER, C. J., AND WYCKOFF, P. S. On the adequacy of certain experimental observables as measurements of flame burning rate. *Combustion and Flame 113*, 3 (1998), 312–332.

[92] NOIRAY, N., AND SCHUERMANS, B. Deterministic quantities characterizing noise driven Hopf bifurcations in gas turbine combustors. *International Journal of Non-Linear Mechanics 50* (2013), 152–163.

[93] NORI, V. N. *Modeling and analysis of chemiluminescence sensing for syngas, methane and jet-a combustion*. PhD Thesis, Georgia Institute of Technology, Georgia, 2008.

[94] NORI, V. N., AND SEITZMANN, J. M. CH* chemiluminescence modeling for combustion diagnostics. *Proceedings of the Combustion Institute 32 I*, 1 (2009), 895–903.

[95] O'CONNOR, J., ACHARYA, V., AND LIEUWEN, T. Transverse combustion instabilities: acoustic, fluid mechanic, and flame processes. *Progress in Energy and Combustion Science 49* (2015), 1–39.

[96] ORAIN, M., AND HARDALUPAS, Y. Effect of fuel type on equivalence ratio measurements using chemiluminescence in premixed flames. *Comptes Rendus - Mecanique 338*, 5 (2010), 241–254.

[97] ORAIN, M., AND HARDALUPAS, Y. Measurements of local mixture fraction of reacting mixture in swirl-stabilised natural gas-fuelled burners. *Applied Physics B: Lasers and Optics 105*, 2 (2011), 435–449.

[98] PANOUTSOS, C. S., HARDALUPAS, Y., AND TAYLOR, A. M. Numerical evaluation of equivalence ratio measurement using OH* and CH* chemiluminescence in premixed and non-premixed methane-air flames. *Combustion and Flame 156*, 2 (2009), 273–291.

[99] PASCHEREIT, C. O., FLOHR, P., AND SCHUERMANS, B. Prediction of combustion oscillations in gas turbine combustors. In *39th AIAA Aerospace Sciences Meeting and Exhibit* (Reno, Nevada, USA, 2001), AIAA 2001-0484.

[100] PASCHEREIT, C. O., GUTMARK, E., AND WEISENSTEIN, W. Structure and Control of Thermoacoustic Instabilities in a Gas-turbine Combustor. *Combustion Science and Technology 138*, 1-6 (1998), 213–232.

[101] PASCHEREIT, C. O., SCHUERMANS, B., POLIFKE, W., AND MATTSON, O. Measurement of transfer matrices and source terms of premixed flames. *Journal of Engineering for Gas Turbines and Power 124*, 2 (2002), 239–247.

[102] PETERLEITHNER, J., STADLMAIR, N. V., WOISETSCHLÄGER, J., AND SATTELMAYER, T. Analysis of measured flame transfer functions with locally resolved density fluctuation and OH-Chemiluminescence Data. *Journal of Engineering for Gas Turbines and Power 138*, 3 (2016).

[103] POINSOT, T., AND VEYNANTE, D. *Theoretical and numerical combustion*, 2nd ed. Edwards, Philadelphia, 2005.

[104] POINSOT, T. J., TROUVE, A. C., VEYNANTE, D. P., CANDEL, S. M., AND ESPOSITO, E. J. Vortex-driven acoustically coupled combustion instabilities. *Journal of Fluid Mechanics 177* (1987), 265–292.

[105] POLIFKE, W., PASCHEREIT, C. O., AND DÖBBELING, K. Constructive and destructive interference of acoustic and entropy waves in a premixed combustor with a choked exit. *International Journal of Acoustics and Vibration 6*, 3 (2001), 135–146.

[106] PUTNAM, A. A., AND DENNIS, W. R. Burner oscillations of the gauze-tone type. *Journal of the Acoustical Society of America 26*, 5 (1954), 716–725.

[107] RAYLEIGH, J. W. S. The explanation of certain acoustic phenomena. *Nature 18* (1878), 319–321.

[108] READER, J., SANSONETTI, C. J., AND BRIDGES, J. M. Irradiances of spectral lines in mercury pencil lamps. *Applied Optics 35* (1996), 78–83.

[109] REYES, J., KUMAR ABHINAVAM KAILASANATHAN, R., AND AHMED, K. Relationship between the chemiluminescence intensity ratio of C2* and CH*, charge pressure, and equivalence ratio for gasoline. *Energy and Fuels 32*, 10 (2018), 10933–10940.

[110] RICHARDS, G. A., AND JANUS, M. C. Characterization of oscillations during premix gas turbine combustion. *Journal of Engineering for Gas Turbines and Power 120* (1998), 294–302.

[111] RUSS, M., MEYER, A., AND BÜCHNER, H. Scaling thermo-acoustic characteristics of lp and lpp swirl flames. In *Proceedings of ASME Turbo Expo* (Montreal, Canada, 2007), GT2007-27775.

[112] SAMANIEGO, J. M., EGOLFOPOULOS, F. N., AND BOWMAN, C. T. CO2* chemiluminescence in premixed flames. *Combustion Science and Technology 109*, 1-6 (1995), 183–203.

[113] SANGL, J. *Erhöhung der Brennstoffflexibilität von Vormischbrennern durch Beeinflussung der Wirbeldynamik*. PhD Thesis, Technical University of Munich, Munich, 2011.

[114] SARAVANAMUTTOO, H. I. H., ROGERS, G., AND COHEN, H. *Gas turbine theory*, 7th ed. Pearson, Harlow, England, 2017.

[115] SATTELMAYER, T. Influence of the combustor aerodynamics on combustion instabilities from equivalence ratio fluctuations. *Journal of Engineering for Gas Turbines and Power 125*, 1 (2003), 11–19.

[116] SCARINCI, T., AND FREEMAN, C. The propagation of a fuel-air ratio disturbance in a simple premixer and its influence on pressure wave amplification. In *Proceedings of the ASME Turbo Expo* (Munich, Germany, 2000), 2000-GT-0106.

[117] SCHADOW, K. C., AND GUTMARK, E. Combustion instability related to vortex shedding in dump combustors and their passive control. *Progress in Energy and Combustion Science 18*, 2 (1992), 117–132.

[118] SCHMID, H.-P., HABISREUTHER, P., AND LEUCKEL, W. A model for calculating heat release in premixed turbulent flames. *Combustion and Flame 133*, 1-2 (1998), 79–91.

[119] SCHUERMANS, B., BELLUCCI, V., GUETHE, F., MEILI, F., FLOHR, P., AND PASCHEREIT, C. O. A detailed analysis of thermoacoustic interaction mechanisms in a turbulent premixed flame. In *Proceedings of ASME Turbo Expo* (Vienna, Austria, 2004), GT2004-53831.

[120] SCHUERMANS, B. B. H., PASCHEREIT, C. O., VAN DER LINDEN, J. H., AND POLIFKE, W. Prediction of acoustic pressure spectra in combustion systems using swirl stabilized gas turbine burners. In *Proceedings of the ASME Turbo Expo* (Munich, Germany, 2000), 2000-GT-0105.

[121] SCHUERMANS, B. B. H., POLIFKE, W., AND PASCHEREIT, C. O. Modeling transfer matrices of premixed flames and comparison with experimental results. In *Proceedings of the ASME International Gas Turbine and Aeroengine Congress and Exhibition* (Indianapolis, Indiana, USA, 1999), 99-GT-132.

[122] SPURK, J., AND AKSEL, N. *Strömungslehre*, 9th ed. Springer Vieweg, Berlin, 2019.

[123] STADLMAIR, N. V. *Influence of water injection on the thermoacoustic stability of a lean-premixed combustor*. PhD Thesis, Technical University of Munich, Munich, 2018.

[124] STRAHLE, W. C. On combustion generated noise. *Journal of Fluid Mechanics 49*, 2 (1971), 399–414.

[125] TIPLER, P. A., AND MOSCA, G. *Physik für Wissenschaftler und Ingenieure*, 7th ed. Springer Spektrum, Berlin, 2015.

[126] TURNS, S. R. *An introduction to combustion*, 2nd ed. McGraw-Hill, Boston, 2000.

[127] VOGEL, M., BACHFISCHER, M., KAUFMANN, J., AND SATTELMAYER, T. Experimental investigation of equivalence ratio fluctuations in a lean premixed kerosene combustor. *Experiments in Fluids 62*, 5 (2021), 93.

[128] VOGEL, M., BACHFISCHER, M., KAUFMANN, J., AND SATTELMAYER, T. Optical equivalence ratio measurement of a dual fuel burner for natural gas and kerosene. *Fluids 7*, 2 (2022), 43.

[129] WARNATZ, J., MAAS, U., AND DIBBLE, R. W. *Verbrennung*, 3rd ed. Springer, Berlin, 2001.

[130] WU, Y., MODICA, V., YU, X., AND GRISCH, F. Experimental investigation of laminar flame speed measurement for kerosene fuels: jet A-1, surrogate fuel, and its pure components. *Energy and Fuels 32*, 2 (2018), 2332–2343.

[131] YI, T., AND SANTAVICCA, D. A. Flame spectra of a turbulent liquid-fueled swirl-stabilized lean-direct injection combustor. *Journal of Propulsion and Power 25*, 5 (2009), 1058–1067.

[132] ZUCCA, A., KHAYRULIN, S., VYAZEMSKAYA, N., SHERSHNYOV, B., AND MYERS, G. Development of a liquid fuel system for GE MS5002E gas turbine: rig test validation of the combustor performance. In *Proceedings of ASME Turbo Expo* (Düsseldorf, Germany, 2014), GT2014-26046.